# COVER PAGE

| | |
|---|---|
| **Project Title:** HYDROCARBON, OXIDATION, DEHYDROGENATION AND COUPLING OVER MODEL METAL OXIDE SURFACES | |
| **Federal Award Identification Number:** DE-FG02-97ER14751 | |
| **Agency Code:** 8900 | **Organization:** Office of Basic Energy Sciences |
| **Recipient Award Identification Number:** 429128 | **Project Period:** 02/01/1997 - 08/31/2021 |
| **Reporting Period:** 02/01/1997 - 08/31/2021 | **Budget Period:** 02/01/1997 - 08/31/2021 |
| **Report Term:** End of Project | **Submission Date and Time:** N/A |
| **Principal Investigator Information:**<br>Dr. David F Cox Professor Emeritus<br>MailStop Code: 0211<br>635 Prices Fork Road Blacksburg, VA 24061<br><br>**Email:** dfcox@vt.edu<br>**Contact:** (540) 231-6829 | **Recipient Organization:**<br>Virginia Polytechnic Institute and State University MailStop Code: MC 0170<br>1880 Pratt Drive, 2006 2006 Blacksburg, VA 24060-3580 Country: USA<br>**DUNS:** 003137015<br>**EIN:** 546001805 |
| **Submitting Official Information:**<br>N/A<br>**Email:** N/A<br>**Contact:** N/A | |

# ACCOMPLISHMENTS

**1. What are the major goals of the project?**

The research priorities and goals evolved and shifted to new topic areas over the different funding/renewal periods of the 24.5 years of the project. All of the experimental work was aimed at understanding adsorption and reaction properties of atomic scale features on well-defined (single crystal) metal oxide surfaces. Our focus was to concentrate on materials with known catalytic applications that were available to us, but not commonly available in single crystal form from commercial laboratories. Additionally, density functional theory (DFT) was used complement our experimental surface science studies and to explore issues of geometric and electronic structure of oxide surface and bulk materials. The accomplishments and findings from these studies are summarized in section 2 in chronological order by funding cycles over the project period. Materials studied experimentally and computationally include the base metal oxide $SnO_2$ and transition metal oxides $\alpha$-$Cr_2O_3$, $\alpha$-$Fe_2O_3$ and MnO. DFT was used also to examine a wider array of bulk materials, primarily silicates, with geoscientists at Virginia Tech. Research goals included:

- Understanding acid/base properties of atomic features on well-defined oxide surfaces
- Determining how common probe molecules interact with well-defined oxide surfaces
- Elucidating site requirements (structure/function relationships) for selective and non-selective oxidation and dehydrogenation of hydrocarbon species on oxide surfaces
- Understand site requirements for reactions of specific hydrocarbon oxygenates (alcohols,aldehydes and organic acids) as models for oxygenated surface intermediates in oxidation reactions
- Examining local structure of oxide surface defects with scanning tunneling microscopy STM (limited)
- Gaining insight on geometric and electronic structure of bulk oxide materials and surface interactions with adsorbate and reactive species with DFT
- Providing experimental benchmarks for adsorption and reaction on transition metal oxides for benchmarking DFT calculations
- Elucidating a (nearly) pure electronic effect (d-electron count) in transition metal oxide reactivity using equivalent surface terminations of isostructural transition metal oxides
- Synthesize and test a planar, multicomponent, transition metal oxide-based model catalyst for thermochemical water splitting

**2. What was accomplished under these goals?**

# 2.1 Results and Accomplishments 2/1/97 – 01/31/2000

## 2.1.1 Experimental Investigations of Acidity and Basicity of Well-Defined Oxide Surfaces

Our interest in acid/base properties of oxide single crystal surfaces began with an earlier study of methanol oxidation on stoichiometric and oxygen-deficient $SnO_2$(110) surfaces [1, 2] from a previous DOE BES grant. These studies of the interaction of alcohols (weak Brønsted acids) with different preparations of the $SnO_2$(110) surface have shown that the probability for alcohol dissociation to surface alkoxides is strongly dependent on the nature of the exposed surface cation[1, 2]. This dissociation process is normally considered a simple acid/base reaction, with the alkoxide ion bonding to a surface cation (Lewis acid site), and the proton binding at surface lattice oxygen anion (basic site) to form a surface hydroxyl [3]. In a previous project period, the acidic properties of well-defined $SnO_2$(110) surfaces were characterized using NH3 as a probe of Lewis acidity. A correlation was found between the "acidity" of the surface cations (as measured by the $\Delta H_{ads}$ of $NH_3$) and their ability to dissociate weak Brønsted acids like methanol. Four-coordinate $Sn^{2+}$ cations on the reduced surface exhibit the highest $\Delta H_{ads}$ for ammonia [4, 5].

Efforts to probe the "basicity" of the surface and the properties of different surface oxygen anions with $CO_2$ were less successful [4]. For stoichiometric and oxygen-deficient forms of the $SnO_2$ (110) and the $Cu_2O$ (111) surfaces [6], $CO_2$ exposures at $LN_2$ temperatures in UHV show evidence only for weakly adsorbed molecular $CO_2$. High temperature exposures were also investigated in a high-pressure cell attached to the vacuum system for conditions up to 200°C and 1 atmosphere. *No evidence of any vacuum-stable carbonates or $CO_2$ adsorbate was observed* by XPS or thermal desorption experiments for a room-temperature surface following these treatment conditions [4].

In the first budget period of this project, this work was continued along two different routes. $CO_2$ adsorption over $Cr_2O_3$ (10$\underline{1}$2) was investigated because observations of the uptake of small amounts of background $CO_2$ on this surface were made during the course of other experiments. The coordinately-unsaturated, electropositive carbon atom in $CO_2$ imparts an acidic character to the molecule according to the Usanovich theory of acidity and basicity [7]. If carbonate formation is viewed simplistically as the addition of a basic oxide ion to carbon dioxide,

$$CO_2 + O^{2-} \rightarrow CO_3^{2-}$$

the assumption that $CO_2$ probes the basic properties of surface oxide ions seems reasonable. However, $CO_2$ forms monodentate and bidentate carbonates, probes cation/anion site pairs via bidentate carbonate formation [8-10], can form bent $CO_2^{\delta-}$ chemisorbates and linear $CO_2$ physisorbates [11]. Hence, it is clear that the interaction of $CO_2$ with oxide surfaces can be complex, and is not a simple probe of the basicity of surface oxide anions. To this end, experiments were initiated with another acidic probe molecule, $BF_3$, a strong Lewis acid.

**2.1.1.1 $CO_2$ adsorption on $Cr_2O_3$ (10$\bar{1}$2).** Few oxide single crystal surfaces have been shown to adsorb $CO_2$ strongly in UHV and form surface carbonates (see [12, 13] and references therein). For stoichiometric $Cr_2O_3$ (10$\underline{1}$2), $CO_2$ adsorption at 190 K leads to two thermal desorption features in temperature programmed desorption (TPD) as shown in Figure 1. A high-temperature feature at 395 K fills first, and is attributed to a bidentate surface carbonate species based on the literature for $CO_2$ adsorption on $\alpha$-$Cr_2O_3$ microcrystalline powders [14] which expose primarily (10$\underline{1}$2) surfaces [15, 16]. In agreement with infrared studies over $Cr_2O_3$ powders, $Cr^{3+}$-$O^{2-}$ site pairs are required for the formation of this surface complex. This site requirement is demonstrated by the lack of a high-temperature thermal desorption feature if the $Cr^{3+}$ cations are first blocked by an adlayer of terminal oxygen or chlorine atoms (Figure 1) [8, 10, 13]. While a strongly bound $CO_2$ (carbonate) species is often taken as an indication of a strong base site, it is clear from the involvement

of the cation in the 395 K desorption feature that $CO_2$ is not a simple probe of the basic properties of surface oxygen anions.

Weakly bound $CO_2$ adsorbates such as those observed on the stoichiometric (218 K) and oxygen-terminated (235 K) surfaces in Figure 1 have been observed over $Cr_2O_3$ powders [10, 13], but IR studies have failed to clarify the nature of the associated surface species. Suggestions include $CO_2$ physisorbates bound oxygen-end on [13], bent $CO_2^{\delta-}$ species bound at surface metal ions [10], and linear $CO_2$ species at surface $Cr^{3+}$ cation sites [10]. While linear or bent $CO_2$ species at cations are possible explanations for the low-temperature (218 K) desorption feature from the stoichiometric surface, the 235 K feature from the oxygen-terminated surface cannot involve an adsorbate at a cation site. The lack of $CO_2$ uptake on the chlorine-terminated surface indicates that the low-temperature adsorbate on the oxygen-terminated surface is associated with the terminal chromyl oxygen, not the more fully coordinated lattice oxygen available at the stoichiometric surface. Regardless of whether this adsorbate is best characterized as a monodentate carbonate, or a bent or linear $CO_2$ adsorbate, it is clear that $CO_2$ probes primarily the terminal chromyl oxide ions on the oxygen-terminated (10$\underline{1}$2) surface. However, given the differences in the bonding configurations between this adsorbate and the more stable (higher-temperature) bidentate carbonate on the stoichiometric surface, it is clear that the differences in desorption temperatures are not simple indicators of variations in the basicity of differently coordinated surface oxide ions.

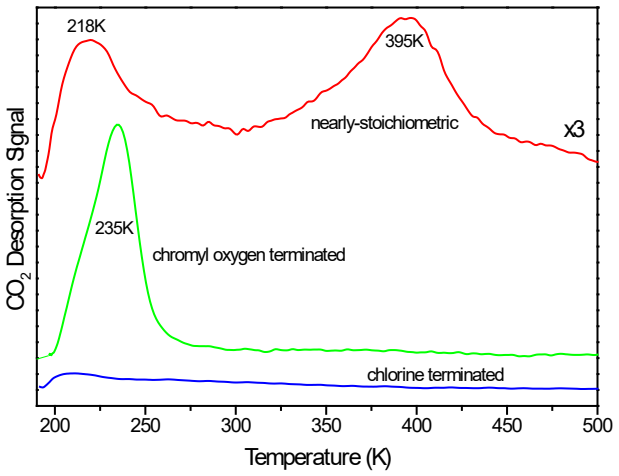


**Figure 1. $CO_2$ thermal desorption from differently-terminated $Cr_2O_3$ (10$\underline{1}$2) surfaces. All dose sizes are 5 L.**

**2.1.1.2 $BF_3$ adsorption on $Cr_2O_3$ (10$\bar{1}$2).** The Lewis acid $BF_3$ appears to give a more direct indication of the Lewis basicity of oxygen anions on $Cr_2O_3$ (10$\underline{1}$2). As shown in Figure 2, adsorption at 190 K on the stoichiometric surface gives a thermal desorption feature at 340 K ($\Delta H_{ads}$ = 21 kcal/mol [17, 18]) which is attributed to the three-coordinate oxygen anions in the outer atomic layer of the stoichiometric surface. Adsorption on the oxygen-terminated surface gives a similar feature in addition to a 500 K ($\Delta H_{ads}$ = 31.9 kcal/mol [17, 18]) desorption feature attributable to $BF_3$ adsorption at terminal chromyl oxygen adatoms. This result agrees with intuition in that the lone pair electrons on a singly-coordinate terminal oxide should be more accessible than those on a three-coordinate anion in the outer atomic layer of the stoichiometric surface. Interestingly, the heat of adsorption of $BF_3$ shows the reverse of the trend seen for $CO_2$ adsorption following oxygen termination of the surface, again demonstrating the difficulty of using $CO_2$ as a simple probe due to its variety of bonding configurations.

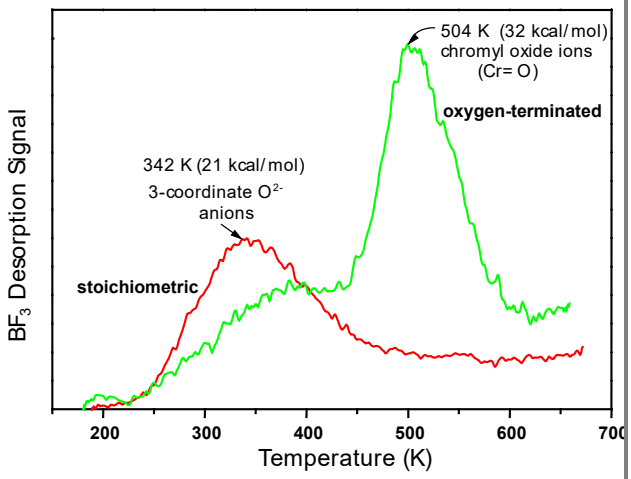


**Figure 2. $BF_3$ thermal desorption from stoichiometric and oxygen-terminated $Cr_2O_3$ (1012) surfaces.**

The use of $BF_3$ as a probe of $Cr_2O_3$ surface properties is not an entirely clean process. Small amounts of $F_2$ are generated, and boron is gradually deposited during successive thermal desorption runs. However, the deposited boron does not affect the $BF_3$ desorption temperatures.

**2.1.1.3 $NH_3$ adsorption on $Cr_2O_3$ (10$\bar{1}$2).** Previously, we had success using ammonia as a probe of the

"acidity" of surface cations on $SnO_2$ (110), and demonstrated that ammonia could distinguish between cations of different coordination, specifically four-coordinate $Sn^{2+}$ and five-coordinate $Sn^{4+}$ cations. $Cr_2O_3$ is generally considered to be an acidic oxide [19, 20], and high uptakes of ammonia have been observed on $Cr_2O_3$ powders with a large (60 kcal/mol) differential heat of adsorption [20], hence ammonia adsorption on $Cr_2O_3$ (10$\underline{1}$2) was investigated. Given the one simple coordination environment (i.e., five coordinate) of the $Cr^{3+}$ cations on this surface, it was thought that these measurements would provide a prototypical example of $NH_3$ adsorption as a probe of cation Lewis acidity on a well-defined oxide surface.

The results for ammonia adsorption on $Cr_2O_3$ (10$\underline{1}$2) were surprising. A heat of adsorption for $NH_3$ of 22.5 kcal/mol is found, but the saturation coverage following adsorption at 190 K is less than 3% of a monolayer (0.03 molecules per coordinately-unsaturated Cr surface cation). The results indicate adsorption at defects rather than the predominant five-coordinate $Cr^{3+}$ sites available on the stoichiometric surface. The nature of the adsorption sites is unknown, but they are most likely cations of lower coordination at some sort of point defect or step sites.

**2.1.1.4 $BF_3$ adsorption on $SnO_2$ (110).** The $SnO_2$ (110) surface exposes two primary types of oxygen anions. On the stoichiometric surface (Figure 3), two-coordinate bridging anions are exposed in the outer atomic layer, along with three-coordinate in-plane anions in the second atomic layer. On the reduced and defective surfaces (Figures 4 and 5), only three-coordinate oxygen anions are exposed, making it possible to probe the in-plane anions in the absence of the bridging anion layer.

As shown in Figure 6, adsorption on the reduced (110) surface gives rise to a $BF_3$ desorption feature at 310K ($\Delta H_{ads}$ = 19 kcal/mol [17, 18]) attributable to adsorption at three-coordinate in-plane oxygen anions. No $F_2$ desorption is observed. (Similar results are observed for the defective surface.) The heat of adsorption is within two kcal/mol of that observed for similarly coordinated anions on the $Cr_2O_3$ (10$\underline{1}$2) surface.

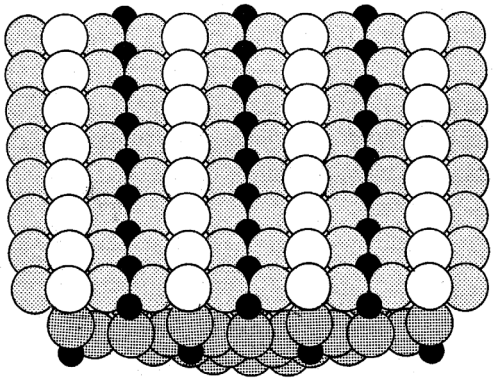

**Figure 3. Ideal, stoichiometric, $SnO_2$ (110) surface assuming no relaxation. The small black circles represent Sn cations while the larger open circles represent $O^{2-}$ anions.**

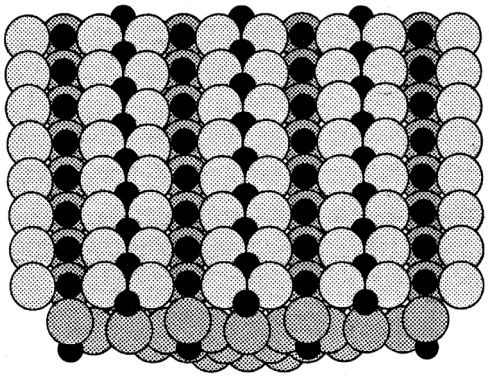

**Figure 4. "Reduced" $SnO_2$ (110) Surface assuming no relaxation.**

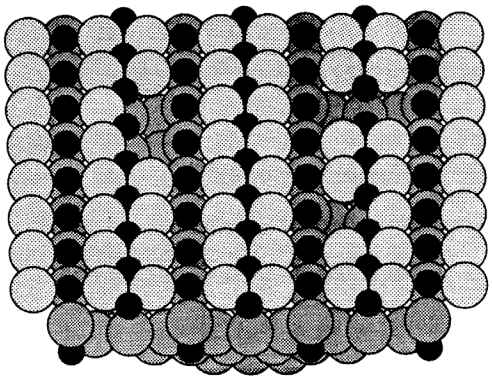

**Figure 5. "Defective $SnO_2$ (110) Surface assuming no relaxation.**

For the stoichiometric surface, a $BF_3$ desorption trace similar to that from the reduced surface is seen, demonstrating that no additional $BF_3$ desorption feature attributable to two-coordinate bridging oxygen anions is observed. The difficulty of probing bridging oxygen on the stoichiometric surface appears to be a result of the labile nature of these anions that makes possible their thermal removal from the clean surface between 350 K and 600 K [21]. In addition to $BF_3$, $F_2$ desorption is observed from the stoichiometric surface (none is observed from the oxygen-deficient reduce and defective surfaces), suggestive of a reaction between the bridging oxygen and $BF_3$. XPS of the surface boron left by this process (B 1s BE = 192.2 eV) indicates a boron oxide deposit [22] formed by the reaction of $BF_3$ with the bridging oxygen anions. These results suggest that the thermal stability of the oxide ion may be a reasonable indicator of whether $BF_3$ will

act as a molecular Lewis acid or as source for an atomic boron reducing agent following $BF_3$ dissociation. [Note that the terminal chromyl oxygen on $Cr_2O_3$ (10$\underline{1}$2) is stable in vacuum to temperatures above 1100 K].

### 2.1.2 Oxidation Chemistry on Well-Defined Oxide Surfaces

In the previous project, investigations of the oxidation chemistry of hydrocarbon fragments on metal oxide single crystal surfaces were proposed using alkyl halide adsorption and decomposition as a source of hydrocarbon fragments. This approach has been successfully applied to the study of hydrocarbon reactions over metals [23], but had, at that time, found little application in the study of metal oxide surface chemistry. Two directions of research have been explored: (1) the oxidation of chlorofluorocarbons over $Cr_2O_3$ (10$\underline{1}$2) and (2) the oxidation of hydrocarbon fragments over $SnO_2$ (110).

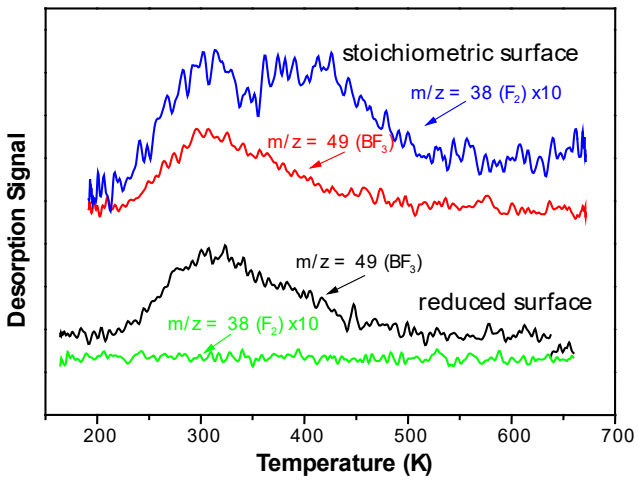


**Figure 6. $BF_3$ thermal desorption from stoichiometric and oxygen-deficient ("reduced") $SnO_2$ (110) surfaces.**

**2.1.2.1 Halocarbon reactions over $Cr_2O_3$ (10$\bar{1}$2).** $Cr_2O_3$ catalysts have found applications for a variety of reactions [14], but their use in the synthesis of alternative refrigerants to replace chlorofluorocarbons [24] illustrates the ability of $Cr_2O_3$ to catalyze halogen elimination and addition reactions. The reactions of a sequence of haloalkanes ($CFCl_2CH_2Cl$, $CF_2ClCH_2Cl$, and $CF_3CH_2Cl$) thought to be intermediates in the fluorination of trichloroethylene to 1,1,1,2 tetrafluoroethane ($CF_3CH_2F$ - refrigerant 134a) with HF have been investigated.

It was found that the reactivity of the molecules is controlled by the composition of the fully halogenated (i.e., non-hydrogen containing) methyl group. The observed reactivity trend ($CFCl_2$– > $CF_2Cl$– >> $CF_3$–) matches that expected from the literature on halocarbon activity, i.e., the more highly chlorinated the methyl group, the more reactive the C-Cl bonds [25-28].

For $CFCl_2CH_2Cl$ and $CF_2ClCH_2Cl$, the reactivity with $Cr_2O_3$ is significant. In thermal desorption experiments, the primary reaction for both haloalkanes is an oxidative 1,2 dichloro elimination to produce an alkene and deposit Cl on the $Cr_2O_3$ (10$\underline{1}$2) surface:

$$CFCl_2–CH_2Cl \rightarrow CFCl=CH_2 + 2\ Cl_s$$
$$CF_2Cl–CH_2Cl \rightarrow CF_2=CH_2 + 2\ Cl_s$$

The chemistry occurs via a reaction-limited process at 265 K (i.e., higher than the desorption temperature for the molecular alkanes and alkenes) that produces both the principle alkene product and a few percent of the alkane reactant [29]. The chemistry is readily explained by a dissociative adsorption step (C–Cl bond cleavage) followed by a rate-limiting β elimination:

These stoichiometric reactions proceed until the surface is deactivated by Cl via simple site-blocking of the surface $Cr^{3+}$ cations. No residual surface carbon is observed following the reaction, and no oxygenated products (CO, $CO_2$, etc.) are produced [29].

$$CFCl_2–CH_2Cl_{(g)} \xrightarrow[\text{adsorption}]{\text{dissociative}} \begin{array}{l} CH_2Cl \\ | \\ CFCl \\ | \quad + Cl_s \end{array} \xrightarrow[\text{elimination}]{\beta\text{-chloride}} \begin{array}{l} CFCl=CH_{2\,(g)} \\ + 2\ Cl_s \end{array}$$

The third haloalkane, $CF_3CH_2Cl$, does not react during thermal desorption experiments, it simply adsorbs and desorbs molecularly. However, during exposures at elevated temperatures (750 K), the activation barrier

to reaction is scaled and equal amounts of Cl and F are deposited on the surface until a saturation coverage of halogen (one adatom per surface $Cr^{3+}$ cation) is reached. While a mass spectroscopic determination of the product molecules was not possible because of the background partial pressure of the reactant, the one-to-one ratio of deposited Cl and F suggests a similar 1,2 dihaloelimination reaction to $CF_2{=}CH_2$.

In addition to the alkenes produced from the dehalogenation of the alkanes, trace amounts of acetylene are also produced. Thermal desorption experiments with $CFCl{=}CH_2$ and $CF_2{=}CH_2$ demonstrate that acetylene is produced by the further oxidation of the alkenes. On a clean $Cr_2O_3$ (10$\underline{1}$2) surface, acetylene is produced during thermal desorption studies of the alkenes in a reaction-limited feature at 475 K. As halogen is deposited on the surface, a desorption-limited acetylene feature at around 300 K also appears, indicating that deposited surface halogen promotes the reaction and lowers the activation barrier to acetylene production. Based on precedents from the organometallic literature, a pathway is proposed that involves dissociative adsorption (C–X bond cleavage) to form a surface fluorovinyl intermediate, $\alpha$-fluorine elimination to vinylidene, followed by a 2,1-hydrogen shift to acetylene. The Group VI transition metals (Cr, Mo, and W) are known to form vinylidene complexes [30, 31], and $\alpha$-elimination of halogen from halovinyl ligands is a well-known method for preparing these organometallic complexes [31, 32]. The final vinylidene

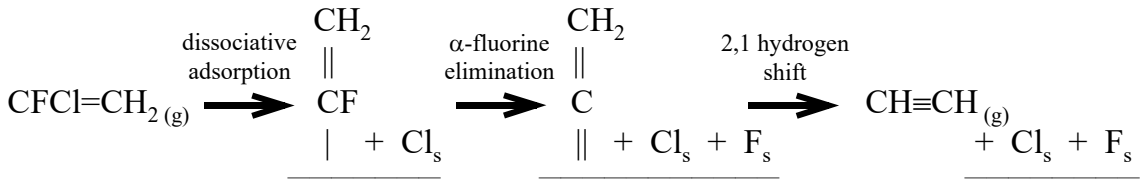


isomerization step (the 2,1-hydrogen shift) is the reverse of a reaction observed over Pt and Pd surfaces where a 1,2-hydrogen shift is observed when acetylene adsorption forms a surface vinylidene [33-35]. While vinylidene species on metal surfaces are consistently reported to decompose to $H_2$ and surface carbon rather than yield acetylene [33, 36-38], the minimal capacity of $Cr^{3+}$ cations on the (10$\underline{1}$2) surface to $\pi$-backbond [39] may lead to less weakening of the C=C bond and a different reaction pathway. This isomerization step is thought to be intramolecular since experiments with pre-adsorbed D atoms do not yield any deuterated acetylene, DC≡CH [29].

The chemistry typically reported for the steady state reactions of haloakanes over $Cr_2O_3$ catalysts includes isomerization, disproportionation and HX abstraction, and involves halogen exchange with the surface [40-45]. The observed alkane to alkene dehalogenation chemistry described above differs from most of these accounts, but is very similar to the zinc-catalyzed dehalogenation of vicinal dihalides used in organic synthesis [46]. The differences in our UHV studies and the traditional catalytic studies suggest that other reactions can occur between the reactants and the halogen adlayer at elevated temperature and pressure.

**2.1.2.2 Alkyl iodide reactions over $SnO_2$ (110).** In our initial investigations of the reactions of oxygenates on $SnO_2$ (110), an unexpected selectivity was observed. Of the alcohols and organic acids studied, the only reactions to occur were oxidative dehydrogenation and dehydration. Of the aldehydes and ketones investigated, only molecular adsorption and desorption was observed. None of these reactions require an oxygen insertion step. One of the goals of our work with $SnO_2$ was to determine the role of the two crystallographically inequivalent forms of lattice oxygen (bridging and in-plane) in the oxidation of hydrocarbons over $SnO_2$ (110), and their relationship to the selectivity of the oxidation process.

For this project, we began an investigation of oxygen insertion reactions by utilizing alkyl iodides to produce hydrocarbon fragments on $SnO_2$ (110). The intent was to examine the subsequent oxidation and decomposition chemistry as a function of surface condition, specifically in the presence and absence of bridging oxygen anions and in-plane oxygen vacancies. While hydrogenation and dehydrogenation reactions are usually observed for hydrocarbon fragments over metal surfaces [23], we expected primarily oxidation products over $SnO_2$ with shifting selectivity dependent on surface condition and available forms of surface lattice oxygen.

This work was started with methyl iodide, $CH_3I$, to allow a comparison of the reactions of methyl groups with those observed previously for methoxide formed via dissociative adsorption of methanol [1]. Our work has concentrated solely on the reactions of methyl iodide, as a result of problems encountered due to the low reactivity of this molecule and the small size (4 mm x 2.5 mm) of our $SnO_2$ single crystal surface. In thermal desorption experiments with $CH_3I$ over reduced and defective $SnO_2$ (110), the probability of thermally activating the oxidation reaction is small with conversions in a given run on the order of 1 to 2% as observed in thermal desorption and via XPS of deposited iodine. The only product identified from reduced and defective surfaces is dimethyl ether (DME) as shown in Figure 7. The small amount of DME product is reaction-limited and observed at 340 K in the high temperature tail of the molecular $CH_3I$ desorption signal where the surface coverage is extremely low. Electron irradiation (50 eV, $10^{17}$ $e^-/cm^2$) following adsorption removes approximately 90% of the $CH_3I$ adsorbate via electron-stimulated desorption, and shifts the DME desorption signal down by 60 degrees to 280 K. This lower temperature corresponds to a desorption-limited DME product [47, 48], and suggests that electron irradiation activates both C–I and Sn–O bonds.

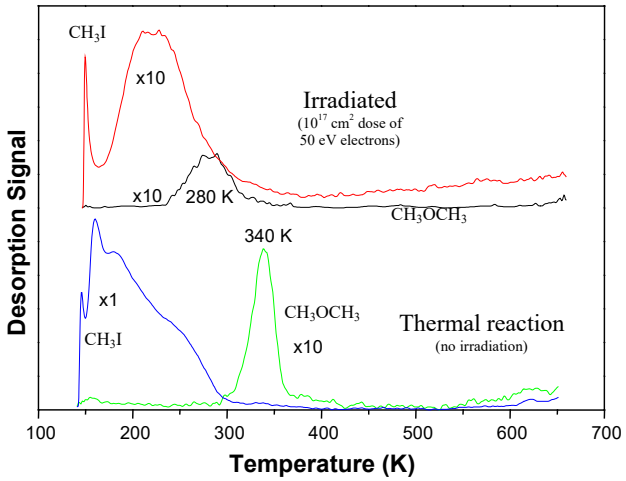


**Figure 7. Thermal desorption following a 5L doses on the reduced surface. Bottom spectra show the effects of thermal activation, while the top spectra show the effects of a $10^{17}$ $cm^{-2}$ exposure to 50 eV electrons.**

On the stoichiometric surface (not shown), similar quantities of DME are observed at 280 K (desorption-limited kinetics) **without** electron irradiation, in addition to a trace amount of formaldeyhyde, $CH_2O$, at 450 K. These results demonstrate that the labile bridging oxygen anions on the stoichiometric surface facilitate the thermal activation of methyl iodide. The formaldehyde desorption signal occurs in the same temperature range as that observed for the decomposition of methoxide to formaldehyde following dissociative adsorption of methanol at bridging at oxygen vacancies on the reduced surface [1], and indicates that the insertion of bridging oxygen anions into methyl groups to form methoxide.

The reaction of methanol to DME has been reported over the (114)-facetted $TiO_2$ (110) surface by Kim and Barteau [49]. The coupling of methoxide to DME in the presence of four-coordinate $Ti^{4+}$ cations appears to depend on the availability of two vacant coordination sites on the $Ti^{4+}$ cation. In our experiments, one can imagine this condition being met by a number of scenarios involving the reaction of lattice oxygen with $CH_3$ to produce a methoxide without any apparent change in the coordination number of the cation binding the methoxide. Given the small amount of product formed and the associated low coverage of reaction intermediates, we were unable to spectroscopically characterize these surface species. For the stoichiometric surface, the coupling of methoxides formed from bridging oxygen is the likely route to DME although methyl-methoxide coupling cannot be ruled out. On reduced and defective surfaces it is unclear which process is the most likely. To help resolve these issues we considered studying methyl idodide oxidation in the presence of preadsorbed methoxide formed by the dissociative adsorption of methanol. However, without higher yields of oxidation products from methyl iodide to probe the reaction pathway

these experiments had little chance of success. Also, the low reactivity of $CH_3I$ has caused difficulty in the search for other products (methyl radicals, methane, ethylene, carbon oxides, etc.) because of overlap in the cracking patterns with the methyl iodide reactant or the background signal at some values of m/z in the mass spectrum. These issues were never resolved.

### 2.1.3 Other Experimental Work

**2.1.3.1 STM investigation of $SnO_2$ (110).** While the presence of bridging and in-plane oxygen vacancies on the $SnO_2$(110) surface have been demonstrated experimentally [1, 21, 50], the details of the local geometric structure (extent of relaxation around the vacancies) and electronic structure in the neighborhood of these defects had not been reported in the literature at this point in the project. STM and STS (tunneling spectroscopy) were used in an attempt to investigate these details.

Problems were initially encountered tunneling to high-temperature annealed samples. For annealing temperatures where the ion-bombarded surface begins to form large terraces, the conductivity drops, and it is difficult to establish a tunneling current. [Note that unlike the case for $TiO_2$, $SnO_2$ does not undergo any significant bulk reduction by heating in vacuum. Hence, most of the changes in conductivity are associated with changes in surface properties.] The use of UV light from a Hg vapor lamp was used in an attempt to excite charge carriers to overcome problems with low sample conductivity.

Early attempts with UV irradiation were promising during runs in air with the lamp close to the sample, but were not successful in our UHV set up with a well-ordered sample. Atomic size features apparently related to the surface unit cell were imaged on small local regions of the surface, but no images of extended terraces were obtained [51]. There is one report in the literature of atomic resolution obtained by STM on the (4x1) reconstructed $SnO_2$ (110) surface (i.e., a "defective" surface) [52], indicating that these experiments should be doable although there is no information available about doping or the bulk conductivity of the sample. Naturally occurring cassiterite crystals with (110) growth faces [53] were also examined in the hopes that natural impurities would lead to a more conductive ordered surface. These attempts were also unsuccessful.

After a number of one-week-long sessions on the UHV STM in our Geological Sciences Department, it was recognized that we were not developing the required expertise for these measurements working on short time frames with a borrowed instrument. The experiments were concluded unsuccessfully.

**2.1.3.2 Adsorption of additional molecules on $Cr_2O_3$ (10$\underline{1}$2).** In addition to the work described in Sections 3.1 and 3.2 on $Cr_2O_3$ (10$\underline{1}$2), thermal desorption studies of atomic hydrogen, $H_2O$, $D_2O$ and CO were conducted on the nearly stoichiometric (10$\underline{1}$2) surface. Atomic hydrogen recombines at around 350 K to give $H_2$ with no formation of water via a reaction with lattice oxygen [29]. Submonolayer quantities of water adsorb dissociatively and recombine between 350 K and 425 K in thermal desorption experiments [51]. CO adsorbs weakly with a heat of desorption of 12 kcal/mol suggesting a predominantly $\sigma$ interaction and weak $\pi$ backbonding [39].

### 2.1.4 Computational Investigation of Oxide Surface Relaxations and Molecular Adsorption

In the early stages of this project we gained access to a much improved density functional code for periodic systems, the Vienna Ab-initio Simulation Package (VASP) [54-56], which utilizes efficient Vanderbilt ultrasoft pseudopotentials [57]. First-principles pseudopotential plane-wave total energy calculations were made using both the local density approximation (LDA) and the generalized gradient approximation (GGA) of Perdew et al. [58, 59] for the electronic exchange and correlation functional. These computational studies were originally undertaken to compliment the experimental STM/STS investigation.

**2.1.4.1 Bulk $SnO_2$.** Calculations were performed on a 48 atom $SnO_2$ cell to predict the fully-relaxed and energy optimized properties of the bulk. The LDA predicts a bulk geometric structure with lattice parameters slightly under, but within 1% of the experimental values as expected for the LDA. The GGA predictions for the bulk slightly overestimate the bulk lattice parameters, but by less than 1.5%. As expected for density-

functional theory [60], the bulk band gap is underestimated at 1.88 eV as compared to the experimental value of 3.6 eV.

**2.1.4.2 Relaxed $SnO_2$ (110) Surfaces.** Our predictions of the optimized geometric and electronic structure of the stoichiometric (Figure 3) and reduced (Figure 4) $SnO_2$ (110) surfaces are similar to those in the literature [61, 62]. In-plane relaxations are negligible, and symmetry-breaking reconstructions are not found. The most prominent geometric change is a small (0.15 Å) inward relaxation of five-coordinate cations, and a small outward relaxation (0.2 Å) of the in-plane anions and remaining cations (i.e., six-coordinate cations on the stoichiometric surface and four-coordinate cations on the reduced surface). In agreement with experiment [21], the calculations predict surface states low in the gap (i.e., near the valence band maximum) associated with the reduction of tin cations at the bridging oxygen vacancies for the reduced surface.

Predictions for the defective surface were unavailable in the literature at this point in the project. We examined a surface with one in-plane vacancy per unit cell, which equates to a (2x1) array of vacancies on the extended surface. Small in-plane relaxations accompany this defect, with the primary effect being a small (0.05 Å) relaxation of the three-coordinate cation (four-coordinate on the reduced surface before introduction of the in-plane vacancy) towards the defect. No symmetry-breaking reconstructions (other than that due to the introduction of vacancies) are observed, in-line with our earlier suggestions that the introduction of in-plane oxygen vacancies does not lead to a dramatic restructuring of the local coordination environment [21].

**2.1.4.3 $NH_3$ adsorption on reduced $SnO_2$ (110).** The adsorption of $NH_3$ on the reduced surface (Figure 4) was also investigated computationally for comparison to our experimental results which demonstrate the ability of this simple Lewis acid probe molecule to differentiate between four-coordinate $Sn^{2+}$ and five-coordinate $Sn^{4+}$ surface cations [4, 5]. GGA corrections were used for these computations since they typically give better results for surface/adsorbate systems than the LDA [63]. For these calculations the entire crystal/adsorbate system was energy optimized. It was found that neglecting the relaxation of the surface and optimizing only the adsorbate led to predicted heats of adsorption ~ 8 kcal/mol smaller than for the fully optimized case.

A simple atop site is predicted at the 5-coordinate cations with a $\Delta H_{ads}$ of 18.9 kcal/mol which compares favorably to the experimental values in the range of 18.5 to 22 kcal/mol. An atop geometry is also predicted along the rows of four-coordinate cations with a $\Delta H_{ads}$ of 20.5 kcal/mol, in poor agreement with the experimental value of 30 kcal/mol. In both cases, coordination of ammonia to the surface results in a 0.2 Å inward relaxation of the associated cation. Reasonable Sn–N bond lengths of 2.31 - 2.35 Å are predicted. The discrepancy in energy for adsorption at four-coordinate cations is thought to be related to the poor estimation of the bulk band gap by the calculations. The introduction of bridging oxygen vacancies on the reduced surface causes a stabilization of Sn 5s and 5p conduction band states to form occupied surface gap states with electron density in the bridging positions along the rows of four coordinate cations (i.e., at the vacancies) [61]. The stabilization of the conduction band states is underestimated because of the small band gap and the repulsion between these gap states and the ammonia at the atop site is apparently over predicted.

## 2.2 Results and Accomplishments 2/1/2000 – 1/31/2003

### 2.2.1 Reactions of C1 Hydrocarbon Fragments on α-Cr2O3 ($10\bar{1}2$).

The reactions of iodomethane, $CH_3I$ (and $CD_3I$), and di-iodomethane, $CH_2I_2$, were studied for insight into the reaction chemistry of methyl and methylene fragments, respectively, on $Cr_2O_3$ surfaces. On the stoichiometric ($10\bar{1}2$) surface exposing five-coordinate cations and three-coordinate anions, binding of these fragments occurs at metal cation sites as demonstrated by XPS (below). Dehydrogenation, hydrogenation and methylene coupling to ethylene are observed for both starting reactants, but no methyl fragment

coupling to ethane is observed. The halogen adatoms deposited by halocarbon dissociation cap the single coordination vacancies on the surface cations, and eventually shut down the surface chemistry via site blocking after sufficient exposure and reaction.

Reactions of both fragments on the chromyl oxygen (Cr=O) terminated surface give $CO_2$ and formic acid, HCOOH, as major products above 700 K. The recurring presence of $CO_2$ and formic acid are clear indications of the tendency for surface formate (HCOO) formation from terminal chromyl oxygen, in agreement with the results for formic acid decomposition (section 2.2.2.2) that gives $CO_2$ as a primary oxidation product.

**2.2.1.1 $CH_3I$ adsorption and the reaction of $CH_3$ fragments on stoichiometric ($10\bar{1}2$).** Iodomethane dissociation occurs below 250 K, as is clearly observed with XPS (see Figure 8). XPS following the adsorption of a monolayer coverage of $CH_3I$ at 120 K on stoichiometric $Cr_2O_3$ ($10\bar{1}2$) gives an I $3d_{5/2}$ binding energy of 620.2 eV. Heating to 250 K removes the molecular $CH_3I$ in the monolayer, and gives an I $3d_{5/2}$ binding energy of 619.2 eV for the remaining species. The 1.0 eV shift to lower binding energy is characteristic of I adatoms resulting from the dissociation of $CH_3I$ [22,23]. Following dissociation, a C 1s binding energy of 283.9 eV is observed which demonstrates that the binding sites of the remaining surface fragments are metal (cation) sites rather than the three-coordinate oxygen anions available on the stoichiometric surface. Binding energies near 286.4 eV [24] would be expected for methoxide-like $CH_3$ fragments bound at surface oxygen anions.

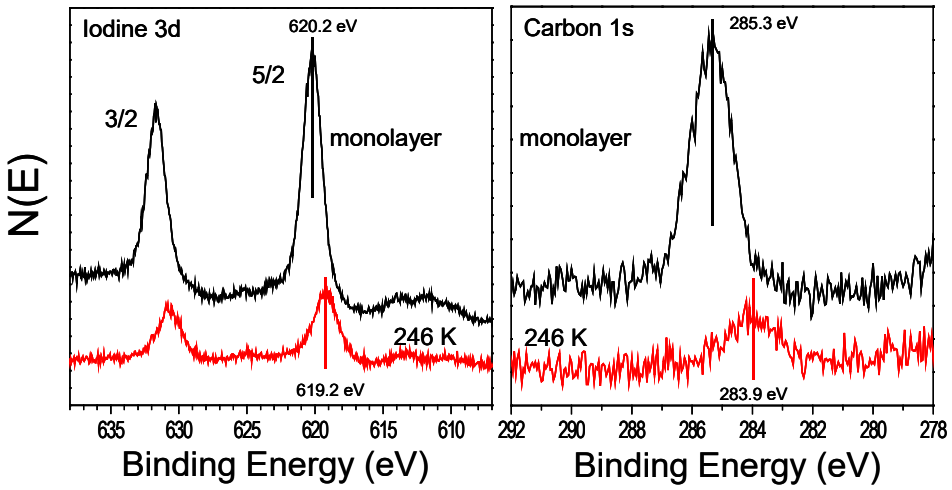


**Figure 8. XPS illustrating the dissociation of iodomethane. All spectra are referenced to a Cr $2p_{3/2}$ BE of 576.9 eV.**

The chemistry of methyl fragments on stoichiometric $Cr_2O_3$ ($10\bar{1}2$) is similar to that seen on metallic Cu surfaces [25] where α hydride elimination is the rate limiting step in the formation of methane from methyl fragments. As shown in Figure 9, the simultaneous desorption of $H_2$, $CH_4$ and $CH_2$=$CH_2$ at 515 K indicates a rate limiting methyl fragment dehydrogenation process (α hydride elimination) that liberates H atoms for reaction to $H_2$ ($D_2$) with other H (D) atoms, or $CH_3$ ($CD_3$) fragments to form methane by reductive elimination. Methylene fragments, $CH_2$, generated by the initial methyl fragment C-H bond cleavage couple with other fragments to form ethene. Since the parent mass for CO and ethene are the same (m/z = 28), experiments with deuterated

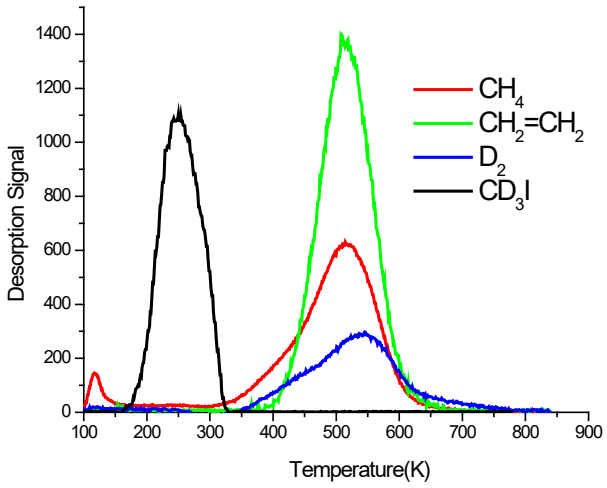


**Figure 9. Thermal desorption of 0.1 L dose of $CD_3I$ from a fresh stoichiometric (1012)**

iodomethane, $CD_3I$, have been used to confirm the occurrence of deuterated ethylene as the product rather than CO, which is also a reasonable candidate product molecule over an oxide surface. Dihydrogen production is peaked at slightly higher temperatures (~ 540 K) than the methane and ethylene products (515 K), suggesting that continued fragment dehydrogenation may result in surface carbon as a dehydrogenation product, as confirmed by post reaction AES analysis.

The lack of oxygenated products (CO, $CO_2$, $H_2CO$, $H_2O$) from the stoichiometric surface is **NOT** unexpected since adventitious surface carbon contamination must be sputter removed rather than burned off by simple heating in vacuum [19]. The observation of $H_2$ as a reaction product rather than $H_2O$ is another indication of the lack of reducibility of this surface under the conditions of our study.

The observed coupling reaction to ethylene **WAS** unexpected. Site requirements for coupling reactions and C-C bond formation on oxides surfaces are typically thought to involve multiple coordination vacancies on a single cation to bind the ligands involved in the coupling reaction [26] or require ligands on closely-spaced neighboring cation sites. The separation between cation sites on the nearly stoichiometric surface is greater than 4.5 Å, a farther distance than one would expect to allow coupling between adjacent sites without some mobility of the surface species. However, we see no indication in thermal desorption for gas phase radicals (i.e., no unaccounted-for m/z 15 signals that might indicate $CH_3$ radical desorption) or carbenes (unaccounted for m/z 14 signals), indicating that the coupling products originate from surface reactions. Note that ethylene is a major product of the reaction of methyl fragments, not just a trace product that could be easily explained by reactions at minority surface sites such as steps or under-coordinated cations associated with surface oxygen vacancies.

The coupling mechanism is not fully understood. The two most likely pathways are direct methylene coupling to ethylene, and methyl/methylene coupling to a surface ethyl fragment followed by β-hydride elimination to ethylene. We believe both pathways are operable, with the results for the reaction of $CH_2I_2$ (see below) also being suggestive of direct methylene coupling. The production of ethene but no ethane suggests that methylene fragments are mobile, but that methyl fragments dehydrogenate (or react with surface H to form methane) before overcoming the barrier to surface diffusion or radical desorption. Given that barriers to β hydride elimination are usually much lower than those for α elimination [15], any ethyl fragments formed by methyl/methylene coupling should undergo immediate β hydride elimination to ethene. We plan to test this possibility in the remaining six months of the current project period by studying the reaction between coadsorbed $CH_2$ and $CD_3$ (from $CH_2I_2$ and $CD_3I$, respectively) to look for a $CH_2$=$CD_2$ reaction product following the approach of Bent and coworkers [27]. Work with ethyl fragments (see below) is required to check the activation barrier to β hydride elimination.

**2.2.1.2 $CH_2I_2$ adsorption and the reaction of $H_2C$ fragments on stoichiometric ($10\bar{1}2$).** Di-iodomethane dissociates on the stoichiometric ($10\bar{1}2$) surface to give surface methylene fragments, $H_2C$, which couple at 415 K to give ethylene as the primary product (Figure 10). The temperature for ethylene evolution is 100 K lower than that observed from $CH_3I$, in agreement with the assignment of methyl fragment dehydrogenation as a higher temperature rate-limiting step in ethene (and methane) production from methyl fragments and $CH_3I$. Methylene dehydrogenation also occurs, liberating H atoms, which in turn hydrogenate remaining methylene fragments to methyl fragments. Methane is produced at the same temperature observed for the formation of methane from methyl fragments and $CH_3I$. No acetylene

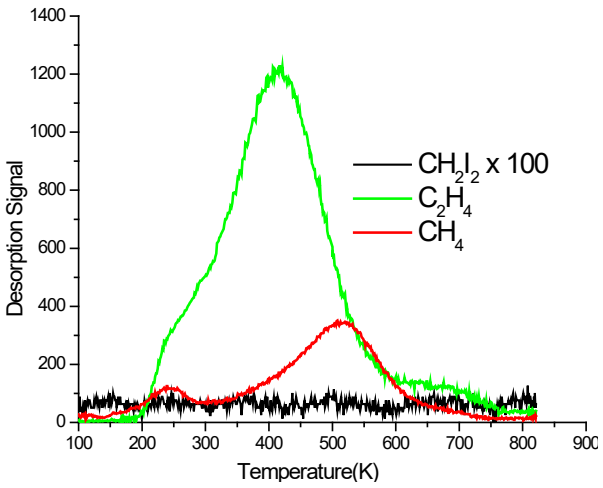


**Figure 10. Thermal desorption of 0.1 L dose of $CH_2I_2$ from a fresh stoichiometric ($10\underline{1}2$) surface.**

is observed as a reaction product, suggesting that the dehydrogenation of methylene to methyne (CH) likely continues to surface carbon. As seen for the reaction of methyl fragments, surface carbon is observed via post reaction AES analysis as a product of the dehydrogenation of methylene fragments.

**2.2.1.3 Reactions of $CH_3$ and $H_2C$ fragments on oxygen terminated ($10\bar{1}2$).** The reaction of $CH_3I$ and $CH_2I_2$ with the chromyl oxygen (Cr=O) terminated surface show some key similarities in product formation and desorption temperatures. Both molecules and their related hydrocarbon fragments undergo oxygen insertion by terminal oxygen, and produce a variety of oxygenated product molecules not seen from the stoichiometric surface that exposes only 3-coordinate anions.

Results for the reaction of $CH_2I_2$ are shown in Figure 11 to illustrate some typical details of the thermal desorption chemistry observed for both molecules. $CO_2$ is a principle product, produced at about 730 K, along with formic acid, HCOOH, at the same temperature. This reaction chemistry is characteristic of a rate limiting surface formate (HCOO) dehydrogenation as seen for formic acid (below). Small amounts of formaldehyde, $H_2C=O$, can be observed at around 450 K, similar to the lower temperature desorption state observed following formaldehyde adsorption (below), with a tail extending to higher temperatures. CO is also observed as a product in two temperature ranges. The results indicate that terminal (Cr=O) oxygen insertion can lead to both selective and nonselective oxidation, although complete oxidation is favored.

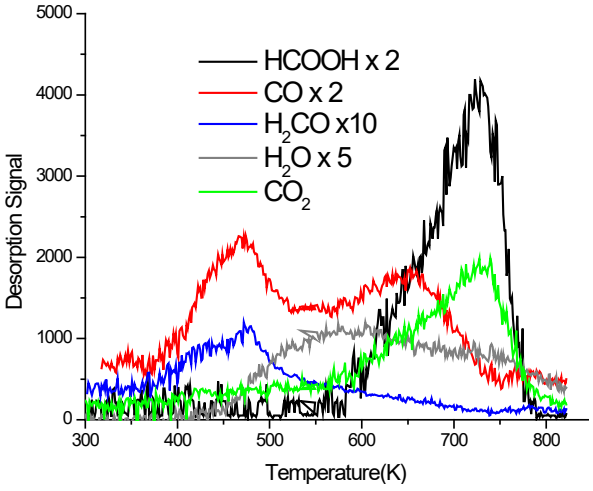


**Figure 11. Thermal desorption of 0.2 L $CH_2I_2$ from a freshly oxygen terminated ($10\underline{1}2$) surface.**

The reaction of both fragments with the chromyl oxygen terminated surface also leads to $H_2O$ formation in a broad desorption feature above 450 K, over the same wide temperature range where dehydrogenation of oxygenated intermediates yields CO and $CO_2$. These reaction products clearly indicate the much higher reactivity of terminal oxygen with both hydrogen and surface hydrocarbon fragments, compared to the three coordinate anions available on the stoichiometric surface. Note that while the terminal oxygen species is thermally stable to over 1100 K in vacuum, its greater tendency for nucleophilic attack on hydrocarbon fragments and its ready chemical removal by hydrogen as water matches well with our previous demonstration (using acidic $BF_3$ as a probe molecule) that terminal chromyl oxygen is a stronger Lewis base than three coordinate oxygen anions on the stoichiometric surface [28].

The product distributions (selectivity) and temperature ranges observed for the reaction of the two hydrocarbon fragments over the O-terminated surface are sensitive to dose size, sample history (total exposure and number of consecutive doses) because of the removal of terminal oxygen as carbon oxides (CO and $CO_2$), hydrocarbon oxygenates (HCOOH and $H_2CO$) and water. In consecutive runs, the production of $CO_2$ and other oxygen containing product molecules decreases as terminal oxygen is removed by reaction. As oxygen containing products drop off, the (de)hydrogenation and coupling products appear as surface cation sites are chemically uncovered and coordinately unsaturated cations sites become available. While the desorption traces are highly dependent on the exact surface condition, the oxygenated products from the hydrocarbon fragments tend to be seen (as the surface condition evolves) in the same temperature ranges observed for the reaction of hydrocarbon oxygenates shown below. This observation demonstrates that oxygenates provides a convenient starting place for understanding the chemistry of hydrocarbon fragments following nucleophilic attack by terminal oxygen.

## 2.2.2 Reactions of $C_1$ Hydrocarbon Oxygenates on α-$Cr_2O_3$ ($10\bar{1}2$).

The adsorption of oxygenates such as alcohols and carboxylic acids provides a means of accessing specific oxygenated surface intermediates to allow a characterization of their associated reaction pathways and selectivity. Reaction pathways for selective and non-selective oxidation of hydrocarbons following oxygen insertion may include alkoxide ($RCH_2O^-$), carboxylate ($RCOO^-$), carbonate ($CO_3^{2-}$) and other oxygenated surface intermediates. The dissociative adsorption of alcohols and carboxylic acids on oxides surfaces typically occurs via heterolytic O-H bond breaking to form alkoxides from alcohols [24,26,29,30], and carboxylates from carboxylic acids [29,31-34]. The reactions of three $C_1$ hydrocarbon oxygenates have been studied: (1) methanol ($CH_3OH$, $^{13}CD_3OD$, and $CH_3{}^{18}OH$), (2) formic acid (HCOOH), and (3) formaldehyde ($H_2CO$).

**2.2.2.1 $CH_3OH$ adsorption and the reaction of $CH_3O$ (methoxide) on stoichiometric ($10\bar{1}2$).** The dissociative adsorption of methanol to methoxide, $CH_3O^-$, on the stoichiometric surface provides a complementary view of the oxidation of methyl fragments, $CH_3$, on the oxygen terminated surface. Since oxygen insertion and the formation of oxygenated products from $CH_3I$ are only observed in the presence of terminal chromyl oxygen, the binding of methyl fragments to a terminal chromyl oxygen is the likely starting point for oxygen insertion and the subsequent reactions of $C_1$ fragments over the ($10\bar{1}2$) surface. Similarly, the dissociative adsorption of methanol on the stoichiometric surface occurs with the loss of the acidic proton that binds at a surface anion site to form OH, while the methoxide binds to a neighboring cation site. Given the single coordination vacancy of the 5-coordinate cations on the stoichiometric surface, a methoxide formed by methanol dissociation on the stoichiometric surface should be chemically identical to a methyl fragment bound by a chromyl oxygen on the O-terminated surface.

Methanol ($CH_3OH$) thermal desorption experiments from the stoichiometric surface give an array of hydrogenation, dehydrogenation, and nonselective oxidation products. For product identification purposes, isotopic labeled methanol ($^{13}CD_3OD$) was also used to distinguish between a number of different hydrocarbons and carbon oxides (ex, the parent masses of $CD_2{=}CD_2$ and CO products are easily separated for the deuterated and $^{13}C$ containing reactants, although both products have a parent m/z ratio of 28 for unlabeled reactants and CO and $CH_2{=}CH_2$ products).

For monolayer coverages (0.8 L dose), methanol desorption is observed in two primary temperature ranges: (1) below 300 K, and (2) 400-500 K as shown in Figure 12. XPS measurements for monolayer coverages on the stoichiometric ($10\bar{1}2$) surface show evidence of a mixed monolayer of molecular and dissociated methanol. Removal of molecular species by heating to 300 K leaves a surface species with a C 1s binding energy characteristic of methoxide, $CH_3O^-$. The desorption of methanol between 400 and 500 K, and the tail to higher temperatures (excluding the shoulder at 650 K) is similar to the temperature range and shape observed for the recombination of dissociated water [35], and is attributed to methoxide/hydrogen recombination.

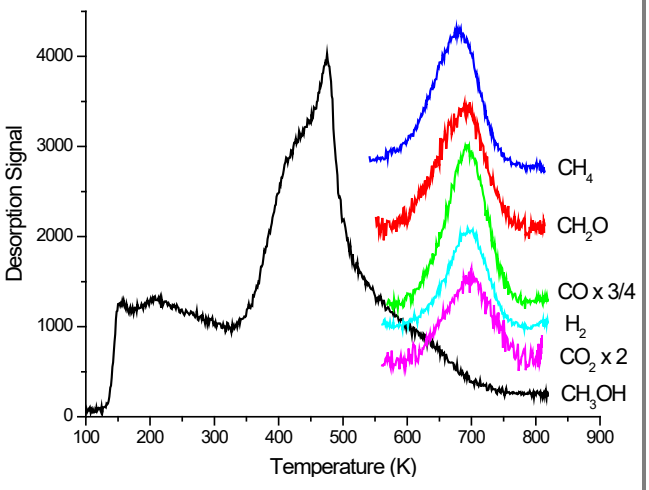


**Figure 12. Thermal desorption of 0.85 L $CH_3OH$ on a stoichiometric ($10\underline{1}2$) surface.**

The products occur within a narrow range of peak temperatures with maxima between 680 K and 700 K. A methane desorption feature is centered around 680 K, with the remainder of the features centered near 690-700 K. The formaldehyde desorption feature (690 K) is the broadest, with its leading and trailing edges encompassing the other entire product desorption features.

$^{18}$O-labeled methanol was used to examine the chemistry associated with the high temperature desorption features between 680 K and 700 K, as shown in Figure 13. For a fresh stoichiometric surface, dosed $CH_3{}^{18}OH$ gives equal quantities of $C^{16}O$ and $C^{18}O$, along with equal amounts of $H_2C^{16}O$ and $H_2C^{18}O$. The $^{16}$O in these products originates from oxygen atoms initially in the form of 3-coordinate surface lattice oxygen, while the $^{18}$O containing products include oxygen from the labeled molecular methanol. The equivalent amounts of labeled and unlabeled product give a clear indication of a symmetric surface reaction intermediate with two equivalent C-O bonds, each with an equal probability of cleavage to give formaldehyde and CO. The most likely intermediates are dioxymethylene, $H_2COO$ and formate, $HCOO^-$. By comparison to the chemistry for formaldehyde and formic acid reactants (below), the significant selectivity to formaldehyde and methane in this temperature range clearly argue in favor of dioxymethylene as the dominant bidentate surface intermediate. The production of these molecules is nonexistent (methane) or in trace amounts (formaldehyde) from the reaction of formate (below).

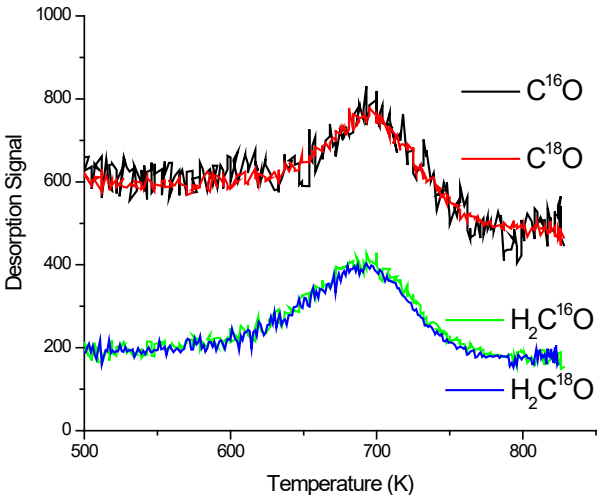


**Figure 13. Thermal desorption of 0.25 L $^{18}$O-labeled methanol ($CH_3{}^{18}OH$) from a fresh, stoichiometric surface.**

**2.2.2.2 $H_2CO$ adsorption and the reaction of $H_2CO_2$ (dioxymethylene) on stoichiometric (10$\bar{1}$2).** As shown in Figure 14, the adsorption and reaction of formaldehyde, $H_2CO$, gives rise to a similar product spectrum at high temperature (670-715 K) as observed from the decomposition of methanol. In addition to a coverage dependent low temperature formaldehyde desorption signal below 500 K (not shown), a high temperature formaldehyde desorption feature is observed at 695 K, similar to that seen for the production of formaldehyde from methanol, and clearly related to the same symmetric dioxygenated (bidentate) surface intermediate. If the surface is Cl terminated by reaction with 1,1,2-trichloro-1-fluoroethane to cap the surface $Cr^{3+}$ cation sites [20], no high temperature desorption features are seen and no reaction chemistry are observed, indicating that a cation-anion site pair is required for the formation of the dioxygenated surface species. This species is formed, therefore, by coordination of the formyl O in formaldehyde with a metal center, and nucleophilic attack of 3-coordinate surface lattice oxygen on the electron deficient carbon center. Note that molecular formaldehyde bound in such a site has the composition of dioxymethylene, $H_2CO_2$. We have observed a similar cation-anion site pair interaction with $CO_2$ which forms a bidentate carbonate that is stable above room temperature in UHV [36], as shown in Figure 15.

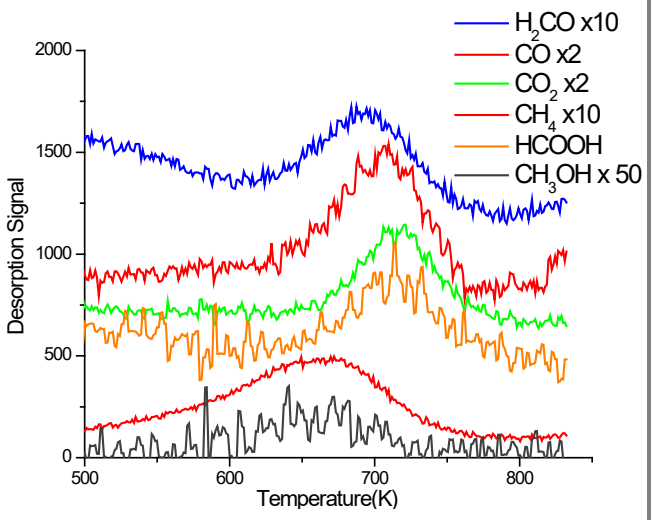


**Figure 14. Thermal desorption of 0.1 L $CH_2O$ from the stoichiometric surface.**

In addition to formaldehyde desorption, methane desorption is observed at a lower temperature with a broad peak centered around 670 K, along with a trace amount of methanol which desorbs at the same temperature. CO and $CO_2$ are observed concurrently with formaldehyde, but centered at slightly higher temperatures of 705 and 715 K, respectively. Formic acid, HCOOH, is also observed, coincident with the $CO_2$

feature.

The occurrence of hydrogenation products, $CH_4$ and $CH_3OH$, indicates hydrogenation of adsorbed formaldehyde (dioxymethylene) to methoxide, and subsequent hydrogenation of methoxide to methane [37] or methanol. (Methane formation by the reaction of methyl fragments at cation sites is ruled out because no concurrent ethylene desorption is observed, as seen with the reaction of methyl fragment from $CH_3I$ and $CH_2I_2$ at metal sites.)

The CO and $H_2$ observed at slightly higher temperatures than formaldehyde desorption indicates dehydrogenation of dioxymethylene. The concurrent desorption of $CO_2$ and formic acid is indicative of a formate intermediate (see below for the reaction of formic acid), and indicates that dioxymethylene dehydrogenates to formate. Subsequent dehydrogenation of formate yields $CO_2$, while the hydrogen released from $H_2CO_2$ and HCOO can also react with surface formate to form formic acid. The observed chemistry, hydrogenation and dehydrogenation of dioxymethylene is characteristic of a Cannizzaro-type disproportionation of dioxymethylene (Scheme 1) [38]:

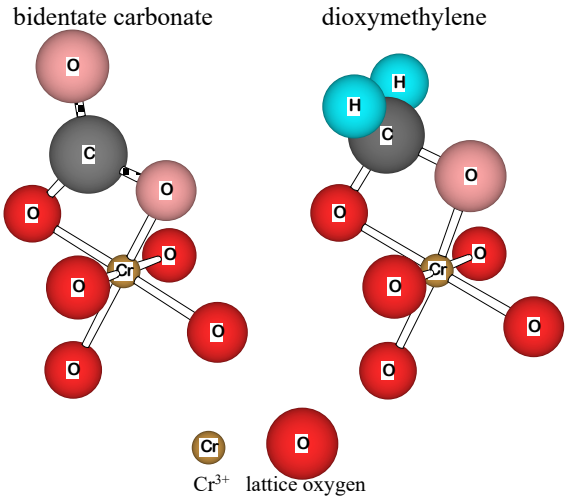


**Figure 15. Cartoon depicting the similarities between $CO_2$ adsorption as a bidentate carbonate, and formaldehyde adsorption as a dioxymethylene.**

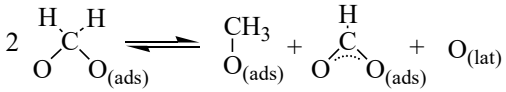

**Scheme 1. Cannizzaro type disproportionation of dioxymethylene to methoxide and formate.**

**2.2.2.2 HCOOH adsorption and the reaction of HCOO (formate) on stoichiometric ($10\bar{1}2$).** Monolayer coverages of formic acid yield a small, low temperature (~250-300 K) formic acid desorption signal associated with the desorption of a molecular formic acid adsorbate, and a higher temperature feature (~715 K) due to the recombination of formate and hydrogen (Figure 16). The reaction of formate prepared by the dissociative adsorption of formic acid gives a product slate of CO and $CO_2$ at high temperatures from the decomposition of surface formate, $HCOO^-$. Water and CO are formed at 685 K, a net dehydration reaction, while $CO_2$ and formic acid are evolved at 715 K, as observed in the reaction of formaldehyde. Trace fomaldehyde is also observed, and desorbs in a broad feature overlapping the two temperature ranges associated with CO and $CO_2$ production. The formaldehyde desorption over the entire temperature range indicates that the dehydrogenation steps associated with formate decomposition can lead to the concurrent hydrogenation of near trace amounts of formate to dioxymethylene, although dehydration and dehydrogenation are the major pathways. The lack of any methane or methanol (as observed for the reaction of formaldehyde) indicates that insufficient hydrogen is available to drive the further hydrogenation of dioxymethylene to methoxide, consistent with the starting molecular composition.

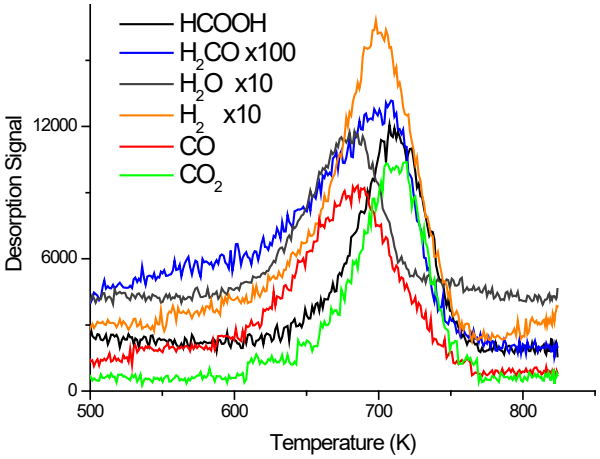


**Figure 16. Thermal desorption of 1.3 L HCOOH on the stoichiometric surface.**

**2.2.2.3 Summary of reaction pathways of $C_1$ oxygenates on stoichiometric ($10\bar{1}2$).** The high temperature reactions (600-725K) of methanol, formaldehyde, and formic acid involve three primary surface intermediates: (1) methoxide ($CH_3O^-$), (2) dioxymethylene ($H_2CO_2$), and formate ($HCOO^-$). Methoxide from methanol dissociation undergoes nucleophilic attack by 3-coordinate surface lattice oxygen on the stoichiometric surface to form dioxymethylene. Dioxymethylene from formaldehyde adsorption is both hydrogenated to methoxide and dehydrogenated to formate in a Cannizzaro-like disproportionation. Formate from formic acid can be hydrogenated to dioxymethylene, but only in trace amounts due to the unavailability of hydrogen for the reaction. It is, however, clear that interconversion between these three oxygenated surface intermediates is operable (Scheme 2), and provides connectivity to the reaction pathways to both selective and nonselective oxidation products.

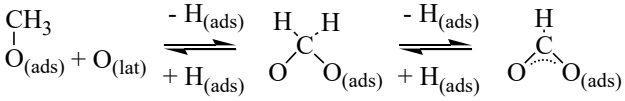


**Scheme 2. Connectivity between oxygenated surface intermediates. Dioxymethylene is the key intermediate.**

## 2.2.3 Computational Investigations of Oxide Electronic Structure

In a previous project period our computational work was aimed at understanding the geometric and electronic structure of stoichiometric and defective $SnO_2$ (110) surfaces, and ammonia chemisorption at cation sites of varying coordination on those surfaces to complement our experimental studies of that system [39]. In the current project period, that work was extended to include the examination of 3-D spatial distributions of valence electronic charge densities and the electron localization function (ELF) [40-43]. In collaboration with members of the VT Computer Science Department, a WINDOWS® based application was developed [44] for the direct 3-D visualization of output files from VASP (the Vienna Ab-initio Simulation Package [45-48]), a periodic, plane-wave density functional code which utilizes Vanderbilt ultrasoft pseudopotentials [45,49]. The viewer provides 3D isosurface images at user specified values of the charge density or ELF, and/or slices that display variations in these scalar quantities on a given plane through the structure.

Our predictions of the relaxations of $SnO_2$ (110) surfaces are in line with the growing number of computational studies of the geometric and electronic properties of stoichiometric and oxygen deficient surfaces [50-59]. While our calculations reproduce the typically small relaxations seen by others, the topological analysis of the electronic structure afforded by the visualization tool and the ELF provide insight into the chemical consequences of the composition variations and the origins of the relaxations that are observed for this rutile-structured material.

On the stoichiometric surface (Figure 17), the ELF describes regions of localization in the electronic structure of outer layer bridging (2-coordinate) oxygen that include a "banana-shaped" lone pair feature extending across the apex of the Sn-O-Sn bond. As the ELF is increased, this feature separates into two irreducible localization domains ("attractors" [42]) representative of two lone pairs on opposite sides of the plane of the Sn-O-Sn bond. These features invite a comparison to the 2-coordinate oxygen in molecular water and the distribution of Lewis electron pairs [60] assumed in the VSEPR (valence shell electron pair repulsion) model [61] for molecular structure.

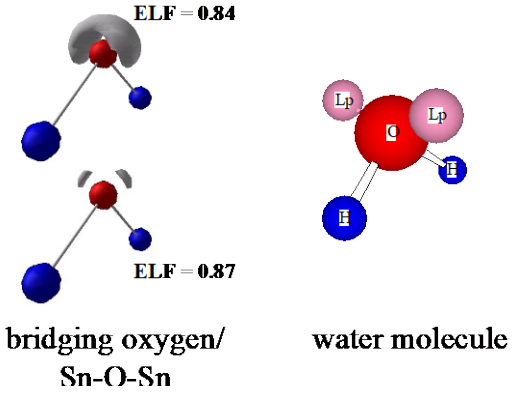


**Figure 17. ELF of a 2-coordinate bridging oxygen from the surface of rutile-structured $SnO_2$(110) compared to the molecular analog water.**

The predominant relaxations observed on the stoichiometric and reduced (110) surfaces are small (0.15 Å) inward relaxations of five-coordinate cations, and small outward relaxations (0.2 Å) of 3-coordinate in-plane anions and remaining cations (i.e., 6-coordinate or 4-coordinate cations on the stoichiometric or reduced surface, respectively). The oxygen anion and three nearest neighbor tin cations are all coplanar in the bulk structure, but at the surface the relaxation moves the anion slightly out of plane and away from the surface towards the vacuum. Examination of the spatial distribution of both the valence charge density and the ELF (Figure 18) shows equivalent local maxima above and below the plane for the coplanar structure in the bulk, while a local maximum appears above the apex of the out-of-plane 3-coordinate surface anion. This lone pair feature at the apex of the out-of-plane anion matches expectations for $H_3O^+$, a 3-coordinate molecular analog. The similarities between the

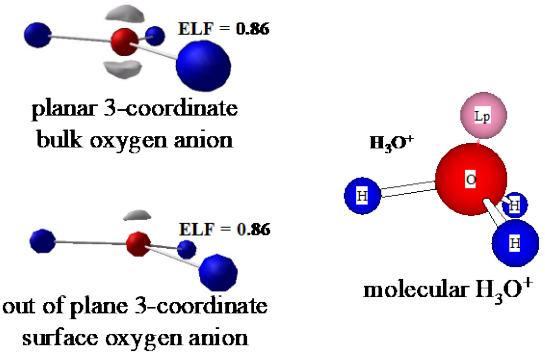


**Figure 18. ELF distribution about 3-coordinate planar (bulk) anion and relaxed surface anion. The molecular $H_3O^+$ analog is shown for comparison.**

surface anions and the oxygen atoms in the molecular systems suggests that the relaxations on this extended ionic surface can be qualitatively understood in terms of a VSPER model and the local geometric structure primarily about the anions.

Removal of the outer layer of bridging oxygen from the stoichiometric $SnO_2$ (110) surface gives a "reduced" surface with exposed 4-coordinate $Sn^{2+}$ cations. While polarization of the charge density above these $Sn^{2+}$ cations has been reported [57], the spatial distribution of the ELF gives a clear picture of a lone pair extending above the surface from the $Sn^{2+}$ cation (Figure 19). This picture is in line with the known coordination chemistry of $Sn^{2+}$ compounds, where 4-coordinate $Sn^{2+}$ is expected in trigonal bipyramidal coordination (as observed on the reduced surface) with one coordination position occupied by a stereochemically active lone pair [62].

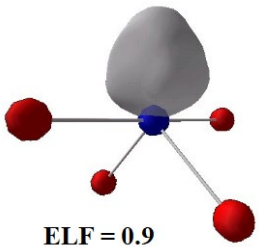


**Figure 19. ELF showing $Sn^{2+}$ lone pair for a 4-coordinate tin cation at a bridging oxygen vacancy on $SnO_2$(110).**

Of the three cations coordinating an in-plane (or relaxed out-of-plane) surface oxygen anion, the two equivalent 5-coordinate cations are in a formal 4+ oxidation state, while the single 4-coordinate cation is 2+, as described above. Removal of the surface oxygen at the center of such a site creates an in-plane oxygen vacancy, and the coordination of the cations adjacent to the vacancy is reduced. Since tin does not form 3+ and 1+ oxides [62], it has been suggested previously that the two electrons required for charge neutrality following the removal of a neutral O atom could be bound to the vacancy (i.e., shared between the three adjacent cations) to create a surface color center [63]. While the associated electronic states are ionizable at room temperature (the sheet conductance increases with the introduction of in-plane oxygen vacancies [63]), the ground state (0 K) spatial distribution for the ELF (Figure 20) clearly illustrates the localization of additional charge about each adjacent cation with the charge directed into the vacancy. This illustration is remarkably similar to the classic picture of a color center sharing charge between adjacent cations [64].

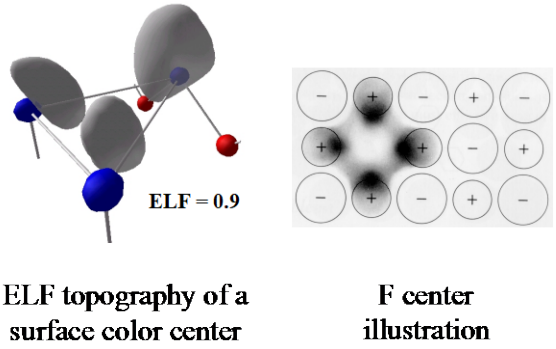


**Figure 20. ELF distribution of a color center at an in-plane oxygen vacancy on $SnO_2$(110). Kittel's representation of a bulk color center is shown for comparison [64].**

The examination of electronic structure calculations for the $SnO_2$ (110) surface by visualization of the ELF and valence charge densities suggests this approach will provide useful insight into the chemical properties of oxide surfaces. However, the electron localization function of Becke and Edgecombe [43] provides an inherently qualitative view of bonding and electron pairs since this scalar quantity is more or less arbitrarily defined between zero and one. {Note: The homogeneous electron gas is used as a reference state for perfect delocalization and is associated with an ELF value of 0.5 [42,65]. A value of 1 corresponds to perfect localization [41,65], and values less than 0.5 occur in regions between concentrations of electron density [65].} Since the shapes and sizes of the isosurfaces are sensitive to the value of ELF to which they correspond, and small variations in geometry can affect the nature of the isosurfaces for a fixed value of ELF, an investigation was undertaken to gain experience in the variability of the ELF with bonding geometry in oxides and the relationship between changes in bonding pair and lone pair attractors with geometry. Since separate (irreducible) bonding domains are not observed for $SnO_2$, silicate systems were chosen as a starting point since localized bonding pairs appear in the ELF along the Si-O bond vector, in addition to the lone pair features banana-shaped feature on the oxide anions. The silicates also offer the advantage of a variety of naturally occurring (mineral) silica polymorphs with well-known bulk crystal structures, much variability in the Si-O-Si bond angle, and different cation and anion coordination numbers. In association with G.V. Gibbs of the VT Geological Sciences Department, a variety of bulk silicate crystal structures and silicate molecules have been examined.

The two mineral $SiO_2$ polymorphs quartz and coesite provide an opportunity to examine 2-coordinate bridging oxide anions within well-defined bulk structures with a range of Si-O-Si bond angles that vary from ~ 137º to 180º (ie, a linear Si-O-Si connection) [66]. In coesite alone, there are five distinct Si-O-Si bond angles. In addition to these crystalline systems, molecular disilicates, $(HO)_3SiOSi(OH)_3$, and a range of molecular cyclosilicates, $(H_2SiO)_n$, with n ranging from 2 to 8 have been examined [66,67]. All structures (crystalline and molecular) were geometry optimized and the ELF and valence charge density examined. For the disilicate molecules, additional runs were made where the Si-O-Si bond angle was varied systematically from 110º-180º and the Si-O bond lengths geometry optimized at each fixed angle [67]. In all, Si-O-Si bond angles from 90.5º to 180º have been examined.

For this set of crystalline and molecular systems, the Si-O bond lengths decrease in a regular fashion as the Si-O-Si bond angle increases. The banana-shaped lone pair ELF localization feature across the apex of the Si-O-Si bond is observed to be irreducible, and the local maximum value of both the ELF and the valence charge density for the lone pair feature on bridging 2-coordinate oxygens decreases nonlinearly with bond angle, in the same regular fashion for all the crystalline and molecular systems that were examined (Figure 21).

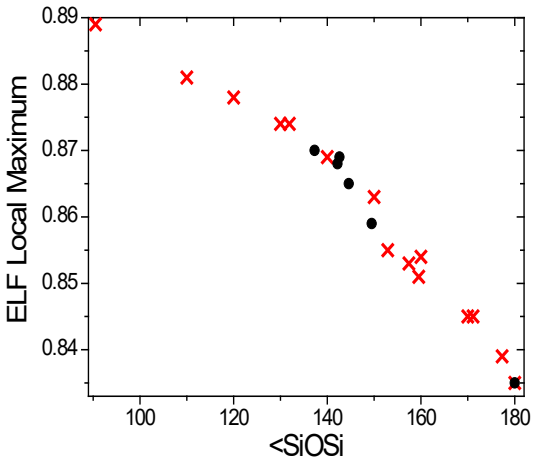


**Figure 21. Variation in the maximum ELF for bridging (2-coordinate) oxygen as a function of Si-O-Si bond angle. Black circles are from crystalline systems. Red crosses are from model molecular systems.**

Viewing the ELF for a fixed percentage (98%) of the maximum lone pair value with widening bond angle (Figure 22) shows that as the local maximum value for the lone pair ELF decreases, the banana shaped isosurface thins and becomes more extended around the anion. In conjunction with these changes in the lone pair feature, the bonding pair isosurfaces along the Si-O bond vector increase in size (Figure 22). At 180º, the two features merge, and the bonding pair isosurface completely envelops the nonbonding isosurface. These changes indicate a migration of electron density from the lone pair region to the bond pair region, consistent with the decrease in bond length with increasing angle, and in agreement with previous calculations demonstrating an increase in the charge density along the Si-O bond vector at the bond critical point [67].

In addition to the variation in bonding and nonbonding (lone pair) properties with angle, comparison with experiment for bulk silicates indicates that the position of the ELF local maximum for the lone pair (locations of expected electrophilic attack in these systems) provides a simple predictive indicator of the bonding sites for protons in bulk coesite and stishovite (a rutile-structured silica polymorph) [66,67]. During the remainder of the current project period, we will determine the minimum energy location of isolated protons in bulk stoichiometric and defective stishovite for comparison to the postion(s) expected from the topology of the ELF in the absence of the proton. After these baseline calculations are completed, we intend to examine the adsorption of hydrogen and dissociation of water on the stishovite (110) surface which is isostructural with $SnO_2$ (110).

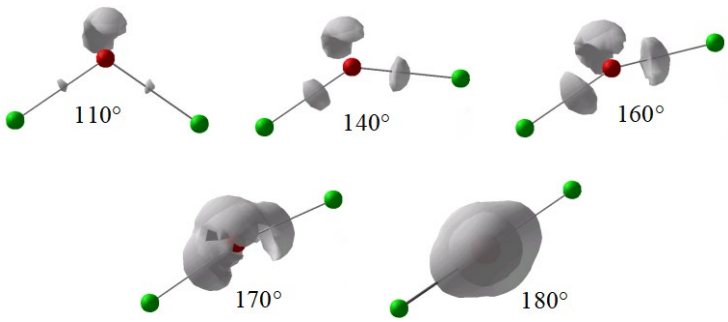


**Figure 22. Variation in bonding pair and lone pair ELF isosurfaces as a funtion of SiOSi bond angle. The ELF was varied between the pictures to maintain the lone pair feature at 98% of the local maximum value.**

Our computational work may appear to have drifted away from our experimental effort, given our current focus on chromia surfaces in the laboratory and bulk silica in the computations. However, we expect our observations of bulk local electronic structure to be useful in interpreting 3-D ELF and charge density distributions at oxide surfaces, and the effects of variations in bond length, bond angle and coordination on the local electronic properties and chemistry of oxide surfaces.

### 2.2.4 Changes in Direction in the Last Project Period.

The original proposal for the current project period included a plan to initiate characterization and reactivity studies on $Cr_2O_3$ (0001) in addition to our work on $Cr_2O_3$ $(10\bar{1}2)$. The original expectation was that the $(10\bar{1}2)$ surface would do no coupling chemistry since the predominant cation sites have but a single coordination vacancy, and it was thought that the (0001) surface, which contains cations with multiple coordination vacancies, would be required for any coupling chemistry to occur. Given that C-C bond formation and coupling chemistry is observed on the $(10\bar{1}2)$ surface, a decision was made to focus the experimental effort primarily on that surface.

## 2.3 Results and Accomplishments 5/1/2003 – 4/30/2006

Our work in this budget period focused on reactions of hydrocarbon fragments (primarily $C_2$ species) over the stoichiometric $\alpha$-$Cr_2O_3$ $(10\bar{1}2)$ surface. Work from a previous period confirmed that oxygen insertion into (nonoxygenated) $C_1$ hydrocarbon fragments with resulting carbon oxide and water formation occurs in the presence of terminal chromyl oxygen (i.e., on an oxygen terminated surface) but not with the three coordinated surface lattice oxygen available at the stoichiometric surface. Our work in the most recent project period has focused on reactions over the stoichiometric surface where coupling (C-C bond formation reactions) and fragment decomposition reactions are expected based on our previous work with $C_1$ fragments. In the final six months of the last budget period, we completed our investigations of $C_1$ fragment chemistry (specifically, an investigation of methylene migration and insertion), and began our work on the reaction chemistry of $C_2$ fragments. The plan of work with $C_2$ fragments was to examine the reaction pathways and kinetics of a variety of $C_2$ alkyl and alkenyl fragments as a starting point for understanding the origins of reaction selectivity and coke formation in the dehydrogenation of ethane over chromia surfaces.

### 2.3.1 Methylene Migration and Insertion Reactions on $\alpha$-$Cr_2O_3$ $(10\bar{1}2)$.

The reactions of iodomethane, $CH_3I$ (and $CD_3I$), and di-iodomethane, $CH_2I_2$, were studied in an earlier project period for insight into the reaction chemistry of methyl and methylene fragments, respectively, on $Cr_2O_3$ surfaces. During the most recent project period, C 1s and I 3d photoemission measurements have shown that some C-I bond cleavage occurs upon adsorption at 120 K on $\alpha$-$Cr_2O_3$ $(10\bar{1}2)$, and is complete by 200 K for $CH_3I$ and by 250 K for $CH_2I_2$. C 1s binding energies for the remaining fragments (283.5 eV for $CH_2$ and 283.7 eV for $CH_3$) are similar to those seen on metals [64, 65], and confirm our earlier suggestions that the methylene and methyl fragments are bound at cation sites. For $CH_2I_2$, there is no clear indication of sequential C-I bond breaking from the photoemission measurements. The halogen adatoms deposited by halocarbon dissociation cap the single coordination vacancies on the surface cations, and eventually shut down the surface chemistry via site blocking after sufficient exposure and reaction [66-68]. Dehydrogenation and hydrogenation are observed for both starting reactants, and methylene coupling to ethene is observed for the reaction of $CH_2I_2$ but no methyl fragment coupling to ethane is observed for the reaction of $CH_3I$. Ethene and $H_2$ are also produced from surface methyl fragments (i.e. from $CH_3I$), with a rate limiting step of methyl fragment dehydrogenation. *In addition, complete dehydrogenation and surface carbon deposition is observed from both $CH_2$ and $CH_3$ fragments.* At the end of the last budget period, the remaining work was to determine the viability of methylene insertion into the Cr-$CH_3$ bond as a route to ethene via subsequent β-hydride elimination.

The possibility of methylene insertion was tested by the reaction of coadsorbed $CH_2$ and $CD_3$ fragments (from $CH_2I_2$ and $CD_3I$, respectively) following the approach of Bent and coworkers [69] to look for a $CH_2$=$CD_2$ product. Three forms of ethene are observed in thermal desorption, as shown in Figure 23, for coadsorbed $CH_2$ and $CD_3$. The $CH_2$=$CH_2$ and $CD_2$=$CD_2$ traces are identical to those for ethene formed from the individual fragments $CH_2$ (from $CH_2I_2$) and $CD_3$ (from $CD_3I$), respectively. The $CH_2$=$CD_2$ product is formed by methylene insertion into a methyl fragment to form a surface ethyl fragment, followed by β-hydride elimination from ethyl to form ethene. $CH_2$=$CD_2$ production occurs in a temperature range where direct methylene coupling (to $CH_2$=$CH_2$) is seen, but at a temperature about 50 K higher than that observed for ethyl fragment dehydrogenation (from $CH_3CH_2X$ as discussed below) to ethene indicating that the rate limiting step is likely methylene migration. Hence, operable pathways observed for C-C bond formation in the $C_1$ reaction system include direct methylene coupling ($CH_2 + CH_2 \rightarrow CH_2$=$CH_2$) and methylene insertion into a methyl fragment with subsequent β-hydride elimination ($CH_2 + CH_3 \rightarrow CH_2CH_3 \rightarrow CH_2$=$CH_{2(g)} + H_{(ads)}$).

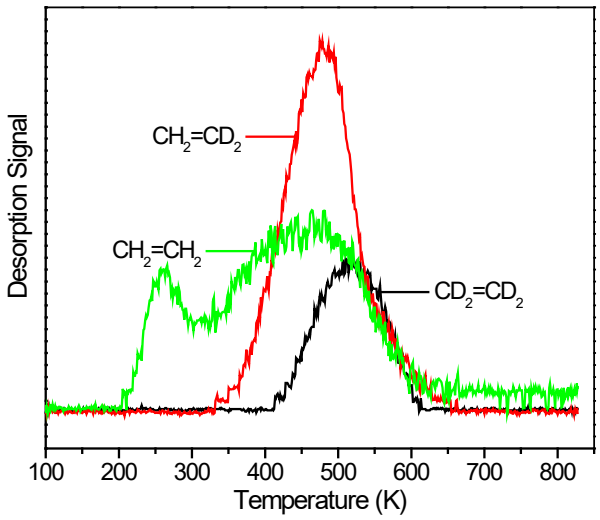


**Figure 23. Thermal desorption following $CH_2I_2$ and $CD_3I$ coadsorption on stoichiometric, α-$Cr_2O_3$ ($10\bar{1}2$).**

The observed coupling reactions to ethene are unexpected. Site requirements for coupling reactions on oxides surfaces are generally thought to require multiple coordination vacancies on a single cation to bind the ligands involved in the coupling reaction [3], or require ligands on closely-spaced neighboring cation sites. The separation between cation sites on the nearly stoichiometric surface is greater than 3.5 Å, a farther distance than one would expect to allow coupling between adjacent sites without some mobility of the surface species. We see no indication in thermal desorption for gas phase radicals (i.e., no unaccounted for m/z 15 signals that might indicate $CH_3$ radical desorption) or carbenes (unaccounted for m/z 14 signals), indicating that the coupling products originate from surface reactions. Note that ethene is a major product of the reaction of methyl fragments, not just a trace product that could be easily explained by reactions at minority surface sites such as steps or under-coordinated cations associated with surface oxygen vacancies. The coupling mechanism is not fully understood. In the section on new work (below), we propose using first principles calculations to examine activated processes such as methylene migration and insertion.

### 2.3.2 Synchrotron Work From the Past Budget Period.

During the previous two years of the project we started a new effort in synchrotron-based characterization of reaction systems. Our goal was to use near-edge x-ray absorption fine structure (NEXAFS) and synchrotron-based photoemission to provide a positive identification of $C_2$ hydrocarbon fragments and their geometry on $\alpha$-$Cr_2O_3$ $(10\bar{1}2)$, particularly for alkenyl fragments. We have made use of the U12a beam line at the National Synchrotron Light Source (NSLS), initially with the help of David Mullins of Oak Ridge National Laboratories, the beam line spokesperson and PRT member. We have made four trips to the NSLS, and used beam time supplied by the General Users Program and supplemented with time donated by the PRT. Table 1 lists the adsorbates examined on stoichiometric $\alpha$-$Cr_2O_3$ $(10\bar{1}2)$ at U12a, and the type of experiments performed. Some photoemission work was done on the adsorption and dissociation of $CH_2I_2$ and $CH_3I$, in addition to our work on $C_2$ chemistry. The photoemission experiments have proven immediately useful because of the improved resolution (even with the required charge compensation by electron flood gun) and signal-to-noise. The NEXAFS experiments have been more problematic. The facilities at U12a had not been used extensively for NEXAFS measurements, so a number of modifications have been made by the PRT to enhance the facilities. During the course of our experiments, the design and collection geometry of the electron partial yield detector (PYD) has been modified, additional shielding has been added to the detector, and the signal collection circuitry has been upgraded. While the facilities have improved, we have also faced some difficulties related to our chromia substrate, as described below.

Table 1. Adsorbates studied to date on stoichiometric $\alpha$-$Cr_2O_3$ $(10\bar{1}2)$

| Adsorbate | XPS | NEXAFS |
|---|---|---|
| HC≡CH | × | × |
| $CH_2$=$CH_2$ | × | × |
| $CH_2$=CHCl | × | × |
| $CH_2$=$CCl_2$ | × | × |
| cis-CHCl=CHCl | × | × |
| trans-CHCl=CHCl | × | × |
| $CH_2$=CFCl | × | × |
| $CH_2I_2$ | × | |
| $CH_3I$ | × | |
| $CH_3CH_2I$ | × | |
| $CH_3CH_2Cl$ | × | |

Figure 24 shows example NEXAFS spectra for mono and dichlorinated ethene molecules at monolayer or greater coverages for grazing incidence light (70° off the surface normal). The spectra are similar to those reported by Bent and coworkers [70] for chlorethenes on Cu(100). The spectra show sharp C 1s→π* resonances at different energies associated with carbon atoms with different extents of chlorination: hυ = 284.5 eV for $=CH_2$, 285.9 eV for =CHCl, and 287.1 eV for $=CCl_2$. Comparison to XPS measurements shows that the variations in energies of the π* resonances are primarily associated with the different C 1s initial state energies [70]. While the C 1s → π* resonances are clear and distinctive, problems associated with the study of $Cr_2O_3$ have prevented a reasonable analysis of features for photon energies in the range from about 288 to 296 eV (highlighted in Figure 24). The binding energy for Cr 2p core levels is almost identically twice that of C 1s. As a result, second order light from the monochrometer excites Cr 2p resonances as demonstrated in Figure 25. Both spectra in Figure 25 are for normal incidence light and a monolayer coverage of vinyl chloride ($CH_2$=CHCl), but in one case the high pass filter on the PYD has been set -150 V to accept C 1s and Cr 2p features, and in the second case set higher than the range of primary photon energies examined to accept only signals associate with Cr 2p excitations from second order light. Because of the high concentration of Cr in the sample, the signal from the small fraction of second order light is much larger than the C 1s NEXAFS. In principle, these contributions can be removed by ratio (or subtraction) with a background spectrum, but in practice we have found that the details of the resulting spectrum in the range of photon energies from 288-296 eV are strongly dependent on small details of the alignment and relative intensities of the spectra. Hence, while the sharp C 1s → π* transitions can be readily observed and used to provide an indication of the presence of a π system in the adsorbate, most of information from the σ* transitions is lost. Note that the overlap of the Cr 2p resonances with the carbon π* resonances is minimized because we are working with chomia ($Cr^{3+}$) rather than chromium metal. This overlap of signal from the second order light limits the usefulness of NEXAFS in the available experimental set up to adsorbates on $Cr_2O_3$ with π systems.

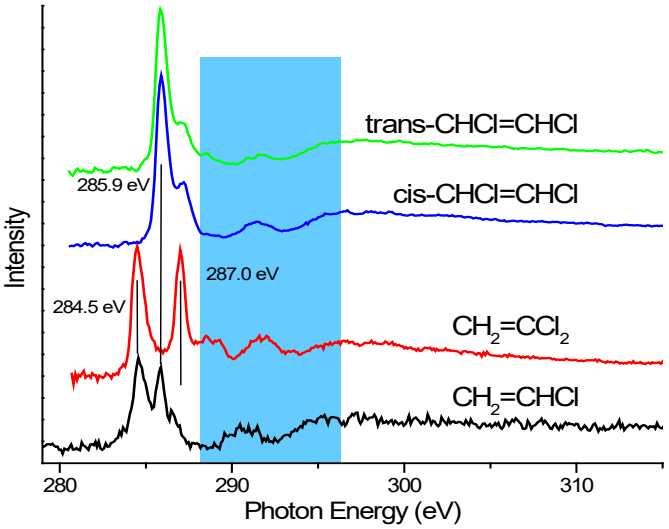


**Figure 24. NEXAFS spectra for molecular chlorethenes on stoichiometric α-$Cr_2O_3$ ($10\bar{1}2$). See text and Figure 4 for a description of the highlighted region.**

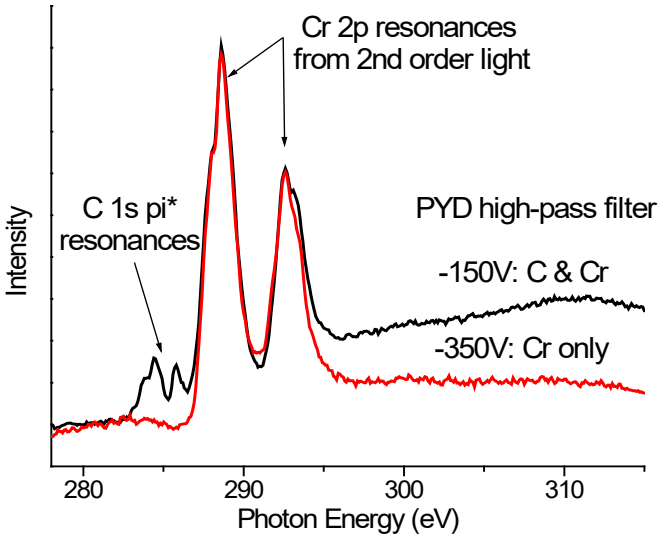


**Figure 25. NEXAFS spectra showing the large contribution spectral contribution associated with Cr 2p resonances from 2nd order light.**

### 2.3.3 Reactions of $C_2$ alkenyl fragments on stoichiometric α-$Cr_2O_3$ (10$\bar{1}$2).

While ethene is the end product of choice in ethane dehydrogenation, subsequent reactions of ethene will influence the overall selectivity, the nature of side products, and may contribute to coke formation and catalyst deactivation. We undertook a study of the reactions of halogenated ethenes as a route to forming different surface intermediates that might result from C-H bond activation in ethene.

**2.3.3.1 $CH_2$=CHCl adsorption and the reaction of vinyl fragments on stoichiometric α-$Cr_2O_3$ (1$\bar{1}$02).** The adsorption and reaction of vinyl chloride ($CH_2$=CHCl) was examined as a route to generating surface vinyl fragments. Photoemission (Figure 26) demonstrates that vinyl chloride dissociates via C-Cl bond breaking on the stoichiometric (10$\bar{1}$2) surface. High binding energy features in the C 1s and Cl 2p spectra are associated

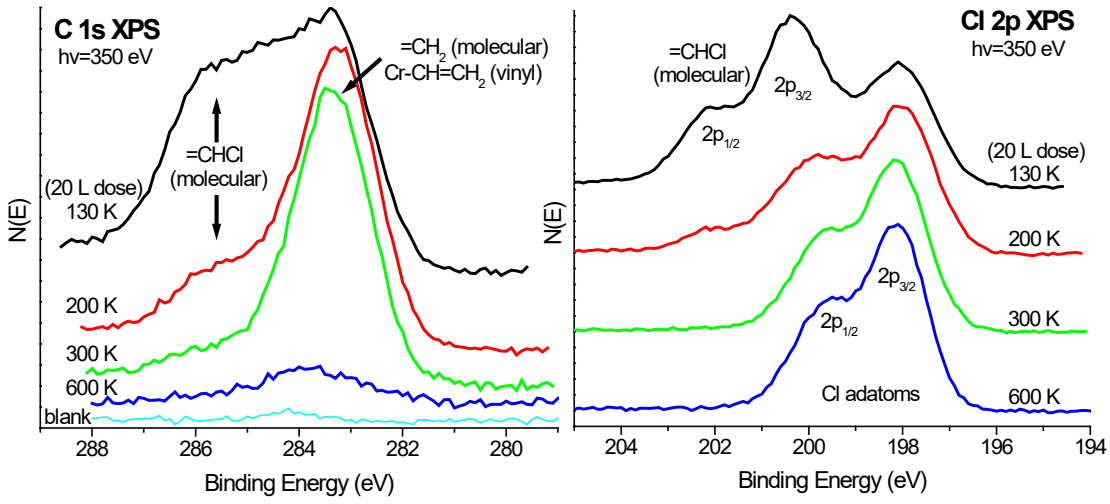


**Figure 26. Synchrotron-based photoemission for adsorbed and annealed $CH_2$=CHCl on stoichiometric α-$Cr_2O_3$ (10$\bar{1}$2) for hυ = 350 eV.**

with intact C-Cl bonds, and therefore molecular vinyl chloride. These high binding energy features decrease in intensity with heating, giving C 1s spectra at 200 K where most C-Cl bonds are broken, and by 300 K the spectrum is characteristic of essentially complete C-Cl bond breaking. The partially resolved Cl 2p doublet shows a similar effect, with spectra characteristic of Cl adatoms after annealing at the higher temperatures. It is clear from the Cl 2p spectrum following the dose that some initial dissociation occurs upon adsorption at the 130 K dosing temperature.

NEXAFS spectra (Figure 27) give another clear indication of these chemical differences, and provide orientation information about the species in the mixed monolayer following adsorption

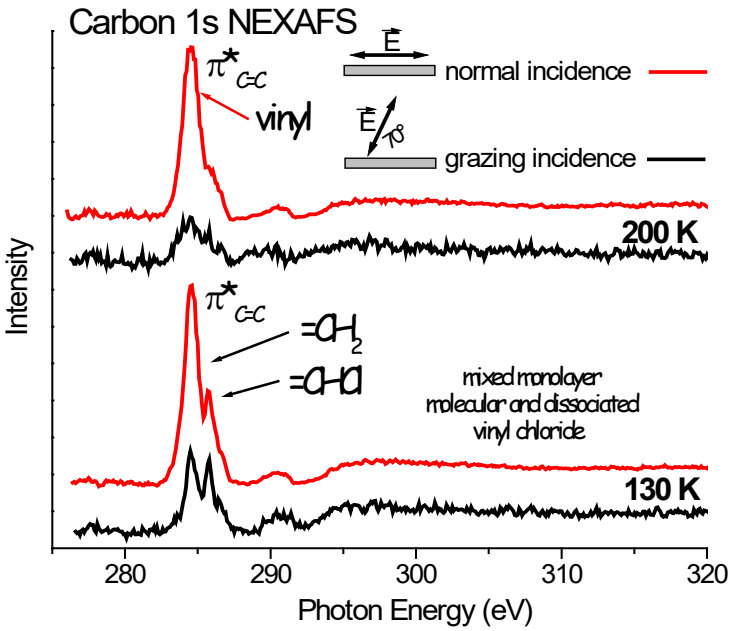


**Figure 27. C 1s NEXAFS spectra for adsorbed and annealed $CH_2$=CHCl on stoichiometric α-$Cr_2O_3$ (10$\bar{1}$2).**

and annealing. Following adsorption at 130 K, two sharp C 1s → π* resonances are seen at 284.5 and 285.7 eV. The π* feature at higher photon energies is associated with the chlorinated carbon, consistent with the higher binding energy C 1s feature seen in photoemission [70]. In the mixed monolayer following adsorption at 130 K, spectra most characteristic of molecular vinyl chloride (i.e., two π* resonances of nearly equal intensity) are seen for grazing incidence light, while the dominant contribution for normal incidence is the π* resonance for non-chlorinated carbon [70]. These data suggest a molecular species bound nominally parallel to the surface since the π* resonances should be largest for a polarization vector perpendicular to the molecular plane [71]. After heating to 200 K, photoemission indicates that most of the C-Cl bonds are broken, and the π* resonances in NEXAFS indicate an intact π system characteristic of non chlorinated carbon that serves as a fingerprint for surface vinyl groups [72]. The polarization dependence of the NEXAFS spectra at 200 K indicates the vinyl groups are orientated with the molecular plane perpendicular to the surface. These preferred orientations for the molecular vinyl chloride and vinyl fragments match our predicted geometries from DFT calculations shown in Figure 28.

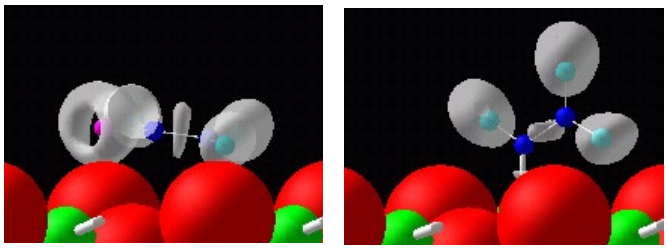

**Figure 28. Adsorption geometries predicted with DFT for molecular vinyl chloride (left) and a vinyl fragment (right) on stoichiometric α-$Cr_2O_3$ (10 $\bar{1}$ 2). Isosurfaces of the electron localization function (ELF = 0.73) are displayed for the molecule and fragment. The cylindrical feature between the two (blue) carbon atoms shows a topology characteristic of the molecular π system. The molecular species is π-bonded to a (hidden) surface $Cr^{3+}$ cation with the molecular plane nominally parallel to the surface, and the vinyl fragment is σ-bonded to a (hidden) surface $Cr^{3+}$ cation with the molecular plane perpendicular to the surface. Cr (green) cations and O (red) anions are drawn with their approximate ionic radii, while the adsorbate atoms are drawn to arbitrary size for ease of viewing.**

Thermal desorption experiments (Figure 29) with vinyl groups generated from vinyl chloride gives Cl adatoms as a surface reaction product along with four gas-phase reaction products: acetylene (HC≡CH), ethene ($CH_2$=$CH_2$), 1,3-butadiene ($CH_2$=CH–CH=$CH_2$), and dihydrogen. No water or chlorinated gas-phase products are formed. Separate thermal desorption experiments with dosed acetylene, ethene, butadiene and atomic hydrogen (split with a hot Pt filament) give no reaction products (except H recombination to $H_2$), and desorption of the molecular species all occur below 400 K (i.e. at temperatures significantly lower than those observed from the reaction of vinyl chloride), indicating that the chemistry from vinyl chloride is all surface reaction limited. The chemistry is described by the following simple reaction sequence:

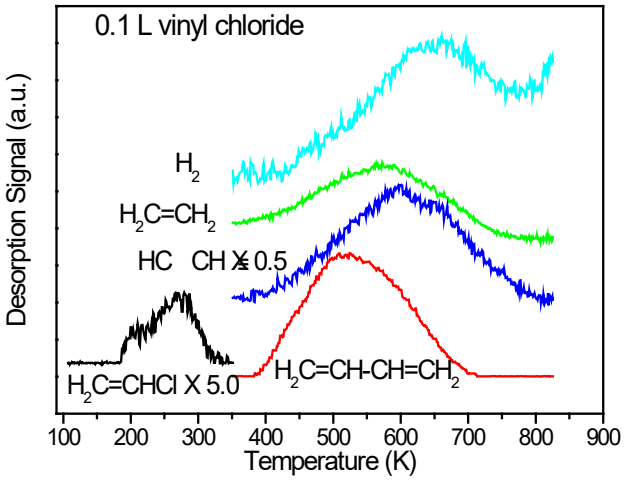


**Figure 29. Thermal desorption for a 0.1 L dose of vinyl chloride on stoichiometric α-$Cr_2O_3$ (10 $\bar{1}$ 2).**

$$2\ CH_2{=}CH{-}_{(ads)} \rightarrow CH_2{=}CH{-}CH{=}CH_2 \quad (1)$$
$$CH_2{=}CH{-}_{(ads)} \rightarrow CH{\equiv}CH + H_{(ads)} \quad (2)$$
$$CH_2{=}CH{-}_{(ads)} + H_{(ads)} \rightarrow CH_2{=}CH_2 \quad (3)$$
$$H_{(ads)} + H_{(ads)} \rightarrow H_2 \quad (4)$$

The vinyl group reaction chemistry is impacted by the surface Cl left from the vinyl chloride reactant. The product distribution changes (Figure 30) with successive small (0.1 L) doses of vinyl chloride as a result of the buildup of Cl adatoms that block cation sites and shut down the surface chemistry. Post reaction AES analysis following the dosing sequence in Figure 30 shows deposited Cl, but no deposited carbon is observed

indicating that vinyl groups are not a major intermediate for the production of coke. Additionally, the temperature for vinyl dehydrogenation (acetylene production) increases by over 50 K for successive 0.1 L doses (not shown), indicating that vinyl fragments are stabilized by Cl adatom modifiers. For successive 0.1 L doses, the yield of the coupling product 1,3-butadiene goes through a maximum for a pre-dose Cl coverage of about 2/3 ML, where one ML (as measured by AES, see Ref. [66, 68] for details) is defined as one Cl adatom per coordinately unsaturated surface $Cr^{3+}$ cation. Since the primary reaction sites are isolated cations with a single coordination vacancy, the coupling process is thought to involve vinyl migration (surface diffusion) and coupling. The results suggest that butadiene production (vinyl coupling) increases initially due to the stabilization of surface vinyl groups by chlorine, but rolls over at higher halogen coverages because (presumably) the deposited halogen impacts the mobility of vinyl groups by cation site blocking.

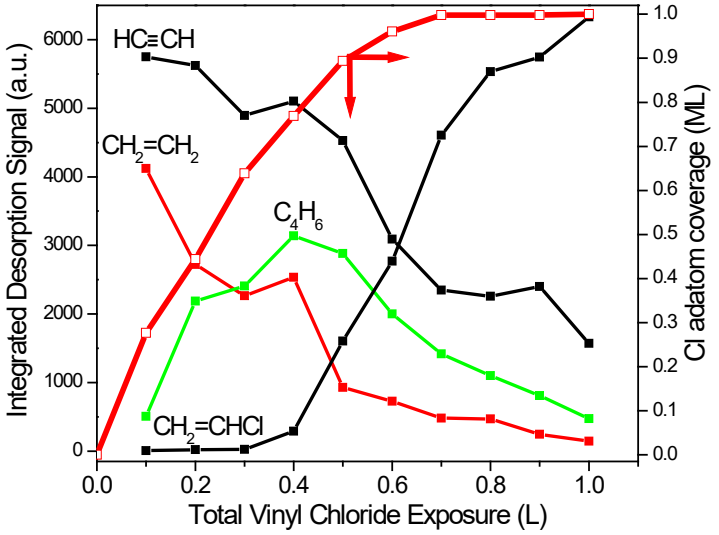


**Figure 30. Variation in relative hydrocarbon desorption amounts for consecutive 0.1 L doses of vinyl chloride on stoichiometric α-$Cr_2O_3$ (10$\bar{1}$2).**

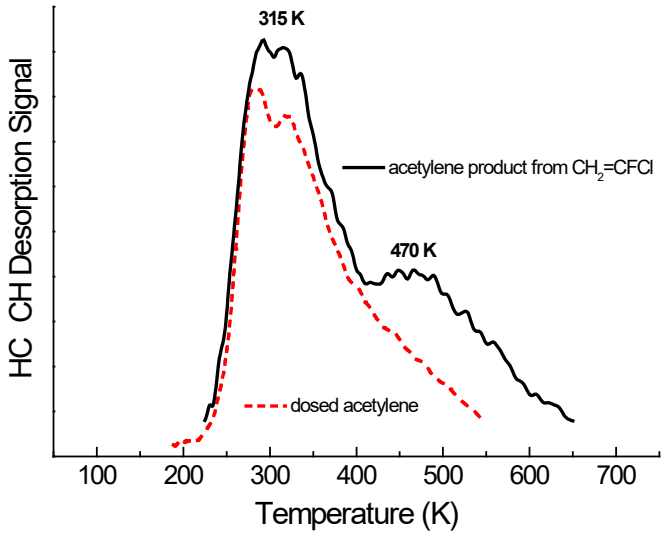


**Figure 31. Acetylene product from $CH_2$=CFCl thermal desorption following a 0.1 L dose on stoichiometric α-$Cr_2O_3$ (10$\bar{1}$2). The dashed line shows the desorption limited evolution of acetylene from the simple adsorption and desorption of acetylene.L doses of vinyl chloride. Similar results are obtained for $CH_2$=$CCl_2$.**

**2.3.3.2 $CH_2$=$CCl_2$ and $CH_2$=CFCl adsorption and the reaction of vinylidene fragments on stoichiometric α-$Cr_2O_3$ (10$\bar{1}$2).** The adsorption and reaction of 1,1-dihaloethenes were examined as precursors to surface vinylidene fragments. We have reported on the reaction of 1-chloro-1-fluoroethene, $CH_2$=CFCl [66, 67] , where acetylene is the only gas phase reaction product observed in thermal desorption (Figure 31), and is produced by both a desorption limited (315 K) and a reaction limited (470 K) channel. Surface halogen adatoms are the only surface products found in post-reaction AES analysis under the conditions of our thermal desorption

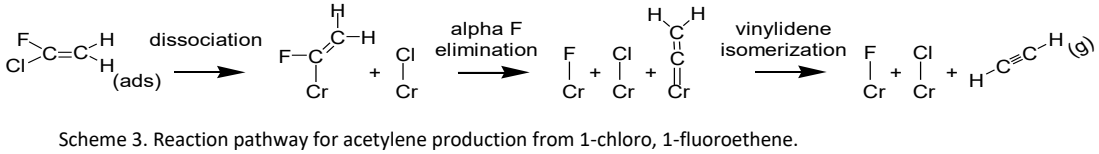


Scheme 3. Reaction pathway for acetylene production from 1-chloro, 1-fluoroethene.

experiments; no carbon deposition is observed. Based on the differences in C-Cl and C-F bond strengths, the reaction was proposed to involve initial C-Cl bond cleavage to form an α-fluorovinyl intermediate, α-fluorine elimination to vinylidene, and vinylidene isomerization to acetylene (Scheme 3) [66, 67]. We note that on metals vinylidene has been generally reported to decompose to hydrogen gas and surface carbon [33, 36-

38]. Hence, the selectivity for the reaction of the proposed vinylidene intermediate is remarkably different on stoichiometric α-$Cr_2O_3$(10$\bar{1}$2), presumably due to the limited capacity for backbonding of isolated the $Cr^{3+}$ cations [66, 67].

Halogen deposition was also found to "activate" the reaction, causing an increase in the production of desorption limited acetylene [66, 67] until site blocking of surface cation sites by halogen eventually shuts down the chemistry. In our initial report, no spectroscopic characterization of the surface hydrocarbon species was available, and it was unclear if the rate limiting step for the reaction-limited production of acetylene was α-fluorine elimination or vinylidene isomerization.

The reaction of 1,1-dichlorethene, $CH_2$=$CCl_2$, was examined with the idea of decreasing the activation barrier to α-halogen elimination from the proposed α-halovinyl intermediate by substitution of Cl for F. In thermal desorption experiments, acetylene was again observed to be the only gas phase reaction product, and again, both desorption and reaction limited channels to acetylene are observed. However, the activation barrier for the reaction-limited channel is unchanged, suggesting that the proposed α halo elimination reaction is not rate limiting and implicating vinylidene isomerization as the rate limiting step in the production of reaction limited acetylene. Photoemission and NEXAFS experiments were undertaken with the hope of providing a spectroscopic characterization of the surface intermediates, as well as information concerning the possibility of consecutive C-X bond breaking implied by the proposed reaction mechanism.

Figure 32 shows XPS data (hu = 350 eV) obtained following the adsorption of a monolayer of 1,1-dichloroethene on stoichiometric α-$Cr_2O_3$(10$\bar{1}$2) at 140 K. The Cl 2p photoemission shows evidence for some C-Cl bond breaking (a low binding energy contribution associated with Cl adatoms) upon adsorption at 140 K, while the C 1s and Cl 2p both show clear evidence for the presence of molecular $CH_2$=$CCl_2$ by the high

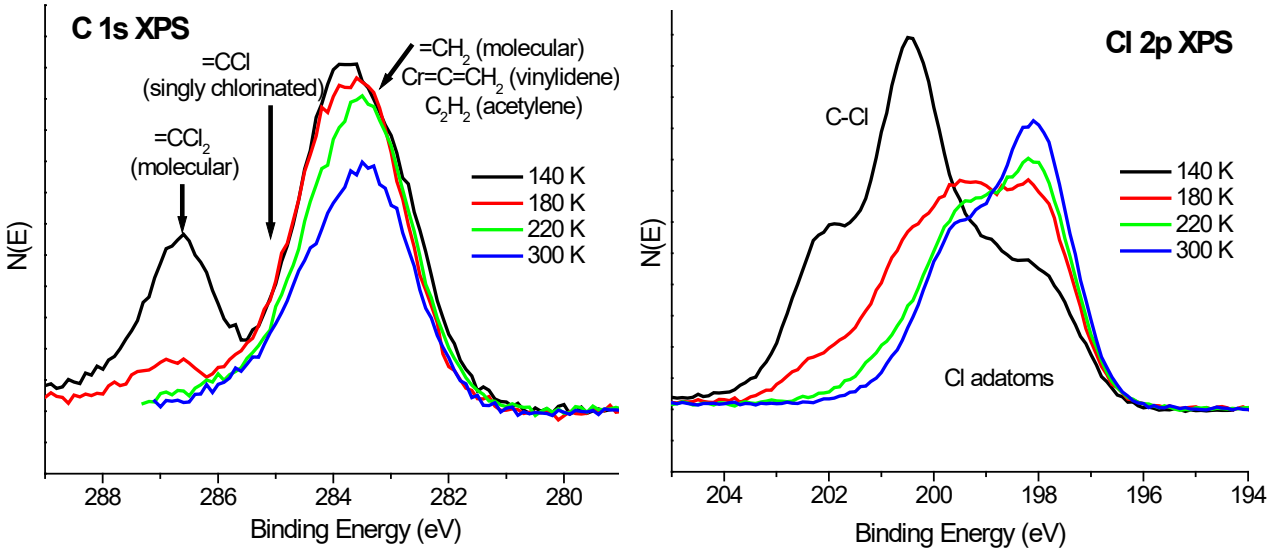


**Figure 32. Synchrotron-based photoemission for adsorbed and annealed $CH_2$=$CCl_2$ on stoichiometric α-$Cr_2O_3$ (10$\bar{1}$2) for hυ = 350 eV.**

binding energy contributions for both core levels associated with intact C-Cl bonds. The results indicate a mixed monolayer of molecular and dissociated species upon adsorption. Following annealing to 220 K, the majority of C-Cl bonds are broken leaving carbonaceous surface species which eventually produce acetylene in thermal desorption. The expected C 1s binding energies for singly chlorinated carbon is known from photoemission data for 1,2-dichloroethenes (below), but there is no clear indication in Figure 32 of sequential C-Cl bond breaking in 1,1-dichloroethene. NEXAFS spectra taken following C-Cl bond breaking at 220 K indicate an intact π system for the surface species, but the spectrum is nearly indistinguishable from that of adsorbed acetylene. Given that significantly more desorption limited acetylene is produced when the surface is activated by Cl adatoms [66, 67], the initial monolayer dose gives rise to significantly more

desorption limited acetylene in thermal desorption. NEXAFS measurements for small initial coverages where the fraction of reaction limited product is greater give too poor a signal to noise to interpret adequately. Hence, while the observed π* resonance in NEXAFS may be consistent with vinylidene species, it can just as easily be assigned to a majority of chemisorb acetylenic species in a mixed monolayer.

For a saturation coverage of 1-chloro-1-fluoroethene ($CH_2$=CFCl) at 120 K, C 1s and Cl 2p photoemission (not shown) indicate that some C-Cl bond breaking occurs upon adsorption, with the majority of C-Cl bonds broken by 200 K. F 1s spectra (Figure 33) show intact C-F bonds following adsorption at 120 K, with contributions of both intact C-F bonds and surface F adatoms following annealing to 200 K. As with the $CH_2$=$CCl_2$ adsorbate, the dehalogenation reactions are quite facile, althought the observation of intact C-F bonds at 200 K (where most C-Cl bonds are broken) indicates that approximately 50% of the fluorine is bound to C in a fluoro-vinyl group at 200K. By 300 K, all C-F bonds are broken, indicating that the surface intermediate for the reaction limited production of acetylene at higher temperatures is vinylidene. Hence, while the substitution of a F atom for Cl can increase the barrier to the second C-X bond breaking event (α halogen elimination), the high temperature reaction limited channel still proceeds through the halogen-free intermediate vinylidene.

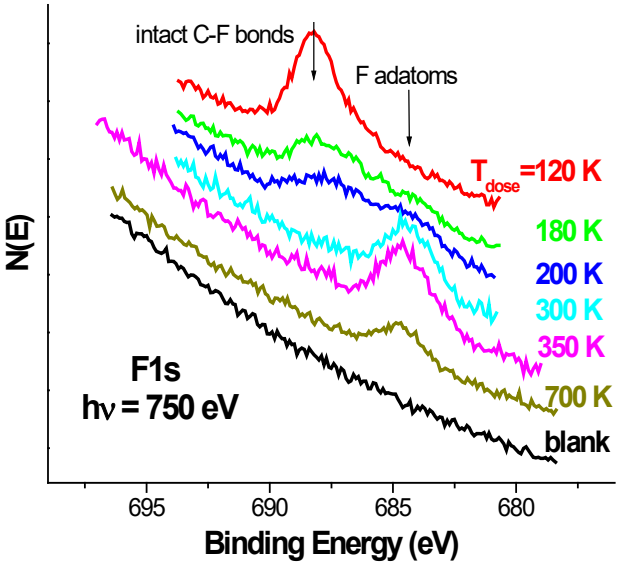


**Figure 33. Synchrotron-based photoemission for adsorbed and annealed $CH_2$=CFCl on stoichiometric α-$Cr_2O_3$ (10$\bar{1}$2) for hυ = 750 eV.**

For the case of $CH_2$=CFCl where there is evidence for some sequential C-X bond breaking, the presence of the F in the α-fluorovinyl fragment lowers the barrier to α elimination in comparison to an unhalogenated vinyl fragment. The result is a reaction path to acetylene (through vinylidene) at a lower temperature than those associated with vinyl coupling to butadiene. Similarly, while migration and coupling to ethene is observed for the $C_1$ carbene methylene, no coupling reactions are observed for the $C_2$ carbene vinylidene which instead isomerizes to acetylene in a temperature range similar to that seen from methylene migration. As observed with vinyl species from vinyl chloride, the reactions of vinylidene surface intermediates from $CH_2$=CFCl and $CH_2$=$CCl_2$ *produce no surface carbon* observable by post reaction AES under the conditions of our thermal desorption experiments. Hence, it appears that vinylidene is not a major intermediate in the production of coke.

**2.3.3.3 cis- and trans-CHCl=CHCl adsorption and the reaction of β-chlorovinyl fragments on stoichiometric α-$Cr_2O_3$ (10$\bar{1}$2).** Our original expectations for the adsorption and reaction of the 1,2-dichloroethenes were that an initial dechlorination step would yield a 2-chlorovinyl surface intermediate with a barrier to β-chlorine elimination lower than that for β-H elimination in an unhalogenated vinyl group. Both the cis and trans isomers of 1,2-dichloroethene were investigated to check for any stereochemical constraints in the surface chemistry.

The reaction chemistry is similar for the two isomers. As with 1,1-dichloroethene, acetylene and surface halogen ($Cl_{(ads)}$) are the only products formed in thermal desorption. Acetylene is produced in both a desorption limited and a reaction limited channel (Figure 34). The reaction limited channel appears at 390 K in thermal desorption, significantly lower than the 550-600 K temperature for vinyl dehydrogenation and the 470 K temperature for vinylidene isomerization. As was seen with the reaction of vinylidene, halogen deposition activates the reaction, causing an increase in the amount of desorption limited acetylene (not shown) until site blocking of surface cation sites by halogen eventually shuts down the chemistry.

Figure 35 shows the C 1s XPS data for trans-1,2-dichloroethene following a multilayer dose and annealing to successively higher temperatures. The photoemission data is characteristic of what is seen for both isomers. Removal of the multilayer leaves a low binding energy feature at 283.3 eV characteristic of a nonchlorinated carbon, and a higher binding energy feature near 285 eV characteristic of a singly chlorinated carbon. The persistence of both features at 360 K where most desorption limited acetylene is removed suggests the expected β-chlorovinyl intermediate for the reaction limited channel to acetylene. As a result of the lower barrier to β elimination at 390 K, the coupling reaction to butadiene observed above 400 K for surface vinyl fragments is suppressed because the barrier to β chlorine elimination is lower than the barrier to vinyl migration. As with the other alkenyl intermediates studied, *no surface carbon is deposited* as a result of the decomposition of this β-chlorovinyl species.

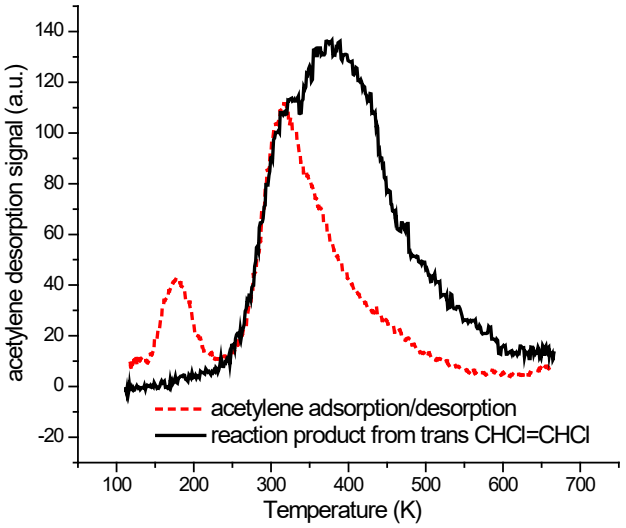


**Figure 34. Acetylene product from trans CHCl=CHCl thermal desorption following a 0.05 L dose on stoichiometric α-$Cr_2O_3$ (10$\bar{1}$2). The dashed line shows the desorption limited evolution of acetylene from the simple adsorption and desorption of acetylene.L doses of vinyl chloride. Similar results are obtained for cis CHCl=CHCl**

On a side note, while no clear stereochemical effects were observed for the decomposition of the two isomers in thermal desorption, the recombination of the β-chlorovinyl species with Cl to produce 1,2-dichloroethene in thermal desorption occurs near 300 K from the trans reactant, and near 385 K (i.e., near the temperature range for β-Cl elimination) for the cis reactant. We currently have no explanation for this observation, but suggest that the difference is an indication that we retain stereospecific β-chlorovinyl surface species from the two reactants.

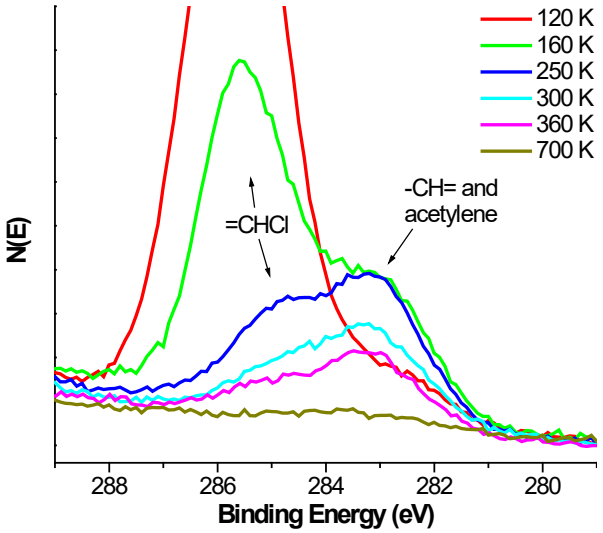


**Figure 35. Synchrotron-based photoemission for adsorbed and annealed trans-CHCl=CHCl on stoichiometric α-$Cr_2O_3$ (10$\bar{1}$2) for hυ = 350 eV.**

**2.3.3.4 Acetylene adsorption on stoichiometric α-$Cr_2O_3$ (10$\bar{1}$2).** Though not an alkenyl species, we have examined the adsorption of acetylene on stoichiometric α-$Cr_2O_3$ (10$\bar{1}$2) because it is the principle thermal desorption product from vinyl fragments, and the only product from vinylidene and β-chlorovinyl fragments. Acetylene adsorbs and desorbs without reaction. No dehydrogenation, coupling, or carbon deposition is observed, and no chlorine containing products are made following acetylene adsorption on a chlorinated surface. Thermal desorption (Figure 36) gives a wide range of desorption temperature for acetylene, with chemisorbed species desorbing between 250 and about 350 K as a function of coverage. For doses greater than about 0.3 L, a low temperature "physisorbed" species desorbs near 135 K. Following adsorption of a saturation coverage at 115 K, annealing to 180 K removes the low temperature "physisorbed" acetylene, and gives an XPS spectrum with a single, slightly broadened (FWHM ≈ 2 eV) C 1s feature at 283.7 eV characteristic of chemisorbed acetylene.

NEXAFS of the chemisorbed layer gives a broadened C 1s → π* resonance with a FWHM (≈ 2.4 eV) about twice that seen for other molecular species. Figure 37 shows the NEXAFS spectrum obtained following annealing to 250 K to leave primarily those adsorbates that give rise to the broad desorption feature between 320 and 400 K. There appears to be two unresolved π* resonances, with a separation that is consistent with both sp (linear) and $sp^2$ (bent) acetylinic adsorbates [73]. There is little dependence of the intensity of the π* transitions with respect to polarization. While no significant polarization dependence is expected for a side-on bonded linear acetylene [73] , the π* resonance associated with a bent ($sp^2$-like) adsorbate is expected to be sensitive to the orientation of the molecular plane with respect to the surface normal. These results were obtained during a visit to the NSLS.

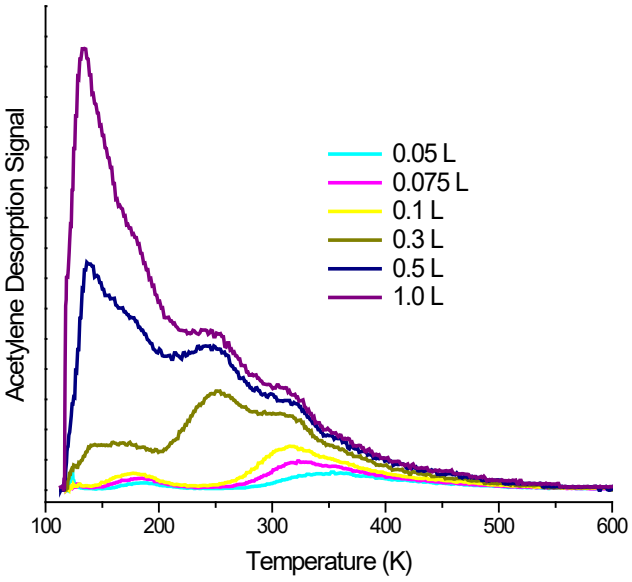


**Figure 36. Thermal desorption of adsorbed acetylene as a function of coverage from stoichiometric α-$Cr_2O_3$ (10 $\bar{1}$ 2).**

Our *preliminary* DFT calculations provide evidence for both bent and linear acetylene adsorption geometries, both with the C-C bond nearly parallel to the surface. Figure 38a illustrates the bent geometry, relative to the coordination octahedron of a surface Cr cation, while Figure 38b shows the tipped geometry of the $sp^2$ plane relative to the surface normal. Tip angles approaching the "magic angle" of 35° will show less polarization dependence than expected for a parallel or perpendicularly oriented plane [71]. The predicted angle near 20° indicates that "tipped" species may reduce the polarization dependence of the spectrum. To date, we have only examined the optimized geometry from two sets of starting conditions. Work is needed to explore the variation in adsorption energy and tip angle with respect to azimuthal orientation to find the lowest energy adsorption states. As noted below in Section 5.4 below, DFT seems to provide reasonable geometries for the (10$\bar{1}$2) surface and adsorbates, but the energetics are still in question. The DFT+U method is being implemented to provide a better electronic description for the highly correlated $Cr_2O_3$ system [74].

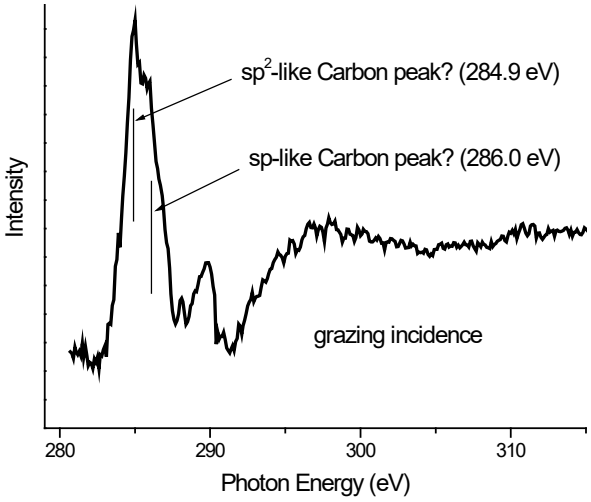


**Figure 37. NEXAFS of adsorbed acetylene after annealing a saturation coverage to 250 K. The spectrum was collected for grazing incidence light (incident angle 70 degrees from the surface normal.**

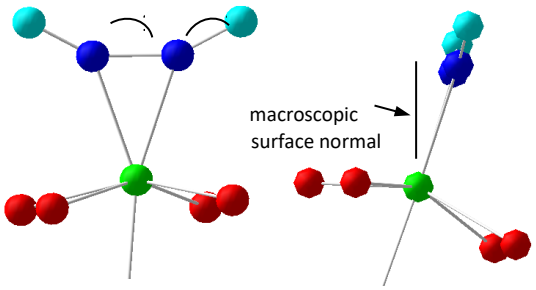


**Figure 38. Predicted "bent" ($sp^2$) geometry for adsorbed acetylene on stoichiometric α-$Cr_2O_3$ (10 $\bar{1}$ 2). (a) shows the side on bonding, while (b) shows the relationship to the macroscopic surface normal.**

## 2.3.4 Reactions of $C_2$ alkyl fragments on stoichiometric α-$Cr_2O_3$ (10$\bar{1}$2).

The simplest alkyl reaction intermediate expected in ethane dehydrogenation is an ethyl fragment from a single C-H bond breaking event. Other $C_2$ alkyl fragments of interest are ethylidene (=CH-$CH_3$) and ethylidyne (≡C-$CH_3$). Less progress was made on this portion of the project due to some personnel problems and associated equipment difficulties. Only the study of the reaction of ethyl fragments has been completed. In the remaining six months of the current project period, we expect to complete thermal desorption studies of ethylidene and ethylidyne precursors and initiate the photoemission studies to finish of this part of the project.

2.3.*4.1 $CH_3CH_2Cl$ and $CH_3CH_2I$ adsorption and the reaction of ethyl fragments on stoichiometric α-$Cr_2O_3$ (10$\bar{1}$2).* The adsorption and reaction of ethyl chloride ($CH_3CH_2Cl$) and ethyl iodide ($CH_3CH_2I$) were examined as a route to surface ethyl fragments. Photoemission demonstrates that the two molecules both dissociate at low temperatures via C-X bond breaking on the stoichiometric (10$\bar{1}$2) surface. Figure 39 shows the characteristic I $3d_{5/2}$ photoemission for the adsorption and reaction of ethyl iodide. C-I bond cleavage begins by 200 K, and the remaining reactant either desorbs or dissociates below 300 K, before the reaction chemistry of the resulting ethyl fragment begins. XPS for ethyl chloride shows a similar trend. The chemistry seen in thermal desorption is illustrated in Figure 40 for the ethyl chloride reactant, but is characteristic of both reactants. The only products are halogen adatoms and three gas-phase reaction products: ethene ($CH_2$=$CH_2$), ethane ($CH_3CH_3$), and dihydrogen. No water, halogenated gas phase products, or coupling products are observed. Separate thermal desorption experiments with dosed ethane, ethene, and atomic hydrogen (split with a hot Pt filament) give no reaction products (except H recombination to $H_2$), and desorption of the

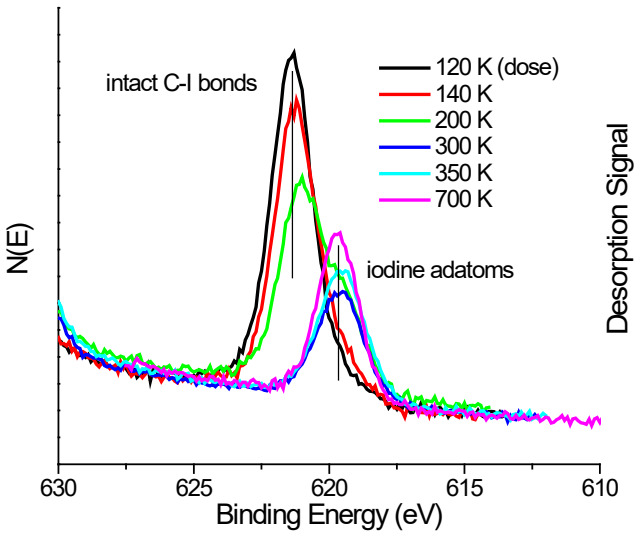


**Figure 39. Synchrotron-based photoemission for a saturation coverage of $CH_3CH_2I$ adsorbed at 120 K and annealed to higher temperatures on stoichiometric α-$Cr_2O_3$ (10$\bar{1}$2). hυ = 700 eV.**

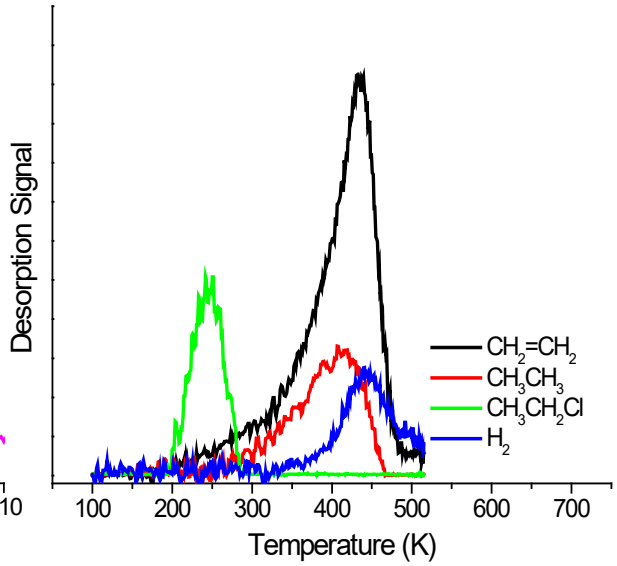


**Figure 40. Thermal desorption for a 0.05 L dose of vinyl chloride on stoichiometric α-$Cr_2O_3$ (10$\bar{1}$2).**

molecular species all occur below 400 K (i.e. at temperatures lower than those observed from the reaction of the ethyl fragment), indicating that the chemistry from the ethyl halides is all surface reaction limited. The chemistry is described by the following simple reaction sequence with a rate limiting β hydrogen elimination step:

$$CH_3CH_2{-}_{(ads)} \rightarrow CH_2{=}CH_2 + H_{(ads)} \quad (1)$$

$$CH_3CH_2{-}_{(ads)} + H_{(ads)} \rightarrow CH_3CH_3 \quad (2)$$

$$H_{(ads)} + H_{(ads)} \rightarrow H_2 \quad (3)$$

The kinetics of the ethyl group reaction chemistry are *not* impacted by the surface halogen left as a

result of the reaction, but the activity decreases with successive doses as a result of the build up of halogen adatoms that block cation sites and shut down the surface chemistry. The yield of all products decreases linearly with the build up of halogen. Post reaction AES and XPS analysis show evidence for deposited halogen, but *no deposited carbon* is observed indicating that ethyl groups are not a major intermediate in the production of coke on this surface.

**2.3.4.2 Experimental work for the remaining 6 months of this budget period: reaction of ethylidene and ethylidyne fragments on stoichiometric α-$Cr_2O_3$ ($10\bar{1}2$).** The reaction of halogenated precursors to ethylidene and ethylidyne will be examined in the remaining six months of the project period. For ethylidene, β hydrogen elimination would give a surface vinyl fragment, while α hydrogen elimination would give ethylidyne (Scheme 2). β hydrogen elimination from ethylidyne should give a vinylidene fragment (Scheme 3). Any hydrogenation of the alkyls associated with the hydrogen provided by H elimination steps leads back towards ethyl fragments and ethane. The chemistry of vinyl and vinylidene species has already been examined, so surface carbon formation from the alkyl fragments is unlikely unless they show a tendency for C-C bond scission on $\alpha$-$Cr_2O_3$ ($10\bar{1}2$). The primary unknown at this point is whether C-C bond formation reactions will be observed.

### 2.3.5 Computational Investigations of $\alpha$-$Cr_2O_3$ ($10\bar{1}2$) surface chemistry.

An exploratory computational investigation of the properties of bulk α-$Cr_2O_3$ and the ($10\bar{1}2$) surface was undertaken to see if DFT methods could provide reasonable predictions of the geometric and electronic structure for this transition metal oxide. There was a concern that calculations involving the transition metal chromium might be problematic since predictions of the correct ground state can be difficult. For this work we use the Vienna Ab-initio Simulation Package (VASP) [54-56, 75, 76], a periodic plane-wave DFT code which can be used for valence electron only calculations using Vanderbilt ultrasoft pseudopotentials [57] or all electron calculations using the projector augmented wave (PAW) method [77]. All calculations have been performed within the local spin density approximation (LSDA) and the generalized gradient approximation (GGA) [78]. It was found that the pseudopotential calculations adequately reproduce the bulk geometric structure, giving bond lengths within better than 1.6% of the experimental values and bond angles within 1.7° of experiment using a C1 point group symmetry. Additionally, the ground state electronic structure was found to match expectations for $Cr^{3+}$ cations based on Hund's rule.

The ($10\bar{1}2$) surface properties were examined using a slab geometry for an 80 atom unit cell 10 atomic layers (two stoichiometric units) thick. The predicted clean surface relaxations are small, with only a slight inward relaxation of the coordinately unsaturated surface cations. Adsorbate geometries have been examined for a number of the adsorbate molecules and hydrocarbon fragments examined experimentally: methyl and methylene fragments, vinyl chloride, vinyl fragments, vinylidene fragments, and recent preliminary examinations of the conformation of adsorbed acetylene. Several of these calculations were made for comparison to (and help in interpretation of) our NEXAFS data. In addition, we have looked at both O and Cl adatoms that bind at surface Cr sites. In our earlier work, terminal chromyl O atoms were found to be active for O-insertion reactions into $C_1$ hydrocarbon fragments and responsible for the formation of carbon oxide reaction products [79]. Cl adatoms are important surface modifiers as seen by their stabilizing influence on surface vinyl fragments and their activating effect on vinylidene fragments where they increase the production of desorption limited acetyelene in TPD. Additionally, we examined the adsorption of $BF_3$, a strong Lewis acid, on 3-coordinate oxygen at the stoichiometric surface, and terminal O atoms. In previous work, we showed experimentally that thermal desorption of $BF_3$ provides a measure of the Lewis basicity of these two different types of surface O atoms [80]. The calculations provide a benchmark on the ability of DFT to reasonably predict molecular binding energies on α-$Cr_2O_3$ ($10\bar{1}2$) surfaces.

While DFT predicts reasonable geometries, the remainders of the bulk electronic properties of $Cr_2O_3$ are not well reproduced. DFT predicts a band gap of ~1.5 eV compared to the experimental value of ~3.4 eV, and while DFT typically under predicts band gaps, it does not handle the strong correlation effects encountered in $Cr_2O_3$ [74], an insulator with properties intermediate between charge transfer and Mott-Hubbard insulators [81]. The difficulties are illustrated by our calculations for $BF_3$ adsorption at terminal chromyl anions and on 3-coordinate surface anions on stoichiometric $\alpha$-$Cr_2O_3$ $(10\bar{1}2)$. The adsorption geometries predicted in both instances are reasonable, with $BF_3$ taking on the non-planar coordination geometry expected for the interaction of this strong Lewis acid with basic oxygen sites [80]. While the predicted heat of adsorption of 17.6 kcal/mol for $BF_3$ at an O atom on the stoichiometric surface is near the 21 kcal/mol experimental value [80], the predictions for the terminal O site are qualitatively incorrect, giving a lower heat of adsorption rather than a higher value observed experimentally.

These issues have been addressed recently by work from the VASP group [74] aimed at predicting surface properties for $Cr_2O_3$ and $Fe_2O_3$, two highly correlated systems. They have implemented a Hubbard-type on-site coulomb repulsion term (the so called DFT+U approach) at the spin-polarized GGA level (GGA+U) [82] and found parameter values that lead to an acceptable compromise between the bulk structural and electronic properties [74]. In application to the $\alpha$-$Cr_2O_3$ (0001) surface, they obtain quantitative agreement with the experimental surface geometry determined with LEED, and are able to predict the stability of the Cr-terminated surface observed experimentally over a wide range of oxygen partial pressures [74]. Their work confirms that the GGA+U provides a correct description of the chromia surface. Interestingly, they find that the biggest discrepancies between the GGA (the method used in our exploratory investigation) and GGA+U occur for O-terminated surfaces, the same situation where our examination of $BF_3$ adsorption failed.

The impact of a single Cl adatom on the properties of neighboring surface atoms has been investigated also. Examination of the variations in atomic charges of nearby surface atoms shows that cations connected the Cl adatom adsorption (cation) site via coordinately unsaturated surface O experience a decrease in valence electronic charge on the order of 25% of that experienced by the Cr cation bonded directly bonded to Cl. Those connected through coordinately saturated O atoms experience no significant change in charge density. While a more electron withdrawing cation site might be expected to increase activation barriers to hydride elimination and decrease barriers to proton elimination [83, 84], it is premature to draw any conclusion about the impact of Cl modifiers on the electronic properties of neighboring cations via a through-surface electronic effect. In light of our earlier difficulties predicting $BF_3$ adsorption energetics, this system will be examined again (below) within the context of the GGA+U method.

### 2.3.6 Computational investigations of bulk minerals and the stishovite, $SiO_2$ (110) surface.

Stishovite is a high pressure, rutile structure-type silica polymorph. We undertook a study of the (110) surface because of a continuing interest in the properties of rutile-structured (110) surfaces that began with our earlier experimental work on the chemistry of $SnO_2$ (110) surfaces [1, 5, 21, 50, 85-88]. Our initial attempts at understanding the stability and chemical properties of $SnO_2$ (110) surfaces with first principles calculations made use of the electron localization function (ELF) [89-92] to highlight properties of the surface electronic structure associated with electron lone pairs on O anions and stereochemical lone pairs on under-coordinated $Sn^{2+}$ cations at oxygen deficient surfaces. The similarity in the topological view of the electronic structure provided by the ELF to that described by the negative of the Laplacian of the electron density used in Bader's AIM [93-99] descriptions led to a collaboration with Prof. G.V. Gibbs (Virginia Tech, Geosciences Department) to examine the topological properties of the ELF for changes in bonding geometry in the well-defined environment of bulk oxide minerals. Silicate systems were chosen as a starting point since separate (irreducible) bond pair domains appear in the ELF along the Si-O bond vector, in addition to those features readily seen in the more ionic $SnO_2$ that are associate with lone pairs.

In a previous budget period, we examined the impact of changes in the SiOSi bond angle on the topology of the ELF and the valence charge density [100, 101]. In the most recent project period, this study was extended to examine the relationship between lone pair features and H atom binding in bulk stishovite [102], variations in ELF topology about oxygen anions with changes in nearest neighbor metal atom electronegativity [103], and the relationship with experimental and predicted electron density distributions and bond critical point properties [104-106]. The experience gained in these studies was used to examine the electronic properties of the stishovite $SiO_2$ (110) surface.

The predicted relaxations for the stoichiometric, stishovite $SiO_2$ (110) surface [107] are small and qualitatively similar to that predicted for $TiO_2$ (110) [108-112], $SnO_2$ (110) [62, 113-116] and $RuO_2$ (110) [117]. The atom-resolved (partial) density of states shows that the surface states at the top of the valence bands are primarily associated with coordinately unsaturated bridging O atoms while those at the bottom of the conduction bands are associated with the coordinately unsaturated Si cations at the stoichiometric surface, as was seen for $SnO_2$ (110) [113, 114].

Visual analysis of the bulk and surface electronic structure using 3D ELF and valence charge density maps gives an intuitively satisfying picture of the electronic structure that matches the "hybridization" descriptions given by Godin and LaFemina for $SnO_2$ [113, 114]. Such descriptions are well know for tetrahedral semiconductors [118], and while they have been applied much less often to oxides, their usefulness in understanding oxide surfaces has also been well established [119-122]. In the bulk, O atoms are coordinated by three coplanar nearest neighbor Si atoms. In their descriptions for $SnO_2$, Godin and LaFemina [113, 114] describe the bulk O atoms as $sp^2$ hybridized with a non bonding lone pair. The topology of the electronic structure described by the ELF for bulk oxygen (Figure 41) clearly shows three bond pairs along the Si-O bond vectors, and a nonbonding lone pair perpendicular to the bonding plane. The arrangement of the four electron pairs intuitively matches the description of Godin and LaFemina [113, 114].

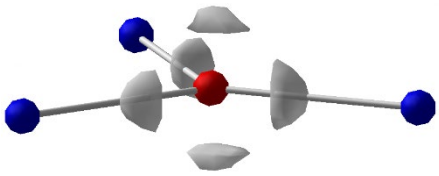

ELF = 0.855

**Figure 41. Bulk O anion of stishovite in planar coordination with three nearest neighbor Si cations.**

At the stoichiometric surface (Figure 42), the ELF describes regions of localization in the electronic structure of outer layer bridging (2-coordinate) oxygen that include two bond pairs along the Si-O bond vectors, and a "banana-shaped" lone pair feature extending across the apex of the Si-O-Si bond [107]. Calculations for (the two coordinate oxygen in) a free water molecule show a similar banana shaped feature associate with the two lone pairs one envisions for the Lewis structure [123] with the four pairs (two bonding and two lone pairs) distributed about the O atom in agreement with the simple VSEPR (valence shell electron pair repulsion) model [124] for molecular structure [107]. The nearly tetrahedral arrangement of the electron pairs suggests an $sp^3$ hybridization for the outer layer bridging oxygens, in agreement with the suggestions of Godin and LaFemina [113, 114].

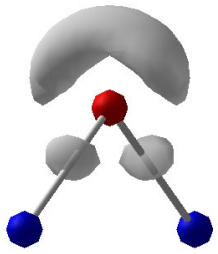

ELF =

**Figure 42. Two coordinate bridging O atom at the relaxed, stoichiometric stishovite $SiO_2$ (110) surface.**

The predominant relaxations observed on the stoichiometric and reduced (110) surfaces are small (0.15 Å) inward relaxations of five-coordinate cations, and small outward relaxations (0.15 Å) of 3-coordinate in-plane anions and the (0.26 Å) six-coordinate cations [107]. The oxygen anion and three nearest neighbor Si cations are all coplanar in the bulk structure, but at the surface the relaxation moves the anion slightly out of plane and away from the surface towards the vacuum. Examination of the spatial distribution of the ELF (Figure 43) shows that a local maximum appears above the apex of the out-of-plane 3-coordinate surface anion rather than the symmetric feature seen in the bulk. The "more tetrahedral" arrangement of the

electron pairs suggests a partial rehybridization from the $sp^2$ condition in the bulk to a more $sp^3$ like state at the surface. Comparisons with the topology of the $H_3O^+$ molecule show a similar single lone pair feature, indicating that the driving force for the out of plane relaxation of the O anions can be understood in terms of the same electron pair repulsion that drives the non-planar geometry of the $H_3O^+$ molecule [107]. Since the coordination number for O anions in bulk oxides tends to range from 2 to 4, these descriptions based on the arrangements of four electron pairs should be applicable to most oxide materials and surfaces. They certainly hold for the coordinately unsaturated (3-coordinate) O atoms at the α-$Cr_2O_3$ (10$\bar{1}$2) surface as shown in Figure 44.

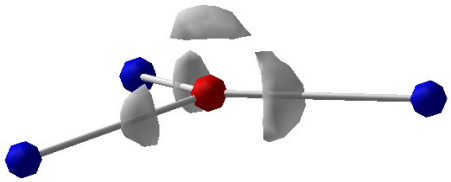

ELF =

**Figure 43. Out of plane relaxation of 3 coordinate in-plane O atom at the relaxed, stoichiometric stishovite $SiO_2$ (110) surface.**

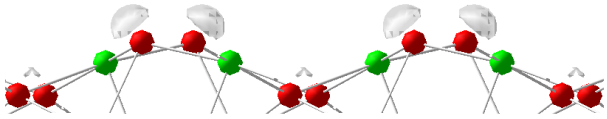

**Figure 44. Well-defined, single lone pair ELF features for three coordinate (red) O atoms at the stoichiometric α-$Cr_2O_3$ (10 $\bar{1}$ 2).**

The surface chemistry of HF on the stishovite $SiO_2$ (110) was examined for several reason. Stishovite exhibits the interesting surface property of being nearly insoluble in HF [125, 126] solutions, a property unique among the silica polymorphs. Additionally, since the adsorption of HF is expected to be dissociative, this adsorbate also provides an opportunity to test the applicability of our observations for bulk silicates that H atoms tend to bind at sites associated with O anion electron lone pairs [102].

HF adsorption was found to be dissociative, with the H and F atoms separating during geometry optimization even for a starting geometry involving molecular HF on stishovite, $SiO_2$ (110). The preferred binding sites for the atomic fragments are at coordinately unsaturated surface atoms: F to the 5-coordinated surface cation, and H to an $sp^3$ hybridized 2-coordinated surface bridging O atom (Figure 45). This is an expected result from simple acid/base considerations for dissociative adsorption of Brønsted acids [3]. The hydrogen atom binds to side of the SiOSi plane defining the bridging O atom, near the location expected for electron lone pairs on the bridging O as seen for H atoms in bulk stishovite [102]. The topology of the ELF for the bound $Si_2OH$ complex (Figure 46) in the full periodic structure takes on a similar geometry to that seen for $H_3O^+$ and for in-plane O atoms following surface relaxation. The complex exhibits four ELF features and the O atom maintains essentially an $sp^3$ hybridization, but at the expense of one lone pair following the addition of the H atom.

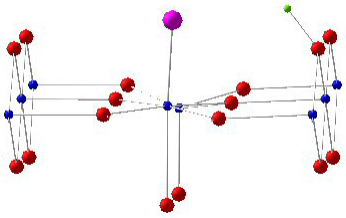

**Figure 45. Binding of dissociatively adsorbed HF on stishovite, $SiO_2$**

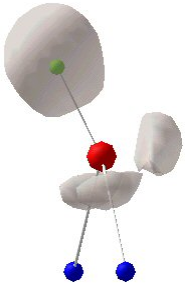

**Figure 46. ELF view of H binding to bridging O on stishovite, $SiO_2$ (110). The O atom retains the sp3 hybridization by forming a nonplanar**

## 2.4 Results and Accomplishments 5/1/2006 – 4/30/2009

During this budget period we pursued four different lines of investigation. (1) We examined the reaction chemistry of ethylidene and ethylidyne on $\alpha$-$Cr_2O_3$ $(10\bar{1}2)$ to complete our examination of $C_1$ and $C_2$ reaction intermediates on this simple surface. (2) We began our studies of the reaction chemistry of hydrocarbon fragments on $\alpha$-$Cr_2O_3$ (0001) to look for any structure sensitivity in these reactions over chromia. (3) We began studies of the reaction chemistry of $C_1$ fragments over $Fe_2O_3$ for comparison to our $Cr_2O_3$ results to directly characterize the impact of a variation in d electron density in the absence of structural effects. (4) We initiated computational studies using DFT of experimentally observed reactions on $\alpha$-$Cr_2O_3$ $(10\bar{1}2)$ that required surface diffusion to drive C-C bond making chemistry.

### 2.4.1 Reactions of C2 alkyl fragments on stoichiometric α-Cr2O3 $(10\bar{1}2)$.

**2.4.1.1 $CH_3CH_2Cl$ and $CH_3CH_2I$ adsorption and the reaction of ethyl fragments on stoichiometric α-$Cr_2O_3$ $(10\bar{1}2)$.** The adsorption and reaction of ethyl chloride ($CH_3CH_2Cl$) and ethyl iodide ($CH_3CH_2I$) were examined as a route to surface ethyl fragments. This work is described in detail in the literature [127]. The only reaction products are halogen adatoms and three gas-phase reaction products: ethene ($CH_2$=$CH_2$), ethane ($CH_3CH_3$), and dihydrogen. No surface carbon deposition (coking) is observed. In thermal desorption, ethene evolves at 500 K from a rate limiting β hydrogen elimination step with an apparent first order activation energy of 31.0 kcal/mol. The simple reaction network can be described by the following steps:

$$CH_3CH_2{-}_{(ads)} \rightarrow CH_2{=}CH_2 + H_{(ads)} \quad (1)$$

$$CH_3CH_2{-}_{(ads)} + H_{(ads)} \rightarrow CH_3CH_3 \quad (2)$$

$$H_{(ads)} + H_{(ads)} \rightarrow H_2 \quad (3)$$

For completeness, and for consideration of the chemistry to be described below, it is noted that for the entire range of alkyl and alkenyl halide reactants and surface intermediates studied to date on $\alpha$-$Cr_2O_3$ $(10\bar{1}2)$, no oxygenated products are ever observed from the nearly stoichiometric surface which exposes only three-coordinated surface lattice oxygen. Only in the presence of terminal chromyl oxygen, Cr=O, on an oxygenated surface are any oxygenated products observed. Additionally, for all the hydrocarbon fragments investigated to date with photoemission ($C_1$ fragments $C_2$ alkenyl fragments and ethyl fragments), the carbon binding energies are consistent with binding at surface Cr cation sites. No evidence is observed for oxygenated surface intermediates.

**2.4.1.2 $CH_3CHCl_2$ adsorption and the reaction of ethylidene fragments on stoichiometric α-$Cr_2O_3$ $(10\bar{1}2)$.** The adsorption and reaction of 1,1-dichloroethane ($CH_3CHCl_2$) was examined as a route to surface ethylidene fragments. No surface carbon deposition is observed from this reaction. AES demonstrates that 1,1-dichloroethane dissociates via C-Cl bond breaking to deposit halogen adatoms, and thermal desorption studies show the generation of reaction-limited ethene as the only gas-phase reaction product (Figure 47). Since deposited halogen adatoms can impact the reaction, we typically use small doses to slow the buildup of halogen and look for variations in the surface chemistry (if any) with varying halogen coverage.

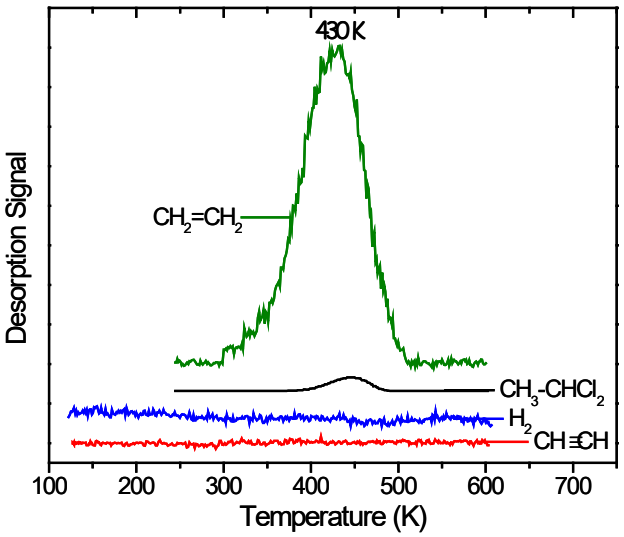


**Figure 47. Thermal desorption following a 0.1 L dose of $CH_3CHCl_2$ on stoichiometric α-$Cr_2O_3$ $(10\underline{1}2)$.**

Unlike the cases of ethyl (above) and ethylidyne (below) decomposition on this surface, no $H_2$ gas is observed as a reaction product from ethylidene, and no hydrogenation (ex., ethane) or dehydrogenation

(ex., acetylene) products are produced. Additionally, no chlorinated products are observed in thermal desorption with the exception of the original dichloroethane reactant molecule. The lone gas phase product is reaction limited ethene which exhibits first order kinetics with an activation barrier to reaction of 27.0 kcal/mol.

Our original expectations were that ethylidene would react via H elimination along one of two possible pathways (Scheme 1). A β-elimination route should produce vinyl fragments and surface H atoms, while an α-elimination route should produce ethylidyne. Our work in the previous project period with vinyl chloride [128] indicates that vinyl groups dehydrogenate to acetylene and hydrogenate to ethene in the presence of surface hydrogen. Likewise, work from the current budget period indicates that ethylidyne (see below) also dehydrogenates to acetylene. The lack of surface $H_2$ and acetylene in the reaction of 1,1-dichloroethane is a clear indication that H-elimination is not an operable pathway. Since the ethene product has the same $C_2H_4$ composition as the expected ethylidene reaction intermediate, it is apparent that the rate limiting step for ethene production is a first-order intramolecular isomerization of ethylidene to ethene (Scheme 2). This reaction is the reverse of the ethene to ethylidene isomerization proposed for Pt(111) enroute to ethylidyne via dehydrogenation [129]. More importantly, the isomerization route for the reaction of this carbene is similar to a pathway we observed in the prior project period on this same surface for another carbene, vinylidene, which isomerizes to acetylene [66, 67]. As with all the hydrocarbon intermediates we have examined to date with photoemission, the ethylidene intermediate is believed to be bound at a surface Cr center.

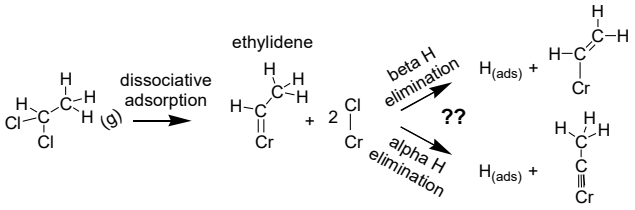


**Scheme 1. Originally-anticipated reaction chemistries from ethylidene dehydrogenation.**

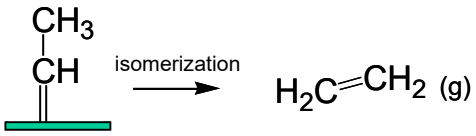


**Scheme 2. Proposed intramolecular isomerization of ethylidene to ethene.**

**2.4.1.3 $CH_3CCl_3$ adsorption and the reaction of ethylidyne fragments on stoichiometric α-$Cr_2O_3$ (10$\bar{1}$2).** The adsorption and reaction of 1,1,1-trichloroethane was examined as a route to surface ethylidyne fragments. AES demonstrates that 1,1-dichloroethane dissociates via C-Cl bond breaking to deposit halogen adatoms, and thermal desorption studies show the generation of three reaction-limited gas-phase products: acetylene (CH≡CH), ethene and $H_2$ (Figure 48). The reaction exhibits first-order kinetics, and an activation barrier to reaction of 39.5 kcal/mol. The 620 K reaction temperature for ethylidyne dehydrogenation to acetylene is the highest we have observed for any alkyl or alkenyl fragments on this surface. *No surface carbon deposition is observed* from this reaction.

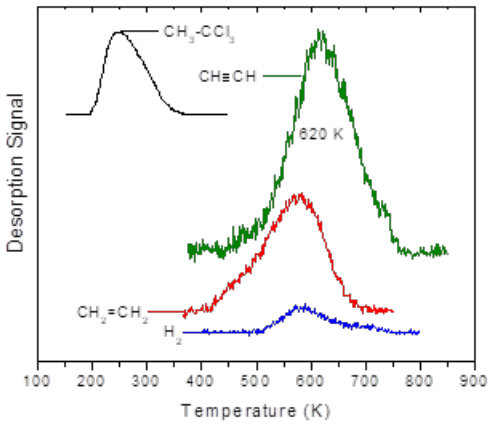


**Figure 48. Thermal desorption following a 0.1 L dose of $CH_3CCl_3$ on stoichiometric, α-$Cr_2O_3$ (10$\bar{1}$2).**

Acetylene production requires dehydrogenation of the ethylidyne reaction intermediate, while hydrogenation must occur for ethene formation. The reaction sequence is readily explained in terms of chemistry we have observed previously from other fragments. The source of H atoms for $H_2$ production and hydrogenation is β-elimination from ethylidyne where the expected products are vinylidene ($CH_2$=C=) and surface H atoms. Work in this budget period has demonstrated that vinylidene isomerizes to acetylene on this surface at lower temperatures than those seen here [29, 67, 68, 128]. Hence, the dehydrogenation route can be described by Scheme 3.

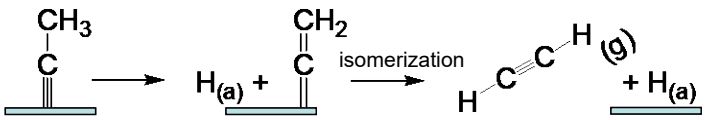


**Scheme 3. Dehydrogenation route from ethylidyne to acetylene on stoichiometric, α-$Cr_2O_3$ (10 $\bar{1}$ 2).**

Ethene production requires hydrogenation of the ethylidyne intermediate by hydrogen released in the dehydrogenation step in Scheme 3. α-H addition to ethylidyne should produce ethylidene, which isomerizes to ethene (section *3.1.2* above) at lower temperatures than those seen here. Hence, the hydrogenation route can be described by Scheme 4. Given the lower reaction temperatures we have observed previous ly for vinylidene isomerization (Scheme 3) and ethylidene isomerization (Scheme 4), the rate limiting step for the reaction sequences is the initial β-H elimination step from ethylidyne.

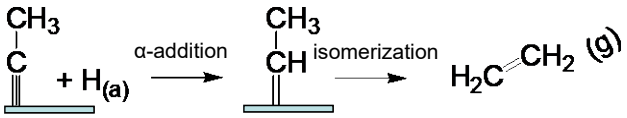


**Scheme 4. Hydrogenation route from ethylidyne to ethene on stoichiometric, α-$Cr_2O_3$ (10 $\bar{1}$ 2).**

## 2.4.2 Summary of $C_1$ and $C_2$ fragment chemistry on stoichiometric α-$Cr_2O_3$ (10$\bar{1}$2).

With the examination of ethylidene and ethylidyne reactions on stoichiometric α-$Cr_2O_3$ (10$\bar{1}$2) in the previous budget period, we completed our reaction studies of $C_1$ and $C_2$ alkyl and alkenyl hydrocarbon intermediates on the (10$\bar{1}$2) surface. The complete list of intermediates studied to date is shown in Figure 49.

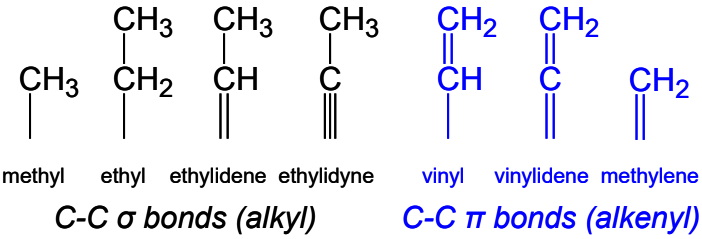


**Figure 49. Complete list of hydrocarbon fragments studied on stoichiometric α-$Cr_2O_3$ (10 $\bar{1}$ 2).**

A number of observations have been made that are relevant to the chemistry of ethane dehydrogenation. Primary among these is that deposition of surface carbon (coke) is only observed in trace amounts from the dehydrogenation of $C_1$ surface intermediates, methyl and methylene fragments, but not from any $C_2$ surface species on stoichiometric α-$Cr_2O_3$ (10$\bar{1}$2) under the conditions of our study. $C_2$ surface intermediates undergo a variety of reactions (hydrogenation, dehydrogenation, isomerization, coupling), but no low-barrier thermal pathways for C–C bond breaking and coke deposition have been found.

The reaction pathways of $C_1$ and $C_2$ intermediates on α-$Cr_2O_3$ (10$\bar{1}$2) are summarized in Figure 50. Hydrogenation pathways have, for the most part, been excluded from Figure 50, with the exception of the hydrogenation reaction connecting ethylidyne ($CH_3$–C≡) to ethylidene ($CH_3$–CH=). Reactions observed for the hydrogenation of methylene and methyl to methane, ethyl to ethane, and vinyl to ethene have been omitted from Figure 50. For all the reactions observed, only those leading to ethene are selective pathways in the ethane dehydrogenation process. All other products (coke, methane, acetylene, 1,3-butadiene), while interesting, are nonselective reaction products with respect to ethane dehydrogenation.

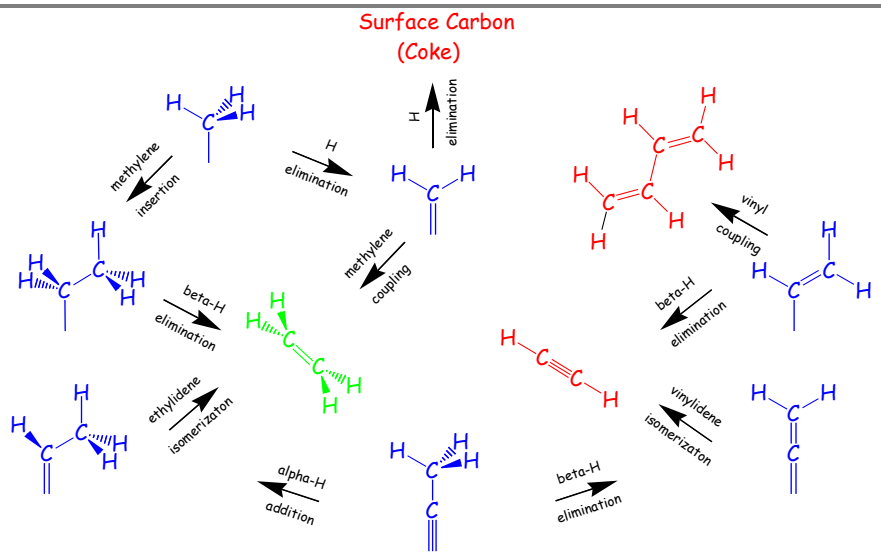


**Figure 50. Summary of the $C_1$ / $C_2$ reaction network on stoichiometric α-$Cr_2O_3$ (10$\bar{1}$2).**

## 2.4.3 Surface characterization and reaction studies on α-$Cr_2O_3$ (0001)

Our interest in reaction studies on α-$Cr_2O_3$ (0001) is to uncover any important structure-sensitive effects in the reaction of hydrocarbon fragments on chromia surfaces. Since the stoichiometric (0001) surface exposes $Cr^{3+}$ cations with three coordination vacancies compared to the single coordination vacancies on the (10$\bar{1}$2) surface, any chemical variations due to coordination differences (local ensemble effects) at surface cation sites which function as the principle reaction sites should be apparent. We are primarily interested in chemical variations that effect reaction selectivity of hydrocarbon fragments on chromia surfaces. This work begins with an initial characterization of the α-$Cr_2O_3$ (0001) surface, and to date we have examined the reaction chemistry of ethyl chloride, 1,1-dichloroethane and 1,1,1-trichloroethane as precursors to surface ethyl, ethylidene and ethylidyne fragments, respectively.

**2.4.3.1 Surface characterization of α-$Cr_2O_3$ (0001).** The experimental work reported in the literature to date on α-$Cr_2O_3$ (0001) has typically been for thin films grown on metallic single crystal Cr substrates, or thin films grown epitaxially on other metal or single crystal corundum-structured (0001) surfaces [130-133]. Our work has been done on a (0001) oriented surface of bulk α-$Cr_2O_3$. This approach has the structural advantage of connecting the surface we examine to a true α-$Cr_2O_3$ single crystal bulk host, but the disadvantage of the sample being insulating.

XPS was used to monitor the composition and chemical state of the surface as a function of ion bombardment, thermal treatments in vacuum and oxygen exposure. As with our earlier work on α-$Cr_2O_3$ (10$\bar{1}$2) [29, 134], the surface composition measured by Mg Kα XPS gives an average value of 1.52 (± 0.05), close to the value of 1.51 estimated for a nonpolar, stoichiometric surface using a layer-by-layer summation.[1] The composition measurements indicate that Cr and O sputter at an essentially stoichiometric rate [29, 134, 135]. At 900 K where the sample is conductive, the Cr $2p_{3/2}$ binding energy falls at 576.9 ± 0.2 eV as expected for $Cr^{3+}$ in $Cr_2O_3$ [136]. The Cr 2p signals for samples prepared by ion bombardment and annealed to 900 K or higher at first appear to show only $Cr^{3+}$ character and give sharp hexagonal (1×1) LEED patterns. However, following oxygen adsorption the photoemission line narrows on the low binding energy side indicative of the oxidation of a lower binding energy contribution (Figure 51). Difference spectroscopy gives a lower binding energy contribution near 574.2 eV characteristic of metallic chromium [136], suggesting that ion bombardment and annealing yields a partially reduced surface. Annealing the oxygenated surface to 1000 K in vacuum causes a partial return of the low binding energy feature.

We tried a number of preparation treatments from the literature that are thought to yield a stoichiometric surface [130-132, 137], but are not yet convinced we have found an ideal treatment for preparing a (nearly) stoichiometric (0001) surface. Oxygen thermal desorption experiments give an indication of the extent of redox associated with oxygen exposure and annealing in vacuum. Figure 52 shows a typical thermal desorption run following a 20 L $O_2$ exposure at low temperature. Using isotopic labeling, Foord and Lambert [137] have shown that the low temperature desorption features originate from molecularly adsorbed $O_2$, while the high temperature desorption features originate from dissociatively adsorbed oxygen. In our experiments, *the high temperature feature only appears following the second 20 L dose at low temperature, and increases in intensity for the next several doses.* These results indicate some irreversible uptake of dissociatively adsorbed $O_2$ which we believe is essential to repair sputter and annealing damage and facilitate the preparation of a stoichiometric surface.

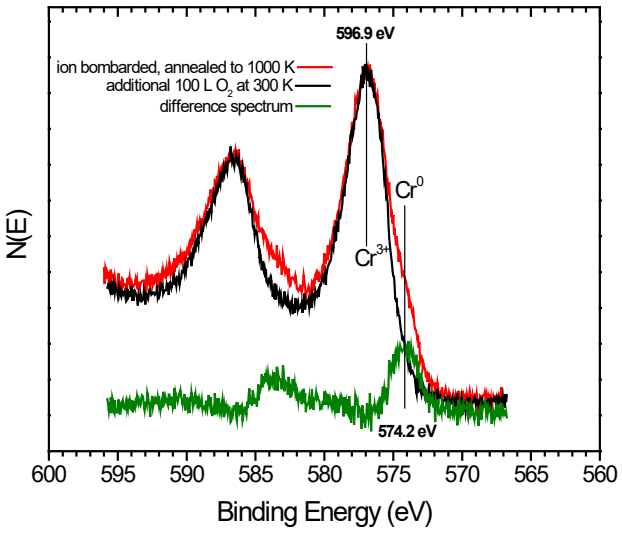


**Figure 51. Cr 2p XPS characterization of $Cr_2O_3$ (0001).**

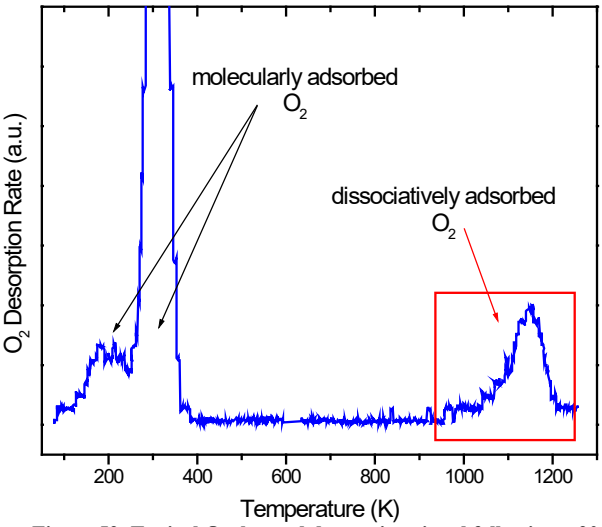


**Figure 52. Typical $O_2$ thermal desorption signal following a 20 L dose of $O_2$ $Cr_2O_3$ (0001).**

We used three different surface preparations for our reaction studies of hydrocarbon fragments: (1) ion bombarded and annealed at 1000 K, (2) bombarded and annealed surface oxygenated at 500 K for a 100 L $O_2$ dose, and (3) bombarded and annealed surface oxygenated at 500 K for a 500 L $O_2$ dose. Treatment (2) removes most of the reduced character observed in XPS for the bombarded and annealed surface but gives no oxygenated reaction products with hydrocarbon fragments in thermal desorption, while (3) gives a higher level of oxygenation, and in some cases oxygenated products like CO in our reaction studies. We believe preparation (2) most closely approximates a stoichiometric surface (although this conclusion has not been confirmed), but have found little difference in reaction chemistry between those surfaces prepared by methods (1) and (2). Preparation (3) gives rise to a surface predominantly terminated by chemisorbed O atoms.

[1] The layer layer-by-layer summation assumes a standard exponential decay of signal with increasing depth from the surface, no diffraction effects; and inelastic mean free paths of 10.0 Å for Cr 2p ($E_{kin}$ = 670 eV) and 10.1 Å for O 1s ($E_{kin}$ = 720 eV) photoelectrons. Mean free paths were estimated from the "universal curve" in reference W.M. Riggs et al., Methods of Surface Analysis, Elsevier, Amsterdam, 1975, p. 103.

**2.4.3.1 $CH_3CH_2Cl$ adsorption and the reaction of ethyl fragments on α-$Cr_2O_3$ (0001).** While the same product slate observed on α-$Cr_2O_3$ ($10\bar{1}2$) is also observed on the (0001) surface (ethene, ethane, $H_2$, halogen adatoms) the reaction chemistry is richer. *No surface carbon deposition is observed* from this reaction, and the kinetics for all the observed gas phase products are reaction limited. Figure 53 shows a typical thermal desorption run for a small 0.1 L dose on an ion bombarded and 1000 K annealed surface. Again, small doses are used to control the extent of chlorination of the surface. Ethene, ethane and $H_2$ are produced in a low temperature reaction channel between 450 and 500 K, a temperature range identical to that observed on the ($10\bar{1}2$) surface, and explainable by the same simple reaction mechanism involving a rate limiting H elimination step:

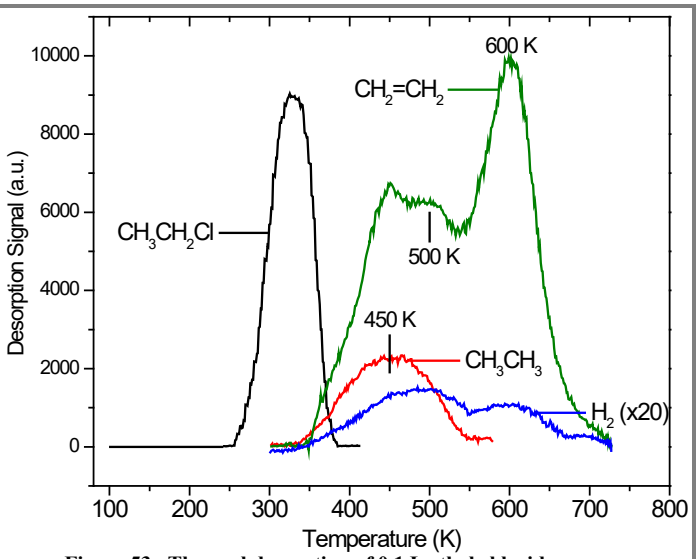


**Figure 53. Thermal desorption of 0.1 L ethyl chloride on bombarded and annealed α-$Cr_2O_3$ (0001).**

$$CH_3CH_2{-}_{(ads)} \rightarrow CH_2{=}CH_2 + H_{(ads)} \quad (1)$$
$$CH_3CH_2{-}_{(ads)} + H_{(ads)} \rightarrow CH_3CH_3 \quad (2)$$
$$H_{(ads)} + H_{(ads)} \rightarrow H_2 \quad (3)$$

A second, higher-temperature reaction channel not seen on the ($10\bar{1}2$) surface produces ethene and $H_2$ at 600 K. The simultaneous evolution of $H_2$ and ethene again indicates the rate limiting H-elimination reaction (1) seen at lower temperatures. Currently, we do not know if the lack of ethane in this reaction channel is due to the low coverage of ethyl intermediates (we have not yet examined high coverages), or due to fundamental difference in the reaction site.

We have, however, seen a variation in the intensity of the two reaction channels with surface condition. The deposition of Cl adatoms gradually closes off both reaction channels as the halogen binds at surface Cr cation sites. (A similar site blocking effect has been seen on the ($10\bar{1}2$) surface for all the halogenated reactants we have examined [66-68, 79, 128, 138-140].) However, the low temperature reaction channel shuts down much more quickly with increasing Cl coverage. This effect can be seen from the variation in the raw m/z 27 signal in thermal desorption (Figure 54) which includes contributions from the reactant and products in different temperature ranges. With each successive 0.1 L dose and subsequent thermal desorption run, the Cl adatom concentration increases (not shown), the amount of unreacted ethyl chloride increases, and the amount of product decreases. The product signal in the low temperature reaction channel (combined ethane and ethene) decreases much more rapidly that the product signal of ethene generated in the high temperature reaction channel.

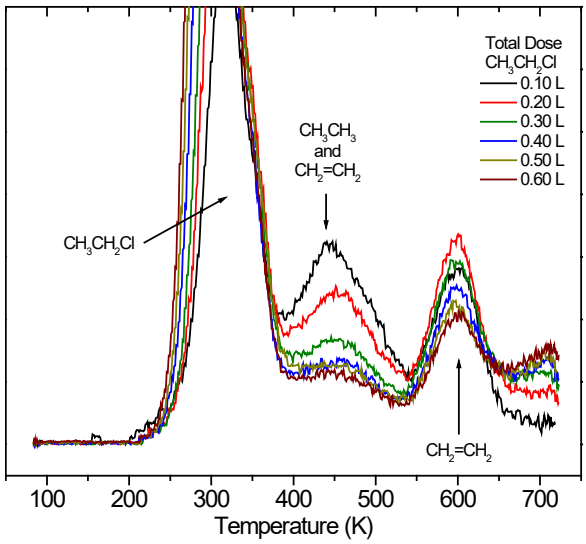


**Figure 54. Sequential 0.1 L ethyl chloride thermal desorption runs beginning on a clean, bombarded and annealed α-$Cr_2O_3$ (0001) surface.**

A similar effect is seen for the 500 L $O_2$ oxygenation treatment at 500 K (Figure 55). The product signal is greatly reduced in comparison to the bombarded and annealed surface, but the high temperature reaction channel is clearly apparent while the low temperature channel is absent. In both cases, whether the metal centers are blocked by Cl or O atoms, the low temperature reaction channel is preferentially blocked. Hence, the low temperature reaction pathway appears to be related to low coordination metal centers. This conclusion is counter intuitive when compared to our results for the $(10\bar{1}2)$ surface where highly (five) coordinated cations with a single coordination vacancy give identical reaction products in the same low temperature range.

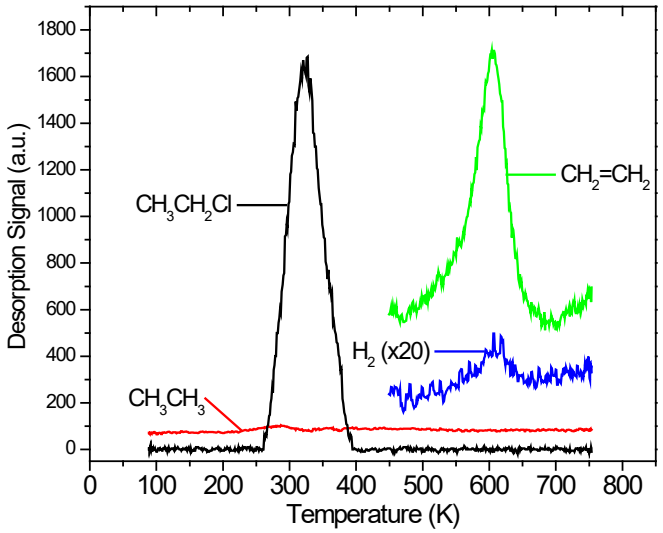


**Figure 55. 0.1 L ethyl chloride thermal desorption run on α-$Cr_2O_3$ (0001) pre-oxygenate at 500 K with 500 L $O_2$.**

These results are not clearly understood, but it appears that the local coordination of the cations may not be the primary influence on the activation barrier to ethyl dehydrogenation. An explanation more related to cation electronic properties may be applicable. With respect to formal oxidation state, the cations at the stoichiometric $(10\bar{1}2)$ and (0001) surfaces are both $Cr^{3+}$, despite the fact that their coordination numbers are five and three, respectively. With Cl (or O) atom deposition on the (0001) surface, the increased coordination of the surface cations with Cl (or O) ligands can be associated with an increase in the formal oxidation state of the Cr centers. Note that on the $(10\bar{1}2)$ surface such an effect would not be seen since coordination of a metal center with a Cl adatom caps the metal site leaving no coordination vacancy to bind and react an ethyl fragment

In addition to the remaining questions about the low-temperature reaction channel, our explanation for the high temperature reaction channel is speculative. Its strong intensity in thermal desorption from the bombarded and annealed surface argues against its association with a highly coordinated cation site, and while diminished in intensity, it persists even on a highly oxygenated surface. As a result of these observations, an O-atom bound intermediate like ethoxide ($CH_3CH_2$–O–) cannot be ruled out. Two negative observations argue against the involvement of such a species. (1) On the $(10\bar{1}2)$ surface, we have seen no clear indication of any O-bound fragments in synchrotron-based XPS, and (2) we see none of the expected acetaldehyde product ($CH_3CHO$) that might result from β-H elimination from an ethoxide intermediate. However, since the O atom involved would originate from strongly-bound surface lattice oxygen, a different decomposition pathway might be operable. Our planned synchrotron-based XPS studies should be able distinguish between O and Cr bound intermediates. Additionally, ethanol reaction studies on partially reduced and stoichiometric surfaces to produce ethoxide by dissociative alcohol adsorption could help distinguish between the chemistry of an ethoxide bound through a lattice O atom or a chemisorbed O adatom. On a stoichiometric surface, the ethoxide generated from ethanol dissociation should closely approximate an ethyl fragment bound at a surface O adatom. On a partially reduced surface, the O atom from ethanol should fill an oxygen vacancy and give an ethoxide characteristic of an ethyl fragment bound to a surface lattice oxygen atom.

**2.4.3.2 $CH_3CHCl_2$ adsorption and the reaction of ethylidene fragments on α-$Cr_2O_3$ (0001).** As with the stoichiometric $(10\bar{1}2)$ surface, the primary product from the reaction of ethylidene on the bombarded and annealed (0001) surface is ethene as shown in Figure 56 for a 0.1 L dose of 1,1-dichloroethane. However, while ethene was the only product formed on $Cr_2O_3$ $(10\bar{1}2)$, a wider range of minor products is observed from $Cr_2O_3$ (0001) including acetylene, ethane, $H_2$, and 2-butene (note the ×10 scale factors). The major product ethene is observed in two main peaks at 375 and 450 K temperature, similar to the 430 K isomerization temperature on $Cr_2O_3$ $(10\bar{1}2)$, and in a smaller shoulder near 585 K. *A trace of surface C can be seen in post reaction AES* following many thermal desorption runs.

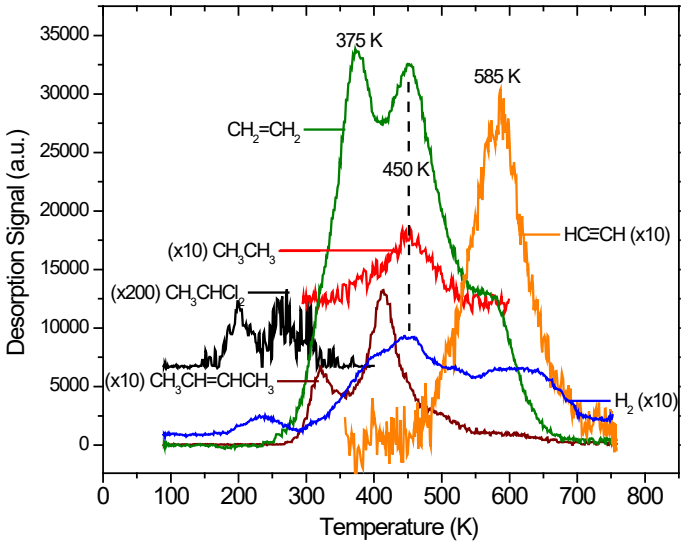


**Figure 56. 0.1 L $CH_3CHCl_2$ thermal desorption run on bombarded and annealed α-$Cr_2O_3$ (0001).**

Acetylene and $H_2$ are secondary products in the 585 K channel indicating a dehydrogenation reaction in parallel with ethene formation. Acetylene formation can occur at 585 K through a β-H elimination from ethylidene to form vinyl, followed by H-elimination from vinyl to acetylene (Scheme 5). Support for this assignment comes from preliminary reaction studies of vinyl chloride on this same surface (not shown) which gives acetylene at 580 K from vinyl decomposition by H-elimination.

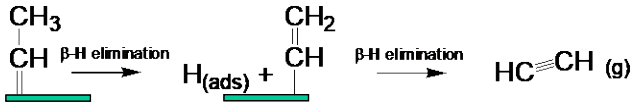


**Scheme 5. 585 K dehydrogenation route from ethylidene to acetylene on bombarded and annealed α-$Cr_2O_3$ (0001).**

The intensity of the 585 K reaction channel is rapidly attenuated by the build up of Cl adatoms (not shown). Exposure and reaction of as little as 0.15 L of 1,1-dichloroethane blocks acetylene formation, while 0.25 L shuts down ethylene formation at 585 K. These observations suggest reaction sites of low-coordination Cr cations (primarily 3-coordinate?) that are rapidly lost by coordination with Cl adatoms.

For the 450 K reaction channel, $H_2$ and ethane are generated, indicating another dehydrogenation pathway in parallel with the ethene formation reaction. The 450 K temperature is the same as that observed for ethane formation from the dehydrogenation of ethyl intermediates (Figure 53) on this same surface. Ethylidene hydrogenation to an ethyl intermediate is, therefore, a likely route, yielding ethane, $H_2$ and some fraction of the ethene observed at 450 K. However, given that only about 5% of the $C_2$ product is generated by a dehydrogenation (acetylene) or hydrogenation (ethane) pathway, it appears that the primary route to ethene from $CH_3CHCl_2$ is ethylidene isomerization as was seen on $Cr_2O_3$ $(10\bar{1}2)$. In fact, the lowest temperature ethene production channel at 375 K in Figure 56 does not coincide with any other $C_2$ products, suggesting that there are no accompanying hydrogenation/dehydrogenation pathways in parallel with ethene production via ethylidene isomerization.

A small amount of 2-butene production is also observed from the ion bombarded and annealed surface, and can be described as a coupling reaction of two ethylidene species:

$$2\ CH_3CH=_{(ads)} \rightarrow CH_3CH=CHCH_3$$

As Cl builds up on the surface, the coupling reaction shuts down. On $Cr_2O_3(10\bar{1}2)$, no coupling reactions were observed for any of the $C_2$ alkyl intermediates, although vinyl coupling to 1,3-butadiene and methylene coupling (another carbene) to ethene were seen. In those cases, surface diffusion of the reaction intermediates was proposed as a necessary step to coupling since the cations on $(10\bar{1}2)$ have but a single coordination vacancy [79, 128, 138, 140]. For the (0001) surface, the surface cations have a larger separation than those on $(10\bar{1}2)$, 4.96 vs 3.65 Å, but the cations on the stoichiometric surface expose three coordination vacancies. As proposed by Barteau [3], we believe the site requirement for this coupling reaction involves two intermediates accommodated in the multiple coordination vacancies on a single surface cation site. The production of 2-butene drops off slowly with increasing Cl adatom coverage, so in the future we may be able to use the ethylidene coupling reaction to relate the Cl surface concentration to the loss of cation sites with multiple coordination vacancies.

What is still unclear is the origin of the multiple temperature regimes for ethene production. While the highest temperature channel appears to be related to low-coordination metal sites (described above), the 375 and 450 K channels do not show the same rapid decrease with Cl deposition. The reaction temperatures do drift downward, to 330 and 415 K, respectively, but decrease slowly in intensity with halogen deposition.

Substantial differences are observed when the surface is terminated with O atoms using the 500 L $O_2$ oxygenation treatment at 500 K. Figure 57 show the results of an 0.1 L $CH_3CHCl_2$ thermal desorption run on the oxygenated surface. Note Figure 57 shows the 5th consecutive 0.1 L reaction run. The reactivity is substantially lower than on the bombarded and annealed surface, with much more 1,1-dichloroethane desorbing unreacted (note the ×10 scale factor compared to ×200 in Figure 56). Ethene is again observed in three temperature ranges as before, but at less than 20% of the intensity seen on the bombarded and annealed surface. Conversely, the acetylene signal is 5-6 times larger and at a higher desorption temperature (635 vs 585 K). Acetylene production is also accompanied by CO. (Note: a small water signal is also observed, but is difficult to pull from the background water in the chamber for these small doses.) Other observations (not shown) are consistent with a small number of reaction sites on the oxygenated surface, with additional reaction sites generated in successive runs by the removal of O adatoms through CO and $H_2O$ formation. The ethene signal is initially half that shown in Figure 57, with no high temperature contribution. Successive reaction runs open up the high temperature ethene production channel by the removal of surface O atoms, consistent with suggestions above that these sites are associated with low-coordination cation sites. However, the propensity to form acetylene and CO rather than ethene suggests both nucleophilic attack of surface O atoms at ethylidene C atoms (for CO formation), and enhanced H-elimination to nearby O adatoms (rather than isomerization) to assist the dehydrogenation route to acetylene (Scheme 5).

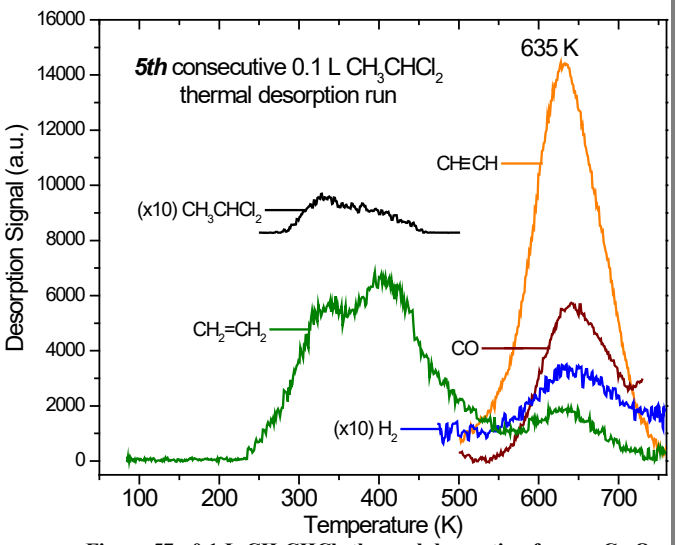


**Figure 57. 0.1 L $CH_3CHCl_2$ thermal desorption from α-$Cr_2O_3$ (0001) pre-oxygenate at 500 K with 500 L $O_2$.**

**2.4.3.3 $CH_3CCl_3$ adsorption and the reaction of ethylidyne fragments on α-$Cr_2O_3$ (0001).** As with the stoichiometric ($10\bar{1}2$) surface, the primary reaction products from ethylidyne on the bombarded and annealed (0001) surface are acetylene, ethene and $H_2$ (Figure 58). *Trace surface C can be seen in post reaction AES* following many thermal desorption runs. Similar to the observations made for the ($10\bar{1}2$) surface, ethylidyne dehydrogenation is rate-limiting, but with a lower activation barrier to β-H elimination of 35.9 kcal/mol (570 K) compared to 39.5 kcal/mol (620 K) on ($10\bar{1}2$). We believe the reaction proceeds in a fashion similar to that proposed above for the ($10\bar{1}2$) surface: (1) ethylidyne dehydrogenation to vinylidene (Scheme 3) with subsequent isomerization of vinylidene to acetylene, and (2) ethylidyne hydrogenation to ethylidene (Scheme 4) followed by (predominantly) ethylidene isomerization to ethene as described in section *2.3.2* above. We have not yet examined the reactions of vinylidene on the (0001) surface, so proposal (1) is speculative.

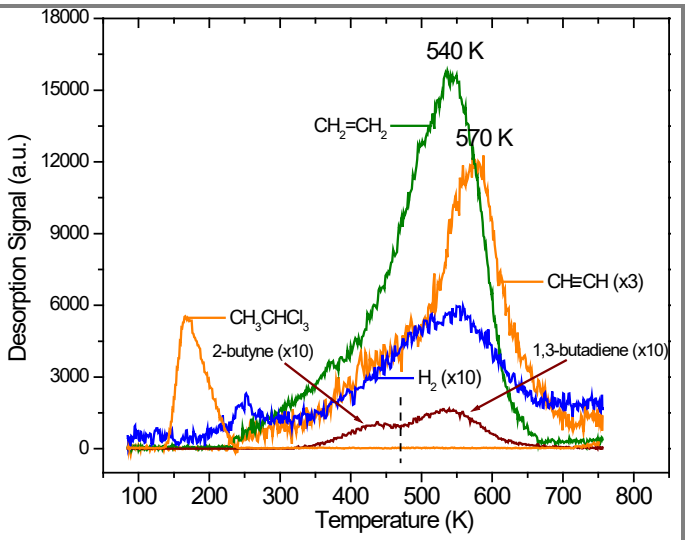


**Figure 58. 0.05 L $CH_3CCl_3$ thermal desorption run on bombarded and annealed α-$Cr_2O_3$ (0001).**

In addition to the observed $C_2$ products, there is also evidence for small amounts of $C_4$ coupling products 2-butyne ($CH_3C{\equiv}CCH_3$) and 1,3-butadiene ($CH_2{=}CH{-}CHCH_2$) shown in Figure 58, and trace amounts of 2-butene ($CH_3CH{=}CHCH_3$) not shown. Note that because 2-butyne and 1,3 butadiene have the same molecular weight, we cannot readily separate their signals via subtraction in Figure 58. However, the m/z=54 signal used to track both molecules exhibits two desorption features: a low-temperature shoulder at 440 K, and a peak at 535 K. Comparison of the m/z 53 and 54 signals with experimental fragmentation patterns for $C_4$ compounds suggests the lower temperature feature is predominantly 2-butyne (2:1 ratio of m/z 54:53), while the higher temperature peak is 1,3-butadiene (5:4 ratio of m/z 54:53). The observed $C_4$ products 2-butyne, 1,3-butadiene and 2-butene are assumed to be coupling products from ethylidyne, vinyl, and ethylidene, respectively. Given the multiple lower temperature routes to ethylidene isomerization (to ethene, section *3.3.2*), one can understand why little of the ethylidene formed via Scheme 4 would be available for coupling. The route to vinyl formation from ethylidyne is not clear. Hydrogenation by α-hydrogen addition to vinylidene formed via Scheme 3 (above) is a possibility, as is ethylidyne isomerization.

Variations of most of the reaction product signals with increasing Cl adatom coverage shows a gradual drop off with consecutive thermal desorption runs and Cl deposition. However, 2-butyne drops of much more rapidly, showing no product while signals for the other molecules persist. This again, as was seen for ethylidene coupling to 2-butene, is an indication that the ethylidyne coupling reaction likely occurs at cation sites with multiple coordination vacancies. The persistence of vinyl coupling to 1,3-butadiene is similar to earlier observations on the ($10\bar{1}2$) surface where coupling occurs even when multiple coordination vacancies are not available.

### 2.4.4 Related chemisorption work on α-$Cr_2O_3$ (0001)

Our characterization and reaction work on α-$Cr_2O_3$ (0001) indicates the need for chemisorption probe molecules capable of distinguishing between cation sites of differing coordination and oxidation state. To date, our work has focused on initial surface preparation via ion bombardment, annealing and oxidation treatments to vary the starting surface condition.

***2.4.4.1 CO thermal desorption experiments.*** Freund and coworkers have shown that CO chemisorbs parallel to the surface in an $O_3$-hollow site on α-$Cr_2O_3$ (0001) with the C and O atoms oriented towards neighboring surface $Cr^{3+}$ cations [141, 142]. These chemisorption sites will be disrupted as Cl deposition changes the coordination of the three-fold coordinated $Cr^{3+}$ cations on the stoichiometric (0001) surface. Preliminary evidence of the sensitivity of CO is found in Figure 59. While our CO thermal desorption data shows more structure than that of Freund and coworkers, we do get a clear indication of a high-temperature CO desorption state (305-240 K) that is present when reduced chromium species appear in XPS (Figure 59a). Oxygenation with 100 L $O_2$ at 500 K removes the reduced signal in XPS, and eliminates the higher temperature desorption signal (Figure 59b). Similarly, we have found $CO_2$ thermal desorption to be sensitive to variations in chromium coordination number on α-$Cr_2O_3$ ($10\bar{1}2$) [86]. The combination of these two probe molecules should make it possible for us to characterize the variation in the coordination of chromium cations on α-$Cr_2O_3$ (0001) with varying Cl coverage.

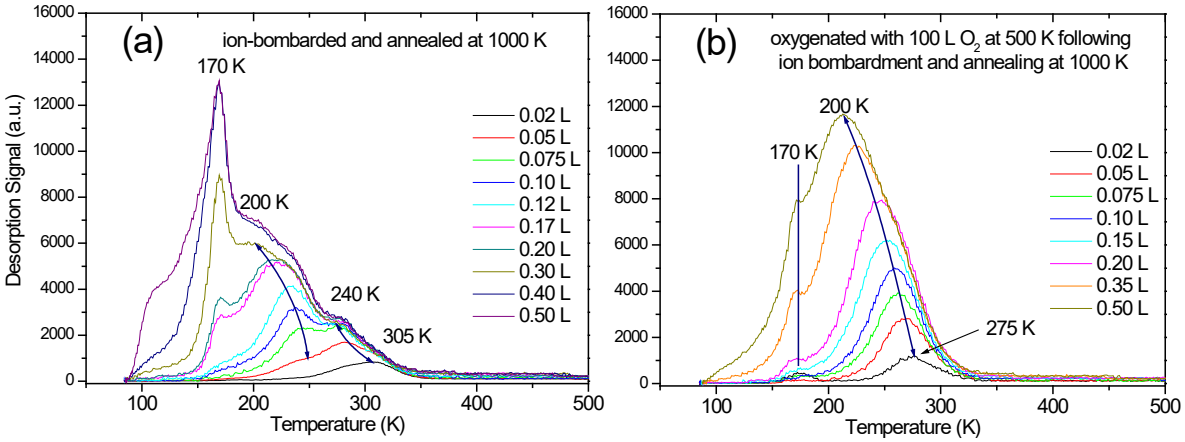


**Figure 59. CO thermal desorption from a $Cr_2O_3$ (0001) surface prepared by (a) ion bombardment and annealing in vacuum, and (b) the surface in (a) oxygenated with 100 L O2 at 500 K.**

**2.4.4.2 Acetylene thermal desorption experiments.** In earlier budget periods we found that acetylene chemisorbs molecularly on α-$Cr_2O_3$ ($10\bar{1}2$) without reaction, and desorbs at 315 K in thermal desorption near the limit of zero coverage. We find dramatically different results for the (0001) surface. Figure 60 shows the chemistry observed during the adsorption and reaction of acetylene on α-$Cr_2O_3$ (0001). Benzene evolves at 400 K as a result of acetylene cyclotrimerization, a reaction that is well known on a number of metal and oxide surfaces [117, 132, 143-150]. Similarly, $Cr^{3+}$ organometallic compounds are known that catalyze ethene and primary alkyn trimerization [151, 152]. This reaction is particularly important for our studies because acetylene does not deposit halogen and modify the Cr cation coordination or oxidation state as do our usual precursors to alkyl and alkenyl fragments. This reaction is, therefore, clearly related to the higher number of coordination vacancies on Cr cations on the (0001) surface. In addition to cyclotrimerization, complete dehydrogenation and surface carbon deposition is also observed.

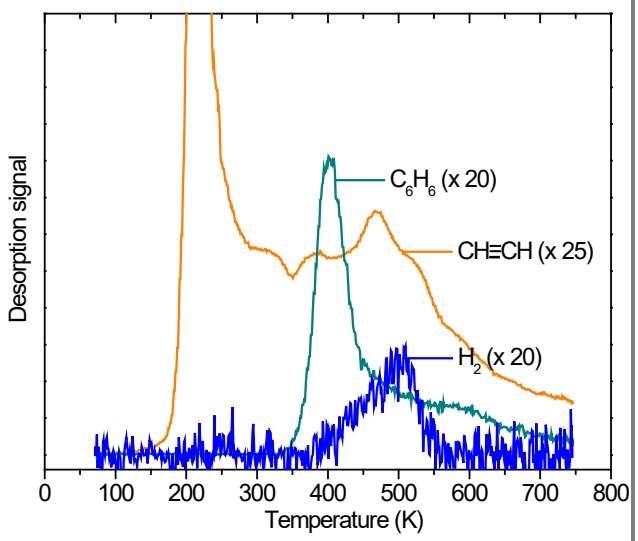


**Figure 60. Thermal desorption for the reaction of 0.1 L of acetylene on α-$Cr_2O_3$ (0001).**

We have also examined the adsorption of ethene, the primary reaction product from ethyl and ethylidene intermediates on the $Cr_2O_3$ (0001) surface. As found

previously for the $(10\bar{1}2)$ surface, there is no evidence for a reaction of ethene, just molecular adsorption and desorption.

### 2.4.5 Surface characterization and reaction studies on $\alpha$-$Fe_2O_3$

Our original plan was to begin work on $\alpha$-$Fe_2O_3$ $(10\bar{1}2)$ to facilitate a comparison to the variety of reaction data we have accumulated over the isostructural $\alpha$-$Cr_2O_3$ $(10\bar{1}2)$ surface, and provide a direct experimental interrogation of a nearly-pure electronic effects in the surface chemistry. This work was slowed initially by the delayed arrival of the single crystal sample, then a delay was experienced in the characterization by an electron gun/electronics failure in both of our 20-year-old sets of LEED optics that are no longer manufactured, requiring replacement with a new set of optics. While waiting on the arrival of the optics, we examined surface preparation recipes utilizing laboratory-based XPS measurements and $O_2$ thermal desorption to characterize the redox characteristics of the surface.

As expected for this reducible oxide, ion bombardment in UHV gives a partially reduced surface. Annealing in vacuum at temperatures of 600 K or above increases the XPS O/Fe ratio from about 1.4 to 2.1 ± 0.07 using Shirley background subtraction and atomic sensitivity factors characteristic for our analyzer. The Fe 2p lines sharpen with annealing, but oxygenation at elevated temperature (using recipes described in [153, 154]) is necessary to give a narrow Fe $2p_{3/2}$ line at a binding energy of 711.2 eV characteristic of $Fe^{3+}$ (Figure 61). A difference spectrum indicates that the primary reduced oxidation state following ion bombardment and annealing is $Fe^{2+}$ [155, 156]. Post oxidation annealing in vacuum up to 750 K results in no new introduction of reduced surface Fe.

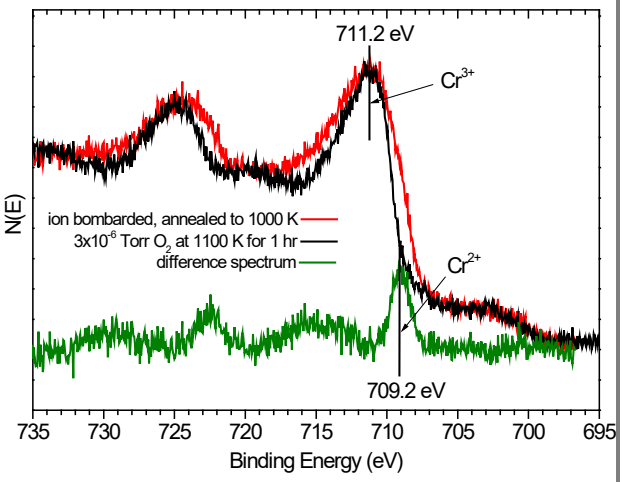


**Figure 61. Fe 2p XPS characterization of single-crystal $Fe_2O_3$.**

A sharp pattern is obtained in LEED for annealing temperatures of 900 K and above following ion bombardment, and also after oxidation treatments. The same oblique 2D unit cell (see figure) is observed for both the ion bombarded/annealed and oxidized surface as shown in Figure 62. While there is no indication of a reconstruction due to the presence of reduced surface species (following ion bombardment) or after oxidation, there is an indication of weak spot-splitting (Figure 62). The primary conclusion of the LEED study is that the crystal is **not** oriented to a $\alpha$-$Fe_2O_3$ $(10\bar{1}2)$ surface as we wished, nor does it correspond to a (0001) surface like that currently under study for $\alpha$-$Cr_2O_3$. The measured cell shape and size in Figure 62 (<75°; a/b=0.61) best matches that for the low index $(11\bar{2}1)$ surface (<72.7°; a/b=0.59) as derived from the crystal structure data of Blake et al. [157] for hematite.

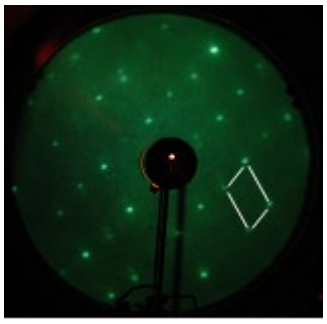

**Figure 62. LEED characterization of our $\alpha$-$Fe_2O_3$ single crystal surface (96 eV). The sample is oriented to $(11\ \bar{2}\ 1)$.**

From an examination of the hematite crystal structure along $[11\bar{2}1]$ it appears the surface is nonpolar, but any termination of the stoichiometric six atomic layer repeat unit perpendicular to the surface will expose surface cations with coordination numbers ranging from three to five (Figure 63). We expended considerable effort collecting $C_1$ reaction data for methyl and methylene groups (from iodomethane and diiodomethane, respectively) on this surface before our LEED characterization. We found no apparent reaction of methyl fragments from $CH_3I$, similar to recent observations for methyl fragments on $\alpha$-$Fe_2O_3$

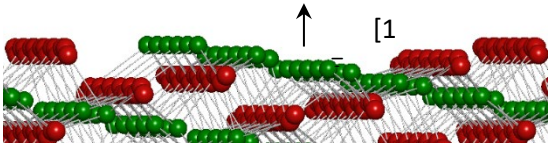


**Figure 63. Side view of the $Fe_2O_3$ $(11\bar{2}1)$ surface. Red spheres are O anions, green spheres are Fe cations**

(0001) [158], and the formation of formaldehyde ($CH_2O$) but no coupling products from methylene fragments. However, given the complexity of the surface structure, we abandoned these experiments while waiting for a $Fe_2O_3\,(10\bar{1}2)$ sample from a new supplier.

### 2.4.6 Computational Investigations of α-$Cr_2O_3$ $(10\bar{1}2)$ surface chemistry.

In an earlier budget period, we found experimentally that several hydrocarbon fragments can couple on α-$Cr_2O_3\,(10\bar{1}2)$ to form higher molecular weight species. Examples included (1) methylene coupling to ethene,

$$2\ CH_2 \rightarrow CH_2{=}CH_2 \qquad (1)$$

(2) methylene insertion into a $CH_3$–Cr bond to form surface ethyl with ethene formed by subsequent β-H elimination,

$$CH_3{-} + CH_2{=} \rightarrow CH_3CH_2{-} \rightarrow CH_2{=}CH_2 + H \quad (2)$$

and (3) vinyl coupling to 1,3-butadiene,

$$2\ CH_2{=}CH{-} \rightarrow CH_2{=}CH{-}CH{=}CH_2 \qquad (3)$$

The intriguing part of this chemistry is that α-$Cr_2O_3$ $(10\bar{1}2)$ does not meet the expected site requirements for such reactions [3], i.e. multiple coordination vacancies on the cation sites. We proposed that the reactions are mediated by surface diffusion to bring the fragments into close proximity with an activation barrier for diffusion below that for fragment dehydrogenation (decomposition) [79, 128, 138, 140].

Our plan for the past budget period was to begin a DFT investigation using the climbing image [159-161] nudged elastic band method (NEB) [159-161] implemented within the Vienna Ab-initio Simulation Package (VASP) [54-56, 75, 76] to examine first the reaction coordinate of methylene surface diffusion, followed by a study of the coupling and dehydrogenation reactions. Our efforts were hampered by prolonged delays in compiling a working copy of the code on our "home built" campus supercomputer, System X. Over a period of several years, multiple compilers and multiple operating systems (on different partitions of the cluster) were tried by the support staff to remedy the problem. This problem was not limited to the implementation of VASP, but several other parallelized electronic structure codes as well. During that time, we were able to investigate adsorbate binding geometries on a smaller campus cluster, but lacked the computational resources to run NEB investigations of minimum energy pathways for reactions. The problems have been overcome, and we have had access to these tools with significant computational power on System X since mid-September 2008. The results generated in the intervening time as we gain experience with the NEB calculations have been very encouraging. These preliminary results are described below.

**2.4.6.1 Methylene diffusion on $Cr_2O_3\,(10\bar{1}2)$.** Our experimental synchrotron XPS data (not shown) indicates the formation of surface methylene from diiodomethane, $CH_2I_2$, with a C 1s binding energy consistent with methylene bound at a Cr sites. Similarly, DFT predicts Cr cations as the lowest energy methylene binding sites. Experimentally, we observe two methylene coupling channels in thermal desorption with apparent first-order activation energies of 18.3 and 24.0 kcal/mol [79]. Because of the corrugated surface structure (Figure 64), diffusion of methylene between cation sites might occur across "troughs" (blue arrows) or over "zig-zag" rows of coordinately unsaturated O anions in the outer atomic layer (yellow arrows). The separation between the neighboring cations along these four paths is identical.

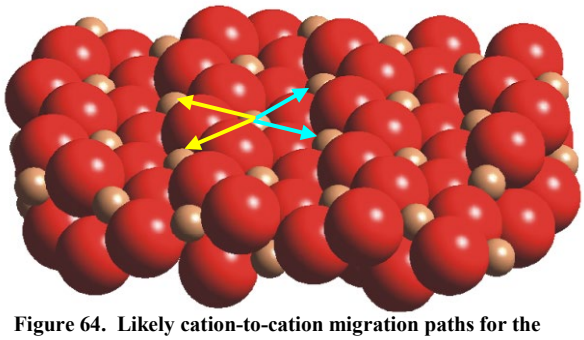

**Figure 64. Likely cation-to-cation migration paths for the activated diffusion of methylene fragments on stoichiometric α-$Cr_2O_3$ $(10\underline{1}2)$. The "cross-trough" path is illustrated by the right-pointing blue arrows, and the over "zig-zag" row path is illustrated by the left-pointing yellow arrows.**

For the path across a trough, the NEB method predicts a transition state with methylene bridged symmetrically between neighboring cation sites across the trough with an activation barrier for diffusion of 16.1 kcal/mol. For diffusion over the zig-zag rows of surface oxygen, we anticipated either an atop path over an O atom (a formaldehydic transition state), or methylene bridged between two O atoms (a dioxymethylene transition state). Interestingly, the NEB method gives a different minimum energy pathway (Figure 65) involving a methylene species bridged between a Cr cation and a neighboring O anion site with an activation barrier to diffusion of 11.4 kcal/mol. The bridging species occur at a local minimum in the potential energy surface along the reaction coordinate. The combination of the two diffusion pathways provides a route across the surface between any nearest neighbor Cr cation sites.

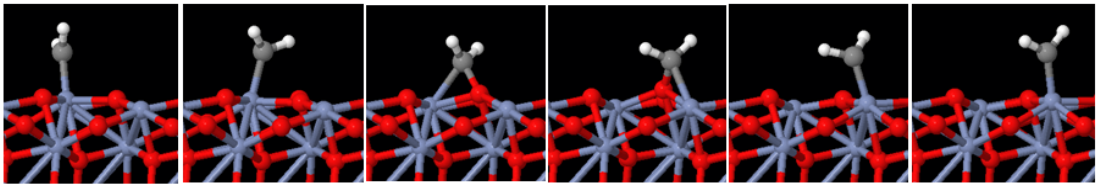

**Figure 65. Minimum energy diffusion pathway with methylene bridged between surface Cr cations (blue) and O anions (red).**

We have also examined the coupling process between neighboring methylenes across a surface trough to form chemisorbed ethylene. The prediction gives an exothermic reaction ($\Delta H_r$= -59.6 kcal/mol) with an activation barrier to coupling of 13.3 kcal/mol, only slightly higher than the barrier to diffusion across the trough. The transition state, shown in Figure 66, precedes a more stabilized di-σ bonded ethene-like moiety bridged between the adjacent cations along the reaction coordinate enroute to an ethene molecule π bonded at a single cation site.

Work is also underway to examine the coupling process for a surface methylene following the Cr–$CH_2$–O bridging pathway for diffusion. We are curious to see if ability to bridge to a surface O atom stabilizes the transition state to give a lower activation barrier to coupling. Other processes we intend to examine computationally are those indicated by our experimental reaction studies on α-$Cr_2O_3$ ($10\bar{1}2$) including the influence of surface halogen on these direct methylene coupling reactions, methylene dehydrogenation, methylene hydrogenation to methyl, and methylene insertion into methyl to form a surface ethyl intermediate (an alternative coupling route to ethene).

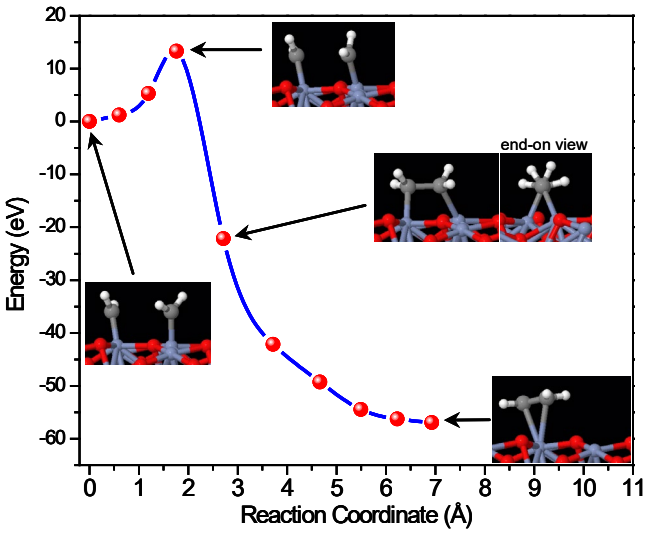


**Figure 66. Minimum energy pathway for methylene coupling across a $Cr_2O_3$ ($10\bar{1}2$) trough.**

It is noted that the experimental activation barriers to methylene coupling are 7-8 kcal/mol larger than the barriers predicted with DFT for the two routes to methylene diffusion and the single barrier to coupling that we have examined. The discrepancies may be due to the influence of surface halogen in the experiment, or the DFT method employed. DFT provides reasonable geometries for the ($10\bar{1}2$) surface and adsorbates, but the energetics are still in question. For example, DFT predicts a bulk $Cr_2O_3$ band gap of ~1.5 eV compared to the experimental value of ~3.4 eV, and while DFT typically under-predicts band gaps, we may encounter additional problems because of strong electronic correlation effects in $Cr_2O_3$ [74]. Hafner and coworkers have included a Hubbard-type on-site coulomb repulsion term (the so called DFT+U approach) at the spin-polarized GGA level (GGA+U) [82] and found parameter values that lead to an acceptable compromise between the bulk structural and electronic properties of $Cr_2O_3$ [74]. When applied to the α-$Cr_2O_3$ (0001) surface, they obtain quantitative agreement with the experimental surface geometry

determined with LEED, and are able to predict the stability of the Cr-terminated surface observed experimentally over a wide range of oxygen partial pressures [74]. We are in the process of generating results for simple adsorbates on α-$Cr_2O_3$ $(10\bar{1}2)$ to compare to experiment.

## 2.5 Results and Accomplishments 5/1/2009 – 4/30/2012

During this budget period we pursued three different lines of investigation. (1) We examined the reaction chemistry of $C_1$ fragments (methyl and methylene) on α-$Cr_2O_3$ (0001) experimentally and computationally to look for structure sensitivity compared to our results from the $(10\bar{1}2)$ surface. (2) We looked for ways to experimentally control the cation coordination number on $Cr_2O_3$ (0001) through the controlled addition of Cl adatoms as a basis for explaining multiple reaction channels of $C_2$ alkyl fragments observed in an earlier project period. (3) We have studied the reaction chemistry of $C_1$ fragments over $Fe_2O_3$ $(10\bar{1}2)$ for comparison to our $Cr_2O_3$ $(10\bar{1}2)$ results to directly characterize the impact of cation d electron density in the absence of structural effects.

### 2.5.1 Structure Sensitivity in Reactions of $C_1$ fragments on α-$Cr_2O_3$?

**2.5.1.1 Methyl, ·$CD_3$, reactions on stoichiometric α-$Cr_2O_3$ $(10\bar{1}2)$ and (0001).** The adsorption and reaction of methyl iodide ($CD_3I$) in TPD on the two structurally-different surfaces of α-$Cr_2O_3$ gives rise to the same product slate: $CD_4$, $CD_2$=$CD_2$, $D_2$, and trace surface carbon. All products are reaction limited, with the first-order dehydrogenation of surface methyl being the rate-limiting step. The reaction network can be described by the following elementary reactions on both surfaces:

$$CD_3{-}_{(ads)} \rightarrow CD_{2(ads)} + D_{(ads)} \quad (1)$$

$$CD_3{-}_{(ads)} + D_{(ads)} \rightarrow CD_4 \quad (2)$$

$$D_{(ads)} + D_{(ads)} \rightarrow D_2 \quad (3)$$

TPD data for the two surfaces are shown in Figures 67 and 68. Despite the significant difference in cation coordination numbers for the two surfaces (five vs three for $(10\bar{1}2)$ and (0001), respectively) the similarity in the methyl dehydrogenation temperatures for the two surfaces indicates there is no significant structure sensitivity in the methyl decomposition reaction associated with changes in the cation coordination number or the local oxygen anion site geometry. We find this result surprising.

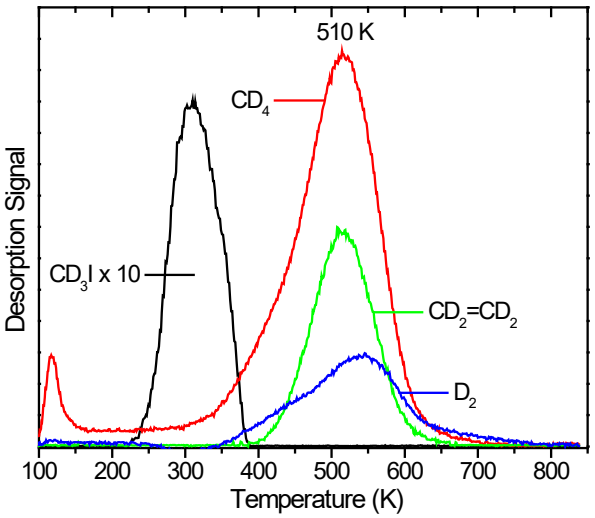


**Figure 67. Thermal desorption following a 0.1 L dose of $CD_3I$ on stoichiometric α-$Cr_2O_3$ $(10\bar{1}2)$.**

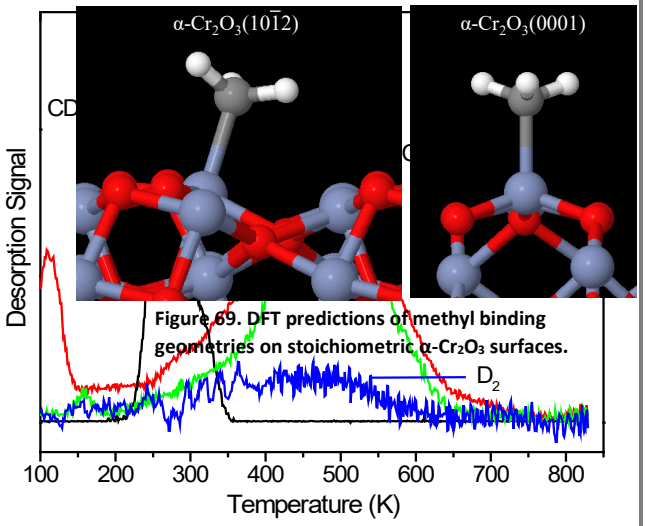


**Figure 68. Thermal desorption following a 0.1 L dose of $CD_3I$ on stoichiometric α-$Cr_2O_3$ (0001).**

**Figure 69. DFT predictions of methyl binding geometries on stoichiometric α-$Cr_2O_3$ surfaces.**

XPS results for methyl iodide adsorption and dissociation (not shown) suggests the possibility of methyl binding on both cation (metal alkyl, Cr-$CH_3$) and anion (methoxide, O-$CH_3$) sites on both surfaces. However, DFT predicts only a stable cation-bound methyl on both surfaces of α-$Cr_2O_3$. (Discrepancies between experiment and DFT are discussed in more detail below in section 3.1.3) For the cation-bound methyl

fragments, DFT indicates that neither surface provides oxygen anions in close proximity to the methyl hydrogen to aid in the hydrogen abstraction (methyl dehydrogenation) reaction (Figure 69).

**2.5.1.2 Experimental examination of methylene, :$CH_2$, reactions on stoichiometric α-$Cr_2O_3$ ($10\bar{1}2$) and (0001).** The methylene coupling process observed above as a result of methyl dehydrogenation was studied directly using dihalogenated methane to generate surface methylene species directly. The adsorption and reaction of dihalomethane ($CH_2I_2$ or $CH_2Cl_2$) in TPD on the two structurally-different surfaces of α-$Cr_2O_3$ gives rise to two gas phase reaction products: the primary product is ethylene ($CH_2$=$CH_2$) from the coupling reaction between two surface methylene species, small amounts of methane ($CH_4$), and trace surface carbon. Methane production occurs at the same temperature observed for methyl ($\cdot CH_3$) dehydrogenation (above).

Since methylene dehydrogenation is expected to require a higher temperature than methyl dehydrogenation in TPD, isotopic labeling studies were undertaken to determine the source of H atoms responsible for the hydrogenation of surface methylene to methyl. The reaction of $CD_2I_2$ leads to $CD_2H_2$ as the majority forms of methane, indicating that the source of H atoms for the hydrogenation step is background hydrogen/water from the chamber rather than methylene dehydrogenation.

TPD and XPS data for the reaction of $CH_2I_2$ on α-$Cr_2O_3$ ($10\bar{1}2$) are shown in Figure 70. Two reaction channels to ethylene are observed in TPD for consecutive small (0.05 L) doses of $CH_2I_2$, with apparent 1st order activation barriers of 0.80 eV and 1.05 eV for the initial doses where the coverage of surface I from the dissociation reaction is low (Figure 70a). The high temperature reaction channel (390 K) is clearly reaction limited, while the 300 K temperature for the low-temperature reaction channel is slightly above the desorption-limited temperature of 285 K observed for a small coverage of dosed ethylene on this surface. Synchrotron-based XPS (Figure 70b) following a saturation dose with subsequent heating clearly shows the surface methylene is bound at a cation site since a higher binding energy of 286 eV or more is expected for an oxygenated surface carbon species.

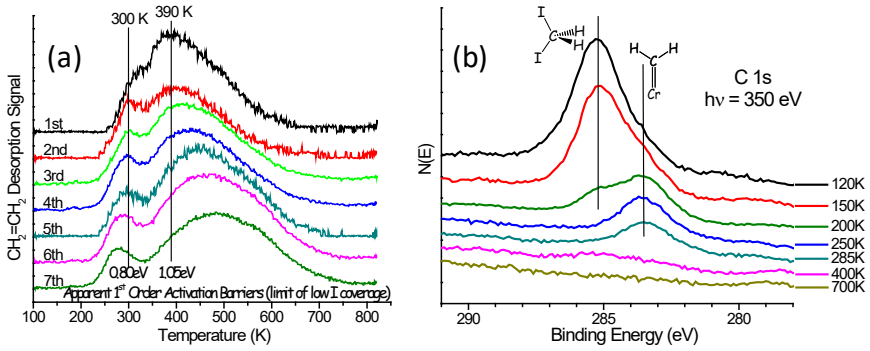


**Figure 70. Reaction of methylene on α-$Cr_2O_3$ ($10\bar{1}2$). (a) TPD for consecutive 0.05 L doses of $CH_2I_2$, and (b) synchrotron-based XPS following a saturation dose with subsequent heating.**

Similar XPS results (not shown) are obtained for the reaction of $CH_2Cl_2$ on α-$Cr_2O_3$ (0001), showing a cation-bound methylene reaction intermediate. TPD data (Figure 71) show the coupling reaction of methylene exhibits two reaction channels to ethylene, but at significantly different temperatures than on the ($10\bar{1}2$) surface, indicating the coupling reaction is structure sensitive. The high temperature (475 K) reaction channel on the (0001) surface is 85 K higher than observed on the ($10\bar{1}2$) surface, while the low temperature channel (255 K) is clearly desorption limited when compared to TPD data for dosed ethylene on this surface.

Most of our understanding of carbon-carbon bond making reactions on oxide surfaces originates from the work of Barteau [3] that suggests that multiple coordination vacancies on a single cation site are required to accommodate the two ligands involved in the coupling reaction. As a result, the observed coupling of methylene to ethylene ($2\ CH_{2(ads)} \rightarrow CH_2{=}CH_{2(g)}$) over the $\alpha$-$Cr_2O_3$ $(10\bar{1}2)$ surface was unexpected because the surface cations provide only a single coordination vacancy. Our observations of methylene coupling over $\alpha$-$Cr_2O_3$ $(10\bar{1}2)$ from an earlier project period led us to consider a process involving surface diffusion and reaction described below (section 2.5.1.3).

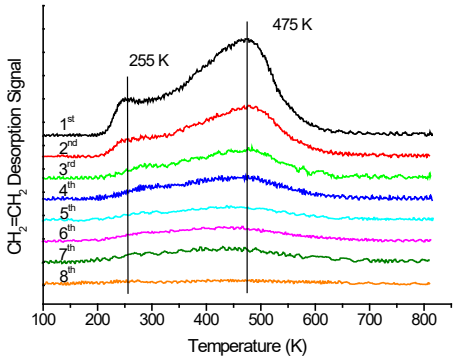


**Figure 71. Reaction of methylene on α-$Cr_2O_3$ (0001) for consecutive 0.10 L doses of $CH_2Cl_2$. Cl adatoms from the dissociation reaction reduce the reactivity via site blocking.**

**2.5.1.3 DFT examination of methylene, :$CH_2$, diffusion and coupling to ethylene on stoichiometric α-$Cr_2O_3$ $(10\bar{1}2)$ and (0001).** During a previous project period, we generated preliminary computational results with DFT for two different surface diffusion pathways on α-$Cr_2O_3$ $(10\bar{1}2)$. During the most recent project period we have completed our DFT examination of this process on both the $Cr_2O_3$ $(10\bar{1}2)$ and (0001) surfaces. We have utilized the climbing image [159-161] nudged elastic band method [159-161] implemented within the Vienna Ab-initio Simulation Package (VASP) [54-56, 75, 76].

There are two primary issues to consider in these calculations. The first issue is how to best handle highly-correlated nature of the d electronic states with DFT, and the second is magnetic ordering of the bulk ground state. For correlation effects, Hafner and coworkers include a Hubbard-type on-site coulomb repulsion term (the so called DFT+U approach) at the spin-polarized GGA level (GGA+U) [82] and find parameters (U=5.0 eV, J=1 eV) that lead to an acceptable compromise between the experimental cell volume, bulk band gap and cation magnetization of $Cr_2O_3$ [74]. When applied to the α-$Cr_2O_3$ (0001) surface, they obtain quantitative agreement with the experimental surface geometry determined with LEED, and are able to predict the stability of the Cr-terminated surface observed experimentally over a wide range of oxygen partial pressures [74]. However, as they note in their paper [74], because of the "empirical character of the Hubbard correction, the applicability of the DFT+U approach to the question of surface phase stability is subject to some uncertainty: it is conceivable that the optimal value of the on-site potential determined for the bulk does not apply at the surface." In this regard, we note that Chaka and coworkers others have found quantitative agreement with experimental results for surface chemistry (hydration and oxidation) on a related system, $Fe_2O_3$ (0001), without the need to invoke an on-site potential [162, 163]. As a result, we have used both approaches, DFT and DFT+U, to examine the chemistry of methylene on α-$Cr_2O_3$.

From a magnetism perspective, α-$Cr_2O_3$ is an antiferromagnetic insulator below the Néel temperature (308 K [74]), and paramagnetic at higher temperatures where most of our coupling chemistry occurs. In our simulations we can set the ordering (up or down spins) of the initial magnetic moments of the cations for the calculation to model antiferromagnetic and ferromagnetic electronic configurations. We have examined both. (One would expect the antiferromagnetic case to be the best approximation for a paramagnetic material because of the zero magnetization.) Following the work of Rohrbach et al. [74], we have examined different sequences of bulk magnetic ordering along [0001] and $[10\bar{1}2]$ directions for PBE psudopotentials within a PAW formulation of DFT, and confirmed an antiferromagnetic DFT ground state for both the standard and the DFT+U approach with (+–+–) ordering along [0001]. The (+–+–) ordering corresponds to an antiferromagnetic coupling between adjacent Cr layers along [0001]. (See ref. [74] for details.)

The computational problem associated with handling transition metal oxides surfaces of α-$Cr_2O_3$ is highlighted by our results for the binding of methylene fragments on the $(10\bar{1}2)$ surface. All of our DFT calculations predict two minima for methylene binding: (1) $sp^2$ methylene $\pi$-bonded at a Cr cation ($CH_2$=Cr),

and (2) $sp^3$-like methylene bridged bonded between a nearest neighbor surface cation and anion (Cr-$CH_2$-$O_{lattice}$). However, as illustrated in Table 1, the predicted global minimum for each type of calculation is the bridge-bonded methylene in contrast to the cation-bound methylene indicated by our XPS results. We note that while DFT has had significant success in prediction surface structures and low-energy terminations of transition metal oxide surfaces, its success in predicting small molecule binding on transition metal oxides is limited. Typical DFT-GGA calculations predicting a systematic overbinding of ~0.3-0.7 eV [158]. In an experimental and computational examination of methyl binding on α-$Fe_2O_3$ (0001) surfaces, Ellis and coworkers concluded that while the predicted strong binding of ·$CH_3$ on different Fe- and O-sites was in conflict with weak binding observed in experiment, the calculated *qualitative* pattern of binding energies for the different adsorption sites were thought to be reliable. In our case with the carbene, :$CH_2$, on α-$Cr_2O_3$ ($10\bar{1}2$) where the difference in binding modes involve a difference in hybridization of the carbon center and a difference in spin state (magnetization) of the system (see discussion to follow), even the ordering of the energetics of the different binding configurations predicted by DFT are in conflict with experiment.

**Table 1. Total energies for methylene adsorbed on an 80 atom ($10\bar{1}2$) slab. The global minimum is shown in green for each type of calculation.**

| Methylene Binding Mode | | Magnetic Ground State | | | |
|---|---|---|---|---|---|
| | | Ferromagnetic | | Antiferromagnetic | |
| | | PAW-PBE | PAW-PBE +U | PAW-PBE | PAW-PBE +U |
| 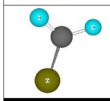 | energy (eV) | -693.522089 | -691.142685 | -695.299601 | -693.021969 |
| | \|Δmagnetization\| | 2.0000 | 2.0000 | 2.0000 | 2.0000 |
| | *energy cost for Δmag (eV)* | 0.708203 | 0.513220 | 0.544327 | 0.532273 |
| 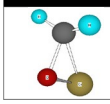 | energy (eV) | -693.847277 | -691.585390 | -695.886738 | -693.744150 |
| | \|Δmagnetization\| | 0.0000 | 0.0000 | 0.0000 | 0.0000 |
| | *energy cost for Δmag (eV)* | 0.0000 | 0.0000 | 0.0000 | 0.0000 |

One complication we note for our calculations is a difference in the net magnetization of the cell for the two methylene binding geometries. The bridged species cause no net change in magnetization of the cell, while a π-bonded methylene causes a change of 2.0 in the magnetization (in Table 1 listed as the absolute value of the difference between the number of spin up and spin down electrons) as the two electrons on the carbene pair with two of the three unpaired d electrons on the cation site. If the magnetization consistent with the π-bonded species (two fewer unpaired electrons) is imposed on the clean surface, a significant energy cost is found for the magnetization variance as shown in Table 1. In the ferromagnetic case, the change in magnetization is localized on a single cation, and is sufficient to account for the higher energy predicted for the π-bonded methylene. For the antiferromagnetic case, if a magnetization with two fewer unpaired electrons is imposed on the clean surface, the magnetization change is delocalized across the cations in the cell rather than localized on a single site as observed in the presence of methylene. The energy cost for the change in is subsequently under predicted. In all cases, if the magnetization of the system is fixed at a value consistent with π-bonded methylene, the cation-bound binding geometry is predicted to have the lowest energy. We have made use of this observation as an artificial method to reverse the ordering of the binding energies of the different sites to estimate barriers to surface diffusion of methylene.

We have examined two possible methylene diffusion routes over the α-$Cr_2O_3$ ($10\bar{1}2$) surface for a ferromagnetic electronic configuration (Figure 72). The barrier for cation-to-cation diffusion across a channel (blue arrows in Figure 72) is 0.67 eV. The potential energy surface for the minimum energy pathway is shown in Figure 73, and involves a $sp^3$-like transition state

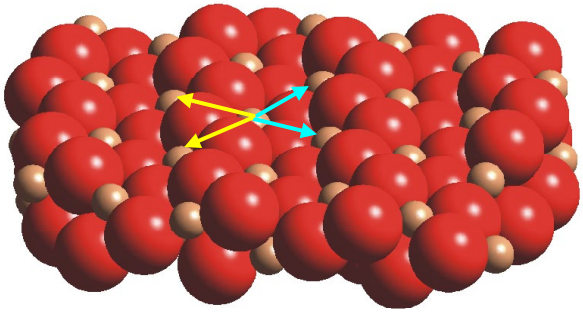

**Figure 72. Cation-to-cation migration paths for the activated diffusion of methylene fragments on stoichiometric α-$Cr_2O_3$ ($10\bar{1}2$). The "cross-channel" path is illustrated by the right-pointing blue arrows, and the oxygen-mediated path over the "zig-zag" rows of coordinately-unsaturated oxygen anion is illustrated by the left-pointing yellow arrows.**

with no predicted change in the overall system magnetization along the reaction coordinate.

For the oxygen-mediated pathway (yellow arrows in Figure 72), diffusion involves movement from cation to cation through $sp^3$-like, bridge-bonded species. A reasonable minimum energy pathway consistent with the experimentally favored cation-bound methylene is only obtained if the overall magnetization on the potential energy surface is fixed to the value corresponding to an initial π-bonded methylene. Again, for the ferromagnetic electronic configuration, the barrier for diffusion is estimated as 0.93 eV with a $sp^3$-like transition state and local bridge-bonded $sp^3$ minima along the reaction coordinate (Figure 74).

In addition to the diffusion pathways, we have also examined the coupling reaction of two surface methylene fragments to form surface ethylene. The barrier for "cross-channel" coupling of methylene on neighboring cations (not shown) is less than 0.15 eV, significantly lower than the barrier to simple diffusion.

From a computational standpoint, the situation for the (0001) surface is dramatically simpler. For all calculations (antiferromagnetic, ferromagnetic, with and without the Hubbard on-site correction), DFT predicts the proper minimum energy binding mode, a π-bonded ($sp^2$) methylene at a cation site with no constraint on the system magnetization, in agreement with our XPS results. Because of the different surface structure, only one surface diffusion pathway is found. It involves two bridge-bonded local minima: the first with methylene bridged between a nearest neighbor cation and anion, and a second more strained configuration bridged between a 2nd nearest neighbor cation-anion pair as indicated in Figure 75. The potential energy surface for the minimum energy pathway with antiferromagnetic ordering (no on-site potential) gives a barrier of 1.28 eV (Figure 76).

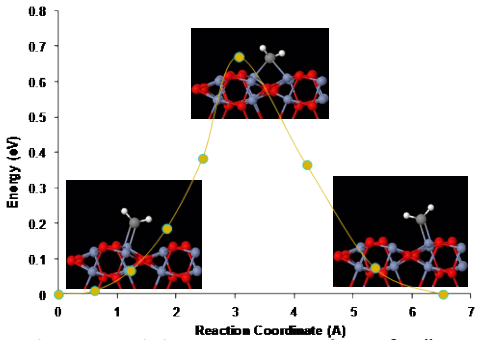


**Figure 73. Minimum energy pathway for "cross-channel" methylene diffusion.**

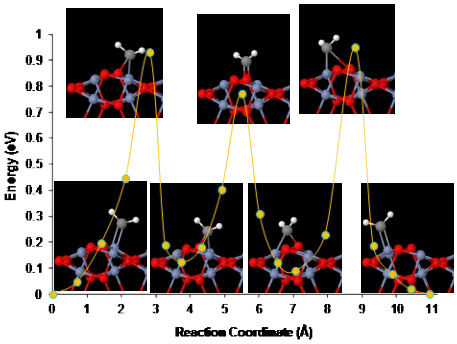


**Figure 74. Minimum energy pathway for "oxygen-mediated" methylene diffusion.**

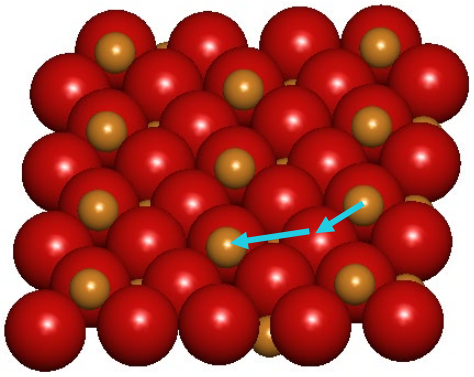

**Figure 75. Catiion to cation methylene migration pathway across α-$Cr_2O_3$ (0001)**

A comparison of the computational and experimental results is shown in Table 2. While the problems encountered for the $(10\bar{1}2)$ surface prevent an accurate estimate of the barriers for the two diffusion pathways (both are underestimated by about 130 meV), the difference in the two computed barriers match the experimentally observed difference between the two reaction-limited coupling channels observed experimentally on the $(10\bar{1}2)$ surface. For the (0001) surface the computed barrier to methylene diffusion matches the experimental value at low Cl adatom coverages to within 10 meV with no artificial constraint imposed on the system magnetization. We find that inclusion of the on-site correction (DFT+U) provides significant change in our computed results given the difficulties already encountered.

**Table 2. Experimental and computed barriers to methylene diffusion on α-$Cr_2O_3$**

| $(10\bar{1}2)$ | Experiment | Calculation |
|---|---|---|
| Low-Barrier | 0.80 eV | 0.67 eV |
| High-Barrier | 1.05 eV | 0.93 eV |
| $\Delta E_a$ | 0.25 eV | 0.26 eV |
| (0001) | Experiment | Calculation |
| | 1.29 eV | 1.28 eV |

The computational results for methylene diffusion on α-$Cr_2O_3$ surfaces explain the experimentally observed chemistry which favors diffusion and coupling over methylene dehydrogenation and carbon deposition. The mobility of surface methylene is attributed to the low barriers to $sp^2 \leftrightarrow sp^3$ rehybridizaton which allows the carbene to "walk" across the surface. The trace amounts of surface carbon left following the reaction of the carbene is likely due to some small amount of "orphaned" [164] methylene that fails to find a coupling partner. Given that the deposited halogen in these reactions eventually blocks the reactive cation sites, there are few turnovers on a given site to that might allow for the build-up of significant amounts of carbon from a low probability reaction pathway.

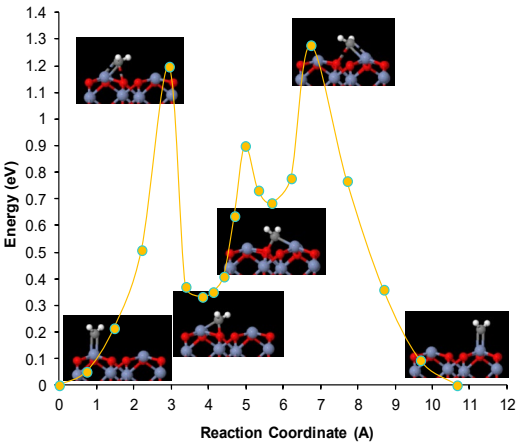


**Figure 76. Minimum energy pathway for methylene diffusion on α-$Cr_2O_3$ (0001).**

The one reaction pathway not explained by the computational study is the low-temperature (255 K) desorption-limited evolution of ethylene from the (0001) surface. We suspect this pathway is due to the coupling of two methylene fragments in the neighborhood of a single surface Cr cation. We are unable to geometry optimize two distinct methylene groups on a single cation in DFT without their spontaneous coupling to ethylene.

### 2.5.2 An attempt to selectively control the Cr cation coordination numbers on α-$Cr_2O_3$ (0001) with deposited halogen.

In this budget period we examined the reaction of $C_2$ alkyls (ethyl, ethylidene, and ethylidyne) on the α-$Cr_2O_3$ (0001) surface for comparison to results from the $Cr_2O_3$ $(10\bar{1}2)$ as part of our attempt characterize structure sensitive in hydrocarbon reactions. A wider range of coupling products was observed over the (0001) surface (presumably due to the lower coordination of the surface Cr cations), but always in small amounts. The primary reaction products were unchanged, but we saw an ~50 K increase in the reaction temperature in TPD on the (0001) surface for intermediates that react by β-hydride elimination (ethyl, $CH_3CH_2$– [165] and ethylidyne, $CH_3C\equiv$). However, the reactivity of ethylidene showed some marked differences. The primary chemistry over $Cr_2O_3$ $(10\bar{1}2)$ is ethylidene isomerization to ethylene [166] in a single reaction channel, but two distinct routes to ethylene are observed over the (0001) surface, one involving a dehydrogenation step and one isomerization. Since cations on the stoichiometric (0001) surface expose three coordination vacancies, our working hypothesis was that the reactivity differences might occur over cations sites binding different numbers of halogen adatoms, effectively altering both the coordination number and oxidation state of the metal center. At the time, we did not have a good characterization of the relationship between halogen coverage and reactivity.

We set out to try to control the coverage of surface halogen adatoms (Cl in our attempts) and to characterize the resulting metal centers with a variety of probe molecules in TPD. Ethyl chloride ($CH_3CH_2Cl$) was our halogen source of choice since it should deposit no more than one Cl adatom per reactant molecule, and it reacts cleanly giving gas phase ethylene and no surface carbon [165]. We quickly found that our reactivity for ethyl chloride and other reactant molecules shut down due to site blocking of the cations at halogen coverages approaching one adatom per cation site.

We examined the distribution of Cl on the (0001) surface using DFT. As with our examination of the diffusion of methylene, we used an antiferromagnetic bulk electronic configuration. Site coverages from one to three Cl per surface Cr cation were examined. In all cases examined, the system energy for a given Cl adatom coverage was *significantly* lower when multiply chlorinated metal sites were avoided. This effect is illustrated in Figure 77 by an examination of the diffusion of a Cl adatoms. The barrier for cation-to-cation diffusion of a single Cl adatom is 1.38 eV. The barrier for adatom diffusion from a double-chlorinated site to a neighboring vacant cation site is only 0.24 eV and is exothermic by over 1.6 eV. Doubly chlorinated cation sites, if formed, are therefore unlikely to remain intact during a thermal desorption experiment. Our model for understanding the limited occupancy for a $Cr^{3+}$ cation site with three coordination vacancies is to consider an oxidative addition of the Cl adatom which changes the cation oxidation state from 3+ to 4+ with a tetrahedral coordination geometry – one of the preferred coordination geometries for $Cr^{4+}$ (ex., $CrCl_4$) [167]. The local coordination geometry predicted by DFT is consistent with this argument (Figure 78). Details of the chemistry of ethylidene on the (0001) surface remain unsolved.

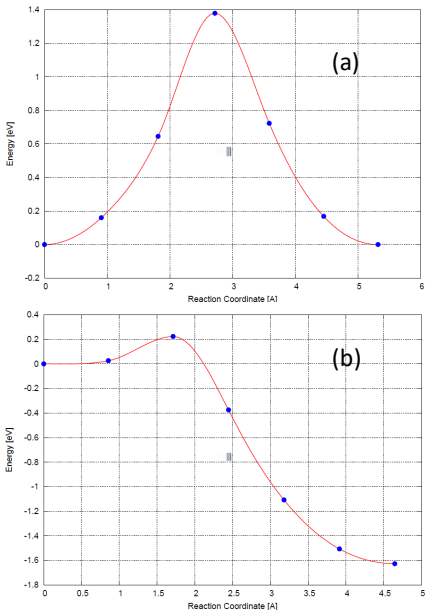


**Figure 77. Barrier to Cl adatom diffusion on α-$Cr_2O_3$ (0001). (a) cation-to-cation diffusion barrier on a clean surface, (b) Cl diffusion from a doubly-chlorinated cation to form two neighboring singly-chlorinated sites.**

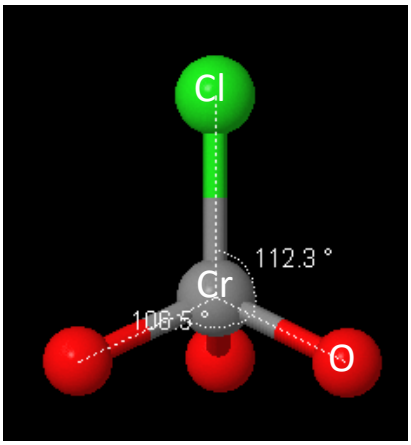


**Figure 78. DFT local coordination geometry of a chlorinated surface cation on α-$Cr_2O_3$ (0001). This subunit was culled from a full periodic slab calculation.**

## 2.5.3 Surface characterization and $C_1$ reaction studies on α-$Fe_2O_3$ $(10\bar{1}2)$

As a complement to our work on structure sensitivity in hydrocarbon reactions over α-$Cr_2O_3$ $(10\bar{1}2)$ and (0001) surfaces, we began a study of reaction chemistry over α-$Fe_2O_3$ $(10\bar{1}2)$ in the most recent project period. A structural equivalent to the α-$Cr_2O_3$ $(10\bar{1}2)$ surface, the study of chemistry over hematite ($Fe_2O_3$) should provide a direct experimental interrogation of a nearly-pure electronic effect in surface chemistry and catalysis associated with a higher d-electron density on $Fe^{3+}$ ($d^5$) compared to $Cr^{3+}$ ($d^3$) cations. Our work to date on α-$Fe_2O_3$ $(10\bar{1}2)$ has focused on surface characterization and the reactions of $C_1$ fragments methyl and methylene.

**2.5.3.1 Surface characterization of α-$Fe_2O_3$ $(10\bar{1}2)$.** We started work on the characterization of an $Fe_2O_3$ single crystal in an earlier project period, but after considerable effort determined that our crystal supplier had provided a $(11\bar{2}1)$ oriented sample rather than the $(10\bar{1}2)$ we intended to study. During the most recent project period we began working on α-$Fe_2O_3$ $(10\bar{1}2)$. Using recipes from the literature [153, 154, 168-172], we are able to produce essentially stoichiometric (1×1) surfaces by oxidation in $O_2$ at $1\times10^{-6}$ Torr at 750 K. XPS following the oxidation treatment give Fe 2p spectra characteristic of $Fe^{3+}$ in $Fe_2O_3$ with no indication of reduced $Fe^{2+}$. Heating the (1×1) surface in vacuum to 950 K produces a reconstructed (2×1) surface with reduced $Fe^{2+}$ sites [168-170] (Figure 79) The ability to readily generate an ordered, but oxygen-deficient surface on the same crystal makes an examination of the chemistry of $Fe^{2+}$ sites readily accessible. However, our understanding of the chemistry is dependent on a knowledge of the structural properties of the reduced sites.

**2.5.3.2 Preliminary STM characterization of α-$Fe_2O_3$ $(10\bar{1}2)$.** The literature includes a number of reports of STM atomic-scale imaging of α-$Fe_2O_3$ (0001) and $(11\bar{2}3)$ surfaces [173-181], but to date there are

no published reports [168, 169] of STM imaging for the $\alpha$-$Fe_2O_3$ $(10\bar{1}2)$ surface despite clear demonstrations that the (1×1) and (2×1) terminations give rise to significant differences in surface chemistry[168, 169, 171, 182]. We made a preliminary attempt at an STM characterization of the $\alpha$-$Fe_2O_3$ $(10\bar{1}2)$ surface in March 2011 during a visit to the Center for Nanophase Materials Sciences (CNMS) at Oak Ridge National Laboratory working with Dr. Minghu Pan, a CNMS staff member.

With only five days of instrument time, the work was necessarily exploratory in nature. Earlier LEED and XPS work in our laboratory provide a starting point for sample preparation. We were unable to generate a flat surface with the established oxidation procedures that produce a stoichiometric (1×1) termination. However, we were able to confirm the stoichiometric nature of the surface using scanning tunneling spectroscopy (STS) which verified the ~2 eV band gap expected for $\alpha$-$Fe_2O_3$. Cycles of gentle (500 eV) ion bombardment and vacuum annealing produced progressively flatter surfaces over a several day period, but no atomic resolution images. STS also verified the reduced nature of the (2×1) surface through a decrease in the band gap to ~ 1 eV. Following a prolonged bombardment and annealing preparation procedure, we were able to see some initial evidence of the (2×1) reconstruction on our final day (Figure 80). While the image quality is obviously very poor, it does offer some encouragement for eventual atomic-scale imaging. We hope to schedule another visit to CNMS for early 2012. On the local front, we have a new faculty member in the Physics Department at Virginia Tech, Prof. Chenggang Tao, who is awaiting delivery of a new low-temperature UHV STM. We will begin a collaboration on imaging iron oxide surfaces following the arrival of his instrument in 2012.

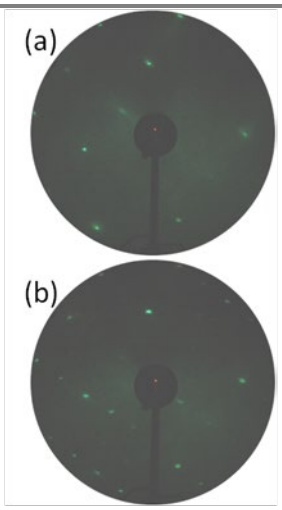


**Figure 79. LEED of $Fe_2O_3$ $(10\bar{1}2)$ for 52 eV beam energy. (a) LEED pattern after oxidation. (b)(2×1) LEED pattern after annealing in vacuum.**

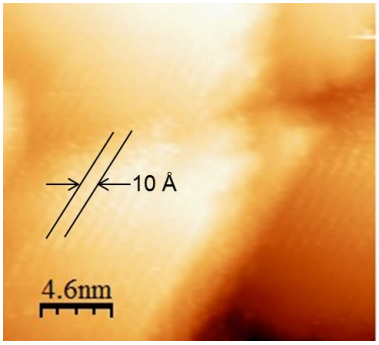


**Figure 80. STM image showing evidence of atomic scale rows with periodicity characteristic of the (2×1) $Fe_2O_3$ $(10\bar{1}2)$ surface reconstruction.**

**2.5.3.2 Experimental examination of methylene, :$CH_2$, reactions on stoichiometric and reduced α-$Fe_2O_3$ $(10\bar{1}2)$.** Variations in the $M^{3+}$ d-electron density cause dramatic but predictable changes in the surface chemistry of methylene, :$CH_2$, fragments on stoichiometric corundum-structure $(10\bar{1}2)$ surfaces when $Cr^{3+}$ cations are replaced with $Fe^{3+}$. The reaction selectivity of diiodomethane, $CH_2I_2$, on stoichiometric α-$Fe_2O_3$ $(10\bar{1}2)$ is entirely towards the nonselective oxidation products CO and $CO_2$ for small submonolayer doses of the reactant, consistent with the reducible nature of the surface. Figure 81a shows the TPD product spectrum following a 0.2 L dose on a freshly prepared, stoichiometric (1×1) $Fe_2O_3$ $(10\bar{1}2)$ surface. CO and $CO_2$ evolve simultaneously (often an indication of a carboxylate surface intermediate) at 630 K. No other products are observed, only a small amount of unreacted diiodomethane. For consecutive TPD runs, the production of CO and $CO_2$ drop off quickly with the first few doses of reactant, and formaldehyde ($H_2C$=O) and ethylene ($H_2C$=$CH_2$) appear as major products. Figure 81b shows the TPD product spectrum for the fifth consecutive 0.2 L dose.

From the products formed, it is clear that methylene fragments from $CH_2I_2$ reduce the surface via the extraction of extract lattice oxygen to make CO, $CO_2$ and $H_2C$=O. We note that in addition to this chemical reduction, our TPD temperature ramp takes the sample into a range (750 K) where the slow onset of the thermally-driven (1×1)-to-(2×1) reconstruction has been observed [170]. The TPD run in Figure 81b is similar to one from a (2×1) surface prepared by the thermally-driven reduction in vacuum.

The shift in the product slate from nonselective oxidation products (CO, $CO_2$) to selective oxidation ($H_2C{=}O$) and $H_2C{=}CH_2$ occurs as the surface becomes reduced. For methylene coupling to ethylene, the generation of reduced $Fe^{2+}$ surface sites is clearly important, although the specific site requirements (if any) for the coupling reaction are unclear because of a lack of information about the surface structure.

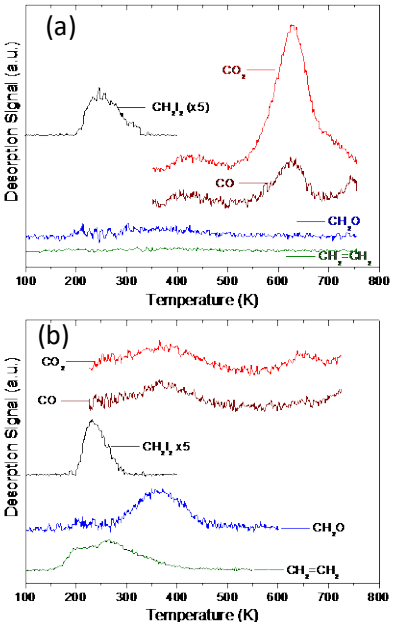


**Figure 81. Reaction of methylene on α-$Fe_2O_3$ (10$\bar{1}$2) from 0.2L doses of CH2I2. (a) First dose on a freshly-prepared (1×1) surface. (b) 5th dose.**

**2.5.3.3 Experimental examination of methyl, ·$CH_3$, reactions on stoichiometric α-$Fe_2O_3$ (10$\bar{1}$2).** The reactivity of the halomethanes $CH_3Cl$ and $CH_3I$ on α-$Fe_2O_3$ (10$\bar{1}$2) is very low. The primary reaction observed in TPD is the simple adsorption and desorption of the halomethane molecule. Our examination of this chemistry is in the early stages. We are currently exploring ways to activate the singly-halogenated reactant molecules (cleave the C-X bond) via electron-induced dissociation (see, for example, Ref. [183]) using a low-energy electron flood gun. Our work with $CH_3I$ adsorption on the two α-Cr2O3 surfaces has demonstrated that we can distinguish between surface $H_3C$-O, $H_3C$-$M^{3+}$ and $H_3C$-I by differences in the C 1s binding energies. We note, however, that a low reactivity of methyl groups with the α-$Fe_2O_3$ (0001) surface has been reported by Stair and coworkers [158, 184] for a number of different surface terminations generated by different sample pretreatments. They observe only methyl radical desorption in TPD following deposition of methyl groups by the pyrolysis of azomethane. If we are able to generate significant surface concentrations of methyl groups via electron-induced dissociation, it will be interesting to see if any methyl oxidation activity is observed similar to that seen for surface methylene, or if radical desorption (as seen on the (0001) surface) or C-X recombination with $CH_3X$ desorption occurs.

**2.5.3.4 Computational modeling of α-$Fe_2O_3$ (10$\bar{1}$2).** Our computational examination of surface chemistry on α-$Fe_2O_3$ (10$\bar{1}$2) is also in the early stages. To date, we have examined the magnetic ordering for the antiferromagnetic bulk, and have verified a ground state with ++-- ordering along [0001] in agreement with the findings of Hafner and coworkers [74, 185]. We have also generated relaxed surface structures for ferromagnetic and antiferromagnetic configuration within the DFT and DFT+U approaches. We have not yet examined any oxygen deficient surface structures.

### 2.5.4 Synchrotron work during the current project period

At the beginning of the current project period, our goal was to collect high-quality photoemission spectra for $C_2$ alkyls on α-$Cr_2O_3$ (0001) to complement our existing TPD reactivity studies from an earlier project period, then begin our studies of $C_1$ fragments on α-$Cr_2O_3$ (0001) and α-$Fe_2O_3$ (10$\bar{1}$2) in support of our current reactions studies. Our research group made five trips to the National Synchrotron Light Source during the current project period. As a result of the changes made to upgrade the U12a beam line, significant problems were encountered in the collection of data from insulating α-$Cr_2O_3$ samples. In earlier visits, the low-energy electron flood gun available at the beam line was sufficient to stabilize charging during photoemission, but the addition of a refocusing mirror at the entrance to the experimental chamber increased the photon flux to a point that spectra could no longer be collected.

During our first visit of this budget period, attempts to reduce the photon flux by narrowing the entrance and exit slits cut down the total dose received by the sample, but because of the improved focusing the flux in the illuminated area stayed high even as the spot size decreased. As a result, this first visit was spent testing a multitude of flood gun settings after the problem was first encountered. The second trip was spent trying different flood gun operating distances in conjunction with a new port alignment device with no success. We eventually resorted to defocusing the new mirror on the last afternoon of our second visit in a "last ditch effort" to collect spectra. This defocusing procedure showed promise, and was used in subsequent visits with varying success.

We eventually collected spectra for the $C_2$ compounds on $\alpha$-$Cr_2O_3$ (0001), but these data all include unusual high binding energy features in the C 1s spectra (288 eV and higher) that were traced back to an unusual level of carbon oxides in the chamber background during our third visit. Multiple extended bake outs did not help, but the rate of uptake in the absence of dosed reactant molecules was characterized. The spectra are usable for our data interpretation but not publishable.

The difficulties through our first three visits delayed our work on examining the $C_1$ compounds studied during the current project period, but we did collect a complete set of spectra for methyl and methylene fragments on $\alpha$-$Cr_2O_3$ (0001) during a shortened fourth visit and the first half of our last visit. Our first attempt at collecting photoemission and NEXAFS data for methylene on $\alpha$-$Fe_2O_3$ $(10\bar{1}2)$ ended in a sample holder failure. Frustrations aside, we have established that the conductivity of our $\alpha$-$Fe_2O_3$ single crystal sample is sufficient to utilize the full photon flux from the beam line with no need for charge stabilization.

## 2.6 Results and Accomplishments 5/1/2012 – 8/31/2016

### 2.6.1 Description of our interest in $\alpha$-$Cr_2O_3$ and $\alpha$-$Fe_2O_3$ surfaces

There are no commercial heterogeneous catalysts for the dehydrogenation of ethane, but chromia is known to catalyze a variety of selective dehydrogenation and non-selective oxidation reactions of hydrocarbons [186-214]. Supported chromia is used industrially for the catalytic dehydrogenation of propane to propene and butanes to butenes [196], and a number of investigations have focused specifically of the oxidative dehydrogenation of ethane [200, 201, 208-211, 215]. The dehydrogenation selectivity is typically a function of time on stream with the initial selectivity to alkenes being low, and CO and $CO_2$ mainly formed. After an induction period associated with the reduction of $Cr^{5+}$ and $Cr^{6+}$ species to $Cr^{3+}$, the selectivity to alkenes typically increases above 90% [14]. The active centers for alkane dehydrogenation are thought to be coordinatively-unsaturated $Cr^{3+}$ cations, and deactivation with time on stream is due to coke formation [14].

Since $Cr^{3+}$ centers are active sites for the dehydrogenation of larger alkanes, we explored the chemistry of $C_1$ and $C_2$ hydrocarbon fragments on $\alpha$-$Cr_2O_3$ single crystal surfaces exposing $Cr^{3+}$ centers for insight into the chemistry of ethane dehydrogenation over chromia. Our hypothesis was that the different intermediates formed by C-C or C-H bond activation in ethane and ethylene would control the overall selectivity in the catalytic dehydrogenation or oxidative dehydrogenation of ethane. It was our hope to identify the primary coke forming intermediates that limit the usefulness of chromia for ethane dehydrogenation. Additionally, we wished to determine any structure-function relationships in the surface chemistry, including the impact of both surface atomic structure and electronic structure on the selectivity of the surface chemistry.

Our approach was to start with two different single crystal surfaces of $\alpha$-$Cr_2O_3$, the (0001) and the $(10\bar{1}2)$, to look for any atomic structure sensitivity in the surface chemistry. The ideal, stoichiometric $(10\bar{1}2)$ surface is nonpolar and breaks the minimum number of cation/anion bonds (Figure 82a). The topmost atomic layer of the ideal surface is composed of oxygen anions. All $O^{2-}$ anions in the top atomic layer are three-coordinate, and the $Cr^{3+}$ cations in the second atomic layer are five-coordinate. Both ions have one degree of coordinative unsaturation relative to their bulk counterparts [153], making this the simplest corundum surface from a coordination chemistry perspective. The ideal (0001) surface (Figure 82b) is non-polar and terminated with a layer of 3-coordinated $Cr^{3+}$ cations (3 coordination vacancies) at a coverage 1/3 that of the layer of underlying $O^{2-}$ anions [216]. All the oxygen anions in the second atomic layer are 3-coordinated with one degree of coordinative unsaturation relative to the bulk. Based on the crystal structure, the nearest $Cr^{3+}$-$Cr^{3+}$ separations of surface cations are 3.65 Å and 4.96 Å on the $(10\bar{1}2)$ and (0001) surfaces, respectively. In the absence of a high density of surface steps and point defects, the metal cation centers can be thought of as *isolated* reaction sites for small $C_1$ and $C_2$ *hydrocarbon fragments, with significant differences in local coordination. These two surfaces provide an experimental basis for the investigation of the effects of atomic structure and cation coordination on the surface chemistry.*

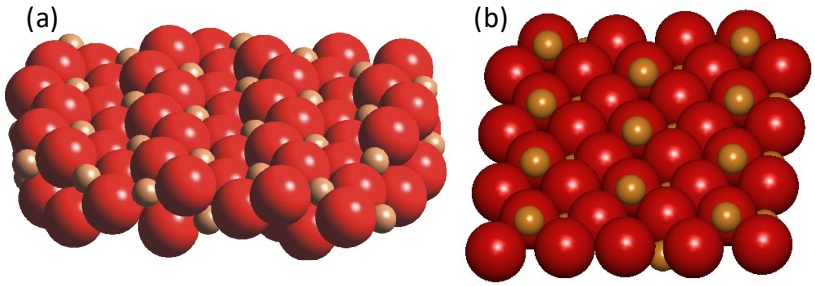


**Figure 82. Ball model illustration of the ideal, stoichiometric (a) $\alpha$-$Cr_2O_3$ $(10\bar{1}2)$ and (b) (0001) surfaces assuming no relaxation. The small gold spheres represent $Cr^{3+}$ cations while the large red spheres represent $O^{2-}$ anions.**

To independently examine electronic effects, we have studied reactivity over the $\alpha$-$Cr_2O_3$ $(10\bar{1}2)$ and $\alpha$-$Fe_2O_3$ $(10\bar{1}2)$ surfaces. Both $\alpha$-$Cr_2O_3$ (escolite) and $\alpha$-$Fe_2O_3$ (hematite) have the corundum bulk structure [216]. Given that the lattice parameters for the two materials vary by less than 1.4%, the substitution of $\alpha$-$Fe_2O_3$ for $\alpha$-$Cr_2O_3$ gives $M^{3+}$ cations (M ≡ Cr, Fe) in essentially identical structural environments in the two materials. While the formal oxidation state of the cations is 3+ in both materials, the cation electronic configurations are different: $3d^3$ for $Cr^{3+}$ and $3d^5$ for $Fe^{3+}$. Hence, differences in the surface chemistry between $\alpha$-$Cr_2O_3$ $(10\bar{1}2)$ and $\alpha$-$Fe_2O_3$ $(10\bar{1}2)$ can be attributed to an essentially pure electronic effect related to the different d electronic configurations of the different cation types. Work completed early in the previous project period has allowed us to make comparisons addressing both structural and electronic effects in the chemistry under study.

We have found that nearly-stoichiometric $\alpha$-$Cr_2O_3$ $(10\bar{1}2)$ surfaces can be prepared via ion bombardment and annealing in vacuum to 950 K [134]. A nearly-stoichiometric $\alpha$-$Cr_2O_3$ (0001) surface can also be prepared in UHV [130, 137, 217]. For hematite, we have had success preparing stoichiometric (1x1) and oxygen-deficient (2x1) $Fe_2O_3$ $(10\bar{1}2)$ surfaces using recipes available in the literature [154, 170].

### 2.6.2 Overview of chemistry on $\alpha$-$Cr_2O_3$

The reactivity patterns (product slates) for different hydrocarbon fragments are similar on both $(10\bar{1}2)$ and (0001) surfaces of $\alpha$-$Cr_2O_3$, although some variations in selectivity and kinetics are observed. Generally speaking, the principle reactivity patterns summarized in Figure 83 for $\alpha$-$Cr_2O_3$ $(10\bar{1}2)$ are also observed for $\alpha$-$Cr_2O_3$ (0001) [29, 66, 127, 217-222].

An interconnection between the $C_1$ and $C_2$ hydrocarbon intermediates in Figure 83 occurs through a set of hydrogenation, dehydrogenation and coupling (C-C bond formation) reactions. Note that not all the hydrogenation reactions observed in our studies are listed in Figure 83. Methylene hydrogenation to methyl, methyl hydrogenation to methane, ethyl hydrogenation to ethane and vinyl hydrogenation to ethylene are also observed. The hydrogenation of vinylidene and ethylidene were not specifically examined.

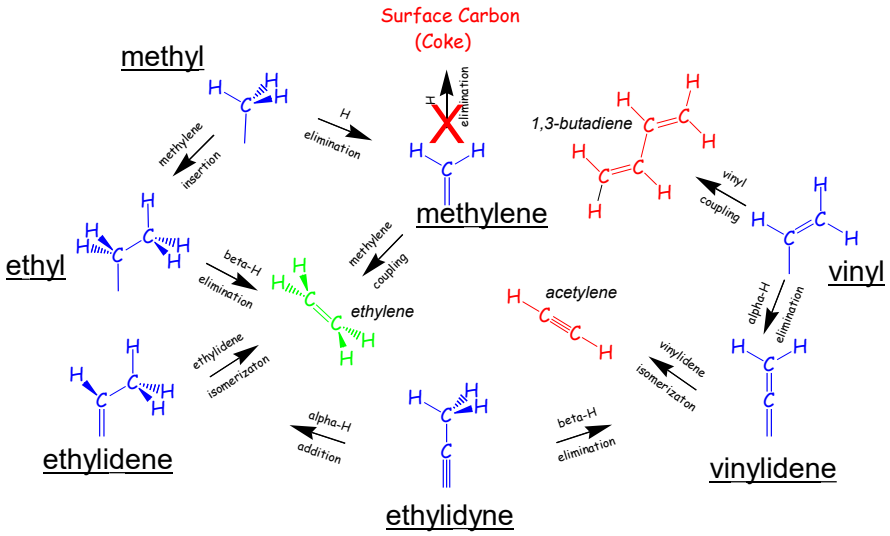


**Figure 83. Primary reaction pathways of $C_1$ and $C_2$ hydrocarbon fragments on α-$Cr_2O_3$ ($10\bar{1}2$). Ethylene (green) is the selective product for ethane dehydrogenation, while the other molecular products (red) are nonselective products.**

In TPD the primary reaction pathways of all the $C_1$ and $C_2$ hydrocarbon fragments yield $C_2$ compounds (or larger in the case of vinyl) as gas phase products. Additionally, only trace surface carbon (coke) deposition is observed within the detection limits of XPS and AES for any of the fragments investigated – even the $C_1$ fragments of methyl and methylene; methyl dehydrogenates to methylene, but methylene couples to form $C_2$ products. None of the fragments investigated are significant coke formers on our α-$Cr_2O_3$ surfaces under the conditions of our TPD experiments. These observations suggest the coke forming reactions on working chromia catalysts have higher activation barriers than those observed in UHV over our model catalysts, and are operable under conditions of higher temperature (required for the initial ethane activation step) and higher pressure where some reactant is always available to the surface.

Interesting among the observations is that the principle reaction of both $C_2$ carbenes is an intramolecular isomerization reaction (ethylidene to ethylene, and vinylidene to acetylene.) The $C_1$ carbene methylene, rather than dehydrogenating to surface carbon, can couple directly to give ethylene, react with surface methyl (insertion into the methyl C-surface bond) to form an ethyl fragment or hydrogenate to methane. These coupling reactions, along with the coupling of vinyl to 1,3-butadiene are most interesting, particularly on α-$Cr_2O_3$ ($10\bar{1}2$) where a nearly-stoichiometric surface should expose cations primarily with a single coordination vacancy. While there are reports of coupling reactions on oxide surfaces where the binding sites of two ligands are in close proximity [164, 223], one typically associates coupling reactions with the availability of multiple coordination sites on a single cation, per arguments advanced by Barteau [3]. In the case of α-$Cr_2O_3$ ($10\bar{1}2$) and (0001) surfaces where the cation sites are widely separated, lateral interactions leading to coupling between small methylene fragments on adjacent cation sites seems unlikely. (We note that XPS indicates that all the intermediates in Figure 83 bind preferentially to cation sites, with the exception of methyl which gives a signature consistent for binding at both cation and anion sites [219].) We have described a rate-limiting surface diffusion model to explain the observed chemistry of methylene coupling [217].

### 2.6.3 Examination of atomic structure sensitivity on α-$Cr_2O_3$

The $C_1$ fragments of methyl and methylene (Figure 83) exhibit the all the primary reaction pathways (dehydrogenation, hydrogenation and coupling) seen for the other fragments, with the exception of the intramolecular isomerization observed for the two $C_2$ carbenes. This makes these two small fragments ideal candidates for the investigation of structure sensitivity (atomic and electronic) in these major reaction pathways.

**2.6.3.1 Methylene diffusion and coupling on α-$Cr_2O_3$ ($10\bar{1}2$) and (0001).** A rate-limiting surface diffusion process has been observed on both $Cr_2O_3$ surfaces that leads to methylene coupling to ethylene (2 $CH_2$= → $CH_2$=$CH_2$) [217, 218, 222] or the insertion of methylene into a methyl-surface bond to form a surface ethyl fragment [218, 219, 222]. The mobility of surface methylene groups is key to both processes. XPS gives a signature characteristic of methylene bound at a surface cation sites [217, 218, 222], implying a metal-bound methylene π-bonded to a Cr cation with an $sp^2$ hybridized carbon center.

DFT provides insight into the surface diffusion process. A thermally driven rehybridization from $sp^2$ to $sp^3$ allows the methylene to bridge from the cation site to a neighboring O anion. A sequence of these rehybridization processes ($sp^2$ → $sp^3$ → $sp^2$ → etc.) gives a "walking" appearance to the methylene group where the two bonds act as "legs" to propel the intermediate across the surface [217]. The bridging structures tend to be local (but not global) minima along the potential energy surface on α-$Cr_2O_3$ (0001). Figure 84 illustrates an initial "step" for methylene diffusion across α-$Cr_2O_3$ (0001). The full potential energy surface for diffusion on this surface is described in Ref. [217].

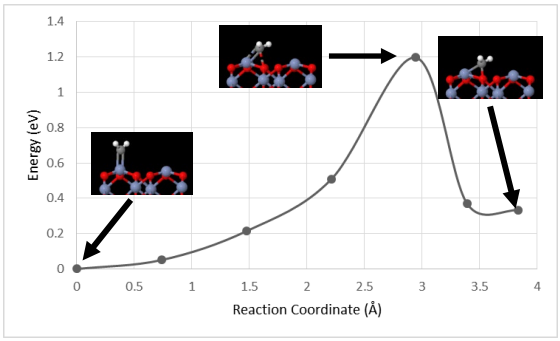


**Figure 84. A methylene "step" in the surface diffusion process on α-$Cr_2O_3$(0001). The process is a thermally driven rehybridization of the carbon center from $sp^2$ to $sp^3$.**

While a similar rehybridization process drives the diffusion of methylene across both α-$Cr_2O_3$ surfaces, significant differences are observed in the activation barriers for diffusion because of the difference in surface atomic structure and varying separations between neighboring cations. Figure 85 shows ethylene production from both surfaces in TPD. The primary feature in both TPD traces is reaction limited with surface diffusion as the rate limiting step. The barrier to surface diffusion is greater by nearly 20 kJ/mol on the (0001) surface, primarily because of the larger separation between neighboring cations.

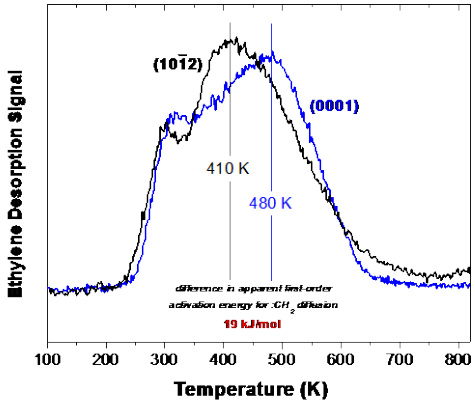


**Figure 85. Variations in the activation energy for the rate limiting diffusion of methylene on α-$Cr_2O_3$ (0001) and ($10\bar{1}2$).**

We note that there are significant difficulties with the DFT calculations for α-$Cr_2O_3$ surface chemistry, and the choice of calculation type is non-trivial. For example, XPS clearly shows that a cation-bound methylene species is the preferred binding configuration on both surfaces. For α-$Cr_2O_3$ (0001), DFT(PBE) predicts the correct low energy binding site, but DFT+U favors a bridged configuration with an adjacent O atom. For α-$Cr_2O_3$ ($10\bar{1}2$), both DFT and DFT+U both predict a bridged site as the preferred binding configuration. Those important problems aside, we note that DFT has still proven extremely useful for understanding processes like surface diffusion.

**2.6.3.2 Methyl dehydrogenation α-$Cr_2O_3$ ($10\bar{1}2$) and (0001).** While a significant effect of surface structure is observed for the diffusion-limited coupling of methylene, little impact of surface structure is observed for the dehydrogenation of methyl fragments. Figure 86 shows a comparison of the methane production in TPD for methyl fragments on both $Cr_2O_3$ surfaces. Methyl dehydrogenation is the rate limiting step on both surfaces. The difference in peak temperatures is small, and accounts for only about 5 kJ/mol difference in the barrier to dehydrogenation. We have made a similar observation for the dehydrogenation of ethyl fragments where ethane is produced via a rate-limiting dehydrogenation (β-hydride elimination) reaction, and is observed at 455 K in TPD on the (0001) surface [218], and 465 K on the ($10\bar{1}2$) surface [127, 220], indicating little variation in the barrier to dehydrogenation with surface structure.

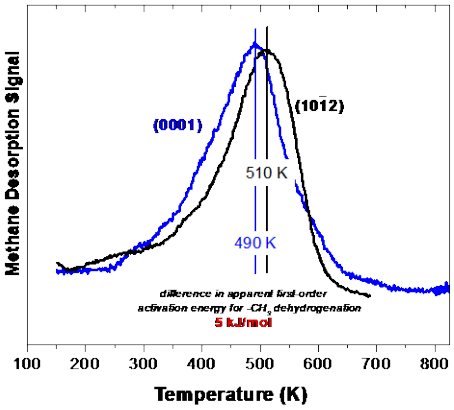


Figure 86. Variation in activation energy for methyl dehydrogenation over α-$Cr_2O_3$ (0001) and (10$\bar{1}$2).

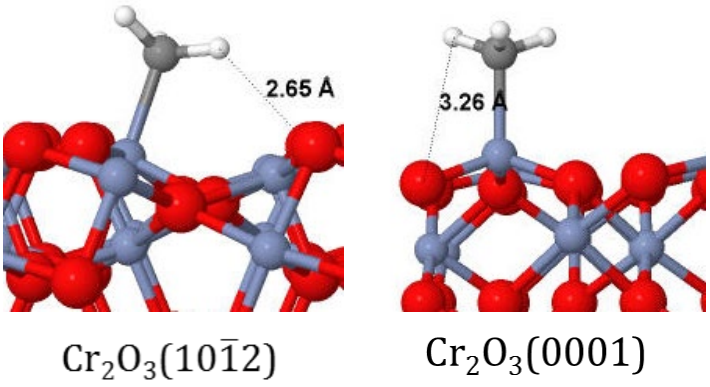


Figure 87. DFT predictions of methyl adsorption geometries on α-$Cr_2O_3$ (0001) and (10$\bar{1}$2).

These are surprising results for dehydrogenation, a process often thought of in terms of an "H extraction" facilitated by the attack of surface lattice oxygen on the H atom. Figure 87 shows DFT-derived structures for methyl fragments on both surfaces. The atomic structure of the (10$\bar{1}$2) surface lends itself to a significantly closer approach of a methyl hydrogen to a surface $O^{2-}$ anion which one might expect to lower the barrier to dehydrogenation, however, no significant effect of surface structure is observed experimentally. The results suggest a simple thermal decomposition of methyl fragments rather than a surface $O^{2-}$ anion-assisted process.

### 2.6.4 Electronic effects: Impact of cation d electronic configuration

A comparison of the reaction chemistry over isostructural α-$Cr_2O_3$ (10$\bar{1}$2) and α-$Fe_2O_3$ (10$\bar{1}$2) surfaces illustrates the impact of a change in cation electronic structure from $3d^3$ to $3d^5$ on reaction selectivity with the cation formal oxidation state fixed at 3+. The reaction of methylene fragments provides a good comparison. Over either the (10$\bar{1}$2) or (0001) surfaces of α-$Cr_2O_3$, methylene coupling to ethylene is the principle reaction, with some methane formed in the presence of additional surface hydrogen [217, 218, 222]. The $Cr_2O_3$ surfaces are essentially non-reducible, and no oxygenated products are formed. For stoichiometric α-$Fe_2O_3$ (10$\bar{1}$2), a first small dose of $CH_2I_2$ to form surface methylene fragments yields primarily $CO_2$, CO and $H_2O$ in TPD with a small amount of formaldehyde, $H_2C{=}O$ [218]. The origin of the oxygen incorporated in the reaction products is surface lattice oxygen, with an accompanying reduction of the iron oxide surface. For consecutive doses and TPD runs, the reaction selectivity shifts away from carbon oxides to formaldehyde with increasing surface reduction, and eventually to ethylene when the surface reduction is sufficient [218]. Figure 88 illustrates this difference by showing the reaction products for a first 0.2 L dose of $CH_2I_2$ (used to generate surface methylene by dissociative adsorption) on the stoichiometric α-$Fe_2O_3$ (10$\bar{1}$2) surface and the fifth dose in a sequence after significant surface reduction.

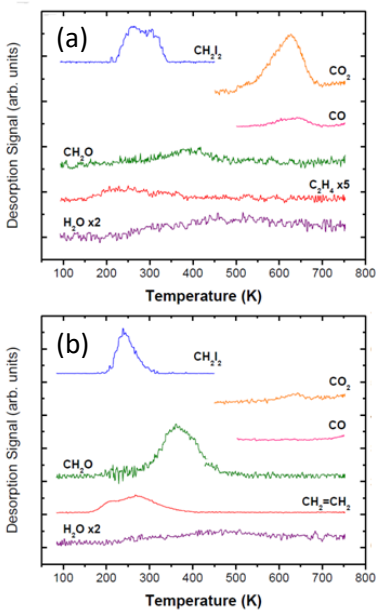


Figure 88. TPD of methylene on α-$Fe_2O_3$(10$\bar{1}$2) from 0.2 L doses of $CH_2I_2$. (a) First dose on a freshly prepared stoichiometric surface, and (b) the 5th dose in a sequence after significant surface reduction.

The CO and $CO_2$ production observed on the iron oxide originates from a formate surface intermediate ($HCOO^-$), and indicates nucleophilic attack by two surface O anions on a methylene carbon on the stoichiometric surface [218]. As the surface lattice oxygen is depleted, the selectivity shifts to formaldehyde and then to the coupling product. The ethylene product appears at low temperature (primarily below 300

K) in TPD, more characteristic of methylene coupling on metal surfaces [69, 224-226] than the diffusion limited production observed on the $Cr_2O_3$ surfaces (400 K and above).

We have completed the TPD reaction studies, but have not yet completed an XPS investigation to determine the extent of reduction of the iron oxide surface as a result of methylene oxidation. However, it is clear from these preliminary data that that the electronic differences between $Fe^{3+}(3d^5)$ and $Cr^{3+}$ $(3d^3)$ drive dramatic shifts in selectivity not seen by the perturbation of the atomic structure alone on α-$Cr_2O_3$ where variations in the kinetics of product formation may be found, but not wholesale shifts in the product slate. The selectivity difference can be partly understood from a simplistic crystal field perspective for the octahedrally-coordinated metal cation centers. For the $3d^3$ ($Cr^{3+}$) configuration, all three d electrons fill bonding $t_{2g}$ orbitals, but for the $3d^5$ ($Fe^{3+}$) high spin configuration in α-$Fe_2O_3$, the two additional d electrons fill antibonding $e_g$ orbitals. The resulting iron oxide is much more reducible, resulting in redox chemistry with the formation of oxygenated products.

### 2.6.5 Model Manganese oxide-based water splitting catalysts: *a change in direction in the last project period*

Because changes in cation electronic properties lead to a much more dramatic change in selectivity than changes in surface geometric structure (described above), in the previous project period we intended to examine the reactivity of $Mn_2O_3$ which has a $Mn^{3+}$ cation d electronic configuration of $3d^4$, intermediate between the $3d^3$ and $3d^5$ configurations of $Cr^{3+}$ and $Fe^{3+}$. Unlike many other transition metal sesquioxides, $Mn_2O_3$ does not crystallize with the corundum structure; hence we cannot match the structure of α-$Cr_2O_3$ and α-$Fe_2O_3$. However, this is considered of secondary importance given the result observed for α-$Cr_2O_3$ and α-$Fe_2O_3$. Since single crystal $Mn_2O_3$ (in either the α or γ forms) is not commercially available, our plan was to generate $Mn_2O_3$ via oxidation of a well-ordered MnO (100) single crystal surface. Our expectation was more selective oxidation chemistry, with oxygen insertion leading primarily to hydrocarbon oxygenates rather than the $CO_2$ observed from stoichiometric $Fe_2O_3$ or the non-oxygenated products observed from non-reducible $Cr_2O_3$. Our hope was to establish a clear relationship between selectivity and d electronic configuration.

However, near the beginning of the project period, the Davis group at Caltech reported a low-temperature (850°C) catalyst for the thermochemical splitting of water that consists of only non-toxic, non-corrosive reagents based on a mixture of manganese oxide and $Na_2CO_3$ [227]. (A later report from this group also shows this system has activity for $CO_2$ reduction [228].) Our belief was that we could generate a surface science model of this complex reaction system to test the details of water splitting, so we changed direction in the last project period to examine this system. The first publication from this study is available [229].

Figure 89, shows the four steps in the catalytic cycle proposed by Xu *et al.* from the Davis group [227]:

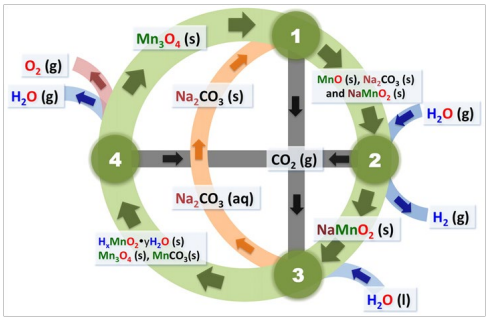


**Figure 89. Thermochemical water splitting cycle of Xu et al. Hydrogen evolution occrs from the reaction of water on with a mixture of MnO and $Na_2CO_3$. Shuttling of Na into an out of manganese oxides contributes to the catalytic cycle. Figure reproduced from Figure 2, Ref. 227.**

*Step 1: Thermal treatment of the $Na_2CO_3/Mn_3O_4$ mixture at 850°C.* $Na_2CO_3$ reacts with $Mn_3O_4$ ($Mn^{2+}$ and $Mn^{3+}$) at 500-850 °C to form $NaMnO_2$ ($Mn^{3+}$), MnO ($Mn^{2+}$) and release $CO_2$.

*Step 2: Hydrogen evolution on the $Na_2CO_3$/MnO mixture at 850°C.* In the presence of water, $Na_2CO_3$ reacts with MnO ($Mn^{2+}$) to form α-$NaMnO_2$ ($Mn^{3+}$) and release $CO_2$, while water splits to produce hydrogen. $Na^+$ in $Na_2CO_3$ is thought to enable the oxidation of Mn from 2+ to 3+ by water. *This is the key step for hydrogen evolution and draws our primary interest.*

*Step 3: $Na^+$ extraction from α-$NaMnO_2$ by aqueous $CO_2$ at 80°C.* Water intercalates into the layered α-$NaMnO_2$ and expands the distance between $MnO_6$ octahedral sheets to greatly enhance the mobility of $Na^+$ sandwiched between the adjacent manganese oxide layers. $CO_2$ is bubbled through the α-$NaMnO_2$ aqueous suspension to extract $Na^+$ and form $Na_2CO_3$, while the proton from water occupies the

position for $Na^+$ and forms $H^+$ birnessite ($H_xMnO_2{\cdot}yH_2O$) ($Mn^{3+}$).

*Step 4: Oxygen evolution by thermal reduction of solids following $Na^+$ extraction at 850°C.* After the $Na^+$ extraction from α-$NaMnO_2$, the resulting $H^+$ birnessite compound ($Mn^{3+}$) is less thermally stable and is reduced to the reactant $Mn_3O_4$ ($Mn^{2+}$ and $Mn^{3+}$) in step 1 by heating at 850 °C (1123 K) which closes the cycle. The temperature for the reduction of Mn from 3+ to 2+ is much lower than the temperature over 2000 K for the reduction of metal oxides in high temperature 2-step water splitting cycles.

**2.6.5.1 Generation of different Manganese oxides on MnO(100).** Using variants of recipes available in the literature [230, 231], we are able to generate $Mn_3O_4$ and $Mn_2O_3$ surface compounds on MnO(100) via oxidation with $O_2$ as verified by XPS [232]. Additionally we have established a method for generating a $NaMnO_2$-like surface compound on MnO(100) via oxidation of a multilayer coverage of pre-deposited Na [232]. None of these thin-film surface compounds formed on MnO(100) exhibit any long range order in LEED. Hence, these are not well-ordered surfaces. TPD of water adsorbed at 125 K on MnO(100), $Mn_3O_4$, $Mn_2O_3$ and $NaMnO_2$ desorbs below 250 K, suggesting that water is primarily molecularly adsorbed. *(A low intensity tail in the TPD spectra above 300 K can be attributed to the recombination of dissociated water for all surfaces. For MnO(100), these features due to dissociated water recombination are clearly associated with surface defects rather than flat (100) terraces.)* The primary water TPD features appear to correlate well with oxidation state of the surface Mn atoms: 190 K for $Mn^{3+}$ and 235 K for $Mn^{2+}$ [232]. As expected, none of the individual compounds produces $H_2$ from water, in agreement with the result of Xu *et al*. [227].

The coadsorption of $CO_2$ and water was also examined on MnO(100) and $NaMnO_2$ since both compounds are present in the water splitting step (2) of the catalytic cycle, and also because the interaction of $CO_2$ and water with $NaMnO_2$ provides an important reaction for regenerating $Na_2CO_3$ and $Mn_3O_4$ via the removal of Na from $NaMnO_2$ in step (3). $CO_2$ interacts weakly with clean MnO(100) terraces, but binds more strongly to as-yet-unidentified surface defects (green trace in Figure 89) [232]. Preliminary DFT(PBE)+U [54-56, 77, 233-235] calculations in our group that include van der Waals corrections (DFT-D3 [236]) give an adsorption energy of 8.16 kcal·mol$^{-1}$ for a $CO_2$ molecule on a flat terrace. This value matches well with the experimental activation energy of desorption of 9.1 kcal·mol$^{-1}$ observed for the 150 K desorption feature attributed to molecular $CO_2$ on terrace sites. Utilizing a surface step to represent a surface defect, DFT+U gives an adsorption energy of 27.95 kcal·mol$^{-1}$ for molecular $CO_2$ adsorption at a step edge. This value is significantly greater than the activation energy of desorption of 17.4 kcal·mol$^{-1}$ attributed to $CO_2$ desorption from surface defect sites, but it does indicate the likelihood that higher temperature desorption features can reasonably be attributed to surface defects. DFT work is continuing to test additional types of defect sites (ex., point defects). We note that the use of DFT+U is critical for this work. DFT(PBE) alone predicts an unrealistic surface reconstruction for weakly adsorbed $CO_2$ molecules at very low (0.03 ML) coverage, similar to problems reported for adsorbed Na [229].

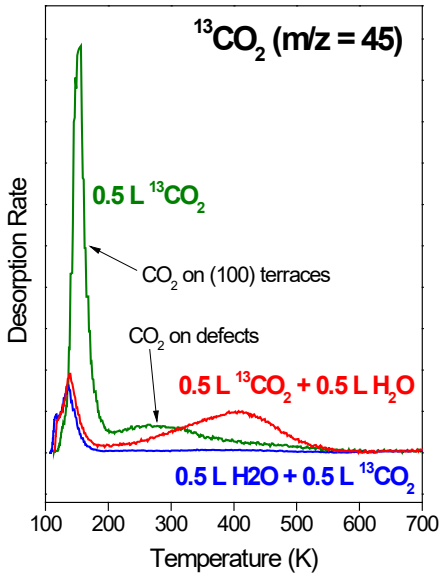


**Figure 90. MnO(100). TPD of $CO_2$ and $H_2O/CO_2$ combinations with different dosing orders. See text for details**

The interaction of water and $CO_2$ on MnO(100) is dependent on the order of dose. Pre-adsorbed water blocks the uptake of $CO_2$ on MnO(100) (blue trace in Figure 90), but water stabilizes preadsorbed $CO_2$ as bicarbonate at surface defect sites and displaces $CO_2$ from terraces (red trace in Figure 90). A careful examination of the different dosing orders as a function of dose size of both molecules (not shown) leads to the assignment of $CO_2$ stabilization at surface defects [232]. This process was confirmed with DFT.

No significant interaction is observed between $CO_2$ and water on the $NaMnO_2$ mixed oxide surface (not shown). Preadsorbed water blocks the uptake of $CO_2$, and post-dosed water displaces preadsorbed $CO_2$. No insight was gained about the process of Na extraction from $NaMnO_2$ by aqueous $CO_2$,

but the conditions of our study (liquid nitrogen temperatures in UHV) are far removed from those of step (3) in the catalytic cycle.

**2.6.5.2 Deposition of Na on MnO(100).** Na deposition on MnO(100) has been investigated by temperature programmed desorption (TPD), x-ray photoelectron spectroscopy (XPS) and low energy electron diffraction (LEED) [229, 232]. Na TPD and XPS measurements indicate that adsorbed Na interacts strongly with the MnO substrate to form an irreversibly-adsorbed, oxidic Na species on the surface for coverages up to 1 monolayer (ML). This strongly-bound Na diffuses into the MnO subsurface and bulk at elevated temperatures above 500 K. For Na coverages above 1 ML, metallic Na is present and desorbs from the surface below 500 K. The deposition of Na on MnO(100) follows a Stranski-Krastanov (SK) growth mode, with the formation of metallic Na islands following completion of the first Na monolayer. (We note that metallic and oxidic Na are easily distinguished in XPS because of strong plasmon loss features in the Na 1s and Na KLL spectra ([229]and references therein). After heating a Na covered surface to 1000 K, a (2×2) LEED pattern is observed, indicating that a surface reconstruction is induced by the diffusion of Na into the near surface region. DFT predicts an O-anion binding site for Na in the first monolayer, with significant charge transfer to the surface characteristic of an oxidic species.

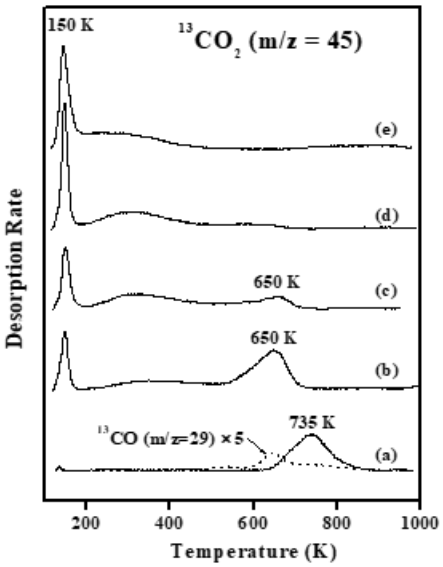


**Figure 91. $CO_2$ TPD from: (a) metallic Na islands and (b) oxidic Na in the first ML. (c) and (d) illustrate the effect of heating oxidic Na to 600 K to drive diffusion into the bulk, and (e) shows the effect of heating oxidic Na to 1000K where no Na remains on the surface and accessible to $CO_2$. In all cases, Na is still observed in XPS (see Figure 92)**

The interaction of the $CO_2$ with the different forms of Na has been examined in detail with TPD (Figure 91) and XPS (Figure 92). $CO_2$ interacts most strongly with the metallic Na islands, desorbing at 735 K in TPD (Figure 92a). In addition, a small percentage of the $CO_2$ adsorbed on metallic Na is reduced to CO via a disproportionation reaction that produces $Na_2CO_3$ ($2NaCO_2 \rightarrow Na_2CO_3 + CO$). Na interacts less strongly with irreversibly adsorbed oxidic Na in the first monolayer, desorbing at 650 K in TPD (Figure 92b). Heating a surface with oxidic Na to 600 K briefly (Figure 91c) or for 10 min (Figure 91d) drives the Na subsurface so that it is no longer sampled by $CO_2$ adsorption. Heating further to 1000 K (Figure 91e) gives a $CO_2$ trace identical to that for clean MnO(100), although Na is still clearly visible in XPS (Figure 92).

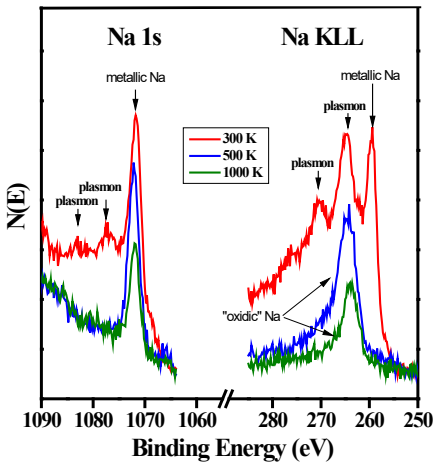


**Figure 92. XPS showing metallic island for a 2.4 ML Na coverage (300 K), and the effect of heating. Heating to 500 K sublimates metallic Na from the surface, leaving oxidic Na in the first ML. Heating to 1000 K drives Na in the first ML subsurface (see Figure 10e) and unavailable for $CO_2$ adsorption.**

Figure 92 shows the XPS Na signals for a 2.4 ML coverage of Na that shows signal characteristics of metallic Na (red "300 K" spectra) which interacts with $CO_2$ as shown in Figure 91a. Heating a metallic Na-covered surface to 500 K sublimates the metallic Na from the surface leaving irreversibly adsorbed oxidic Na with the $CO_2$ behavior shown in Figure 91b. Heating oxidic Na to 1000 K (green spectra in Figure 92) drives Na subsurface giving the TPD behavior in Figure 91e; no Na desorption is observed in TPD by this treatment. XPS shows a decrease in the Na signal due to diffusion into the bulk, but near-surface Na is still visible in XPS although not accessible to $CO_2$. The results indicate that $CO_2$ can be used as a probe molecule in TPD to distinguish between metallic Na islands and oxidic Na in the first ML, and to indicate when Na still observable by XPS goes subsurface and is not available as an adsorption site.

**2.6.5.3 Oxidation of Metallic Na islands on MnO(100) and $Na_2CO_3$ formation.** The interaction of $O_2$

with metallic Na islands on MnO(100) was investigated by XPS and TPD [232]. Exposure to $O_2$ at 350 K completely oxidizes the metallic Na islands to produce a mixture of $Na_2O$ and $Na_2O_2$. Flashing oxidized Na to 750 K gives $Na_2O$ as the primary Na species on MnO(100) as demonstrated by XPS (not shown). Further heating to 850 K causes a solid state reaction between $Na_2O$ and the MnO(100) substrate to form a $NaMnO_2$-like surface compound which decomposes primarily via diffusion of Na into the MnO bulk, above 850 K.

Treating a $Na_2O/Na_2O_2$ mixture with $CO_2$ gives rise to oxygen exchange between $CO_2$ and $Na_2O$ in TPD using $^{18}O$-labeled $CO_2$. Oxygen exchange is characteristic of $Na_2CO_3$ formation [237-240] via the reaction of $CO_2$ with, in our case, sodium oxides on MnO(100). The $Na_2CO_3$ gives $CO_2$ desorption temperatures (carbonate decomposition) near 720 K from $Na_2O_2$ and 800 K (the highest $CO_2$ desorption temperature observed in our study) from $Na_2O$ [232]. Because of the thermal stability of the $Na_2CO_3$, the surface thus formed can be treated by heating to 600 K (10 min) to drive oxidic Na in the first monolayer into the MnO subsurface, leaving the more stable $Na_2CO_3$ islands intact. This synthetic procedure produces a surface exposing islands of $Na_2CO_3$ on MnO(100), which is our model for the complex mixed MnO-$Na_2CO_3$ system thought to be active for thermochemical water splitting [227]. Figure 93 shows a cartoon of the synthetic procedure and the result of a $CO_2$ TPD run from the resulting model surface. It shows characteristics of $CO_2$ desorption from MnO(100) terraces and defect sites, and $CO_2$ desorption from the decomposition of the $Na_2CO_3$ formed on $Na_2O_2$ and $Na_2O$ (720 and 800 K, respectively), confirming the successful synthesis of our model system.

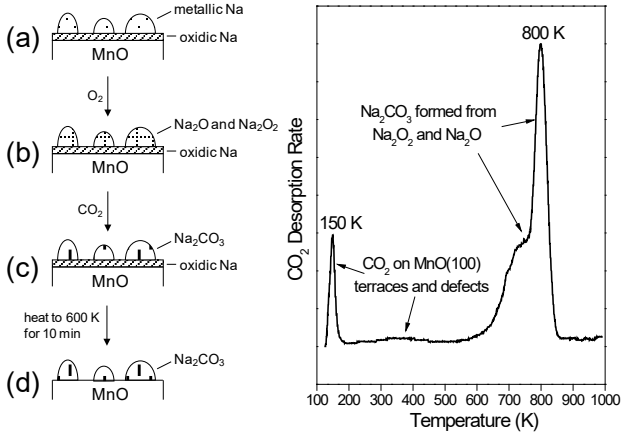


**Figure 93. Synthetic procedure for the model catalytic surface exposing $Na_2CO_3$ islands on MnO(100), and a corroborating $CO_2$ TPD characterization.**

**2.6.5.4 Tests for water splitting on the model catalytic surfaces.** The interaction of water has been examined with all the forms of Na (metallic Na and oxidic Na in the first ML), sodium oxides ($Na_2O_2$ and $Na_2O$), and the model supported $Na_2CO_3$/MnO(100) described above. Under the conditions of our TPD studies, *$D_2$ production from $D_2O$ is only observed in the presence of metallic Na.* While the production of hydrogen from the interaction of water with metallic Na is not surprising, we note that our model for the mixed $Na_2CO_3$/MnO system does not produce hydrogen from water under the conditions of our TPD investigation. In the thermochemical water splitting cycle of Xu *et al.* [227], the shuttling of Na into and out of the manganese oxides is thought to be a key driving force for the $Mn^{2+}/Mn^{3+}$ redox and the accompanying hydrogen and oxygen evolution from water. We see two possible explanations for the differences in our observations.

A first explanation is that at the working temperature of 850 °C (1123 K) for the water splitting catalysis [227], a metallic form of Na is generated by the movement of Na between different solid phases during the solid state reactions and is responsible for the splitting of water. We know, for example, from our study that the sodium oxide that would result from the reaction of water and metallic Na to make hydrogen can undergo a solid state reaction with MnO to form $NaMnO_2$. Step 2 in the catalytic cycle (Figure 89) that generates $H_2$ from water with the conversion of $Na_2CO_3$ and MnO to $NaMnO_2$ could then involve multiple elementary processes: sodium carbonate decomposition to metallic Na and $CO_2$; the reaction of metallic Na with water to form $H_2$ and sodium oxides, and the reaction of the sodium oxide with MnO to form $NaMnO_2$.

An alternative explanation is that the TPD conditions for our model surface with $Na_2CO_3$ islands on MnO(100) are too far removed from the 850 °C (1123 K) operating conditions of the catalytic water splitting cycle [227]. In our UHV TPD experiments, the water and $Na_2CO_3$ reactants desorb (water) and decompose ($Na_2CO_3$) by 800 K – long before reaching the 1123 K reaction temperature. Therefore, it is possible that, the activation barrier for the water splitting reaction exceeds those for desorption of water and the decomposition of $Na_2CO_3$ at low pressure in our TPD experiments.

We took a one year no-cost extension on the current project period because of the delays associated with our move and the changes in the DOE funding cycle.

## 2.7 Results and Accomplishments 9/1/2016 – 8/31/2021

The last budget period focused on completion of tasks where the preparation of nominally stoichiometric and ordered MnO(100) surfaces can be accomplished by simple ion bombardment and annealing processes. Experiments examining the chemistry of oxidized MnO(100) surfaces were abandoned because our XPS system was down for the entire last budget period, and was not available to complete the characterization of Mn oxidation state required for verification of oxidation states required for work with oxidized surfaces.

One of our major activities for this project period has been to examine molecular adsorbates CO, $CO_2$, $H_2O$, coadsorbed $CO_2/H_2O$, $NH_3$, and hydrocarbon fragments (methyl and ethyl groups) on MnO(100) surfaces with DFT. These calculations are the basis for our comparison to accompanying experimental work. These adsorbates range from physisorbed/chemisorbed molecular adsorbates (CO, $CO_2$, $NH_3$), to dissociatively adsorbed systems that recombine upon desorption ($H_2O$), to reactive systems for studying dehydrogenation and C-H bond breaking (methyl and ethyl). We have examined the optimal, low energy adsorption sites for these species to determine the computed adsorption energy of the molecularly adsorbed species for comparison to benchmark TPD measurements. In the first year of this budget period we completed DFT calculations for CO, $CO_2$ and $H_2O$ adsorbed on MnO(100) terraces and very preliminary results with surface defects. In the second year of the budget period we examined multiple adsorption configurations around defects (atomic steps and O-atom vacancies) for $CO_2$, $H_2O$ and co-adsorbed of $CO_2$ and $H_2O$ around defects for comparison to experiment. In the final years of this budget period we addressed the reactive systems on MnO(100) experimentally with TPD and found that MnO(100) does not dissociate halogenated methane or ethane to produce any surface methyl or ethyl fragments. We examined a wide range of thermal and electron-stimulated conditions to dissociate methyl and ethyl halides on MnO(100), but were unable to observe any reaction.

Our second major activity was to complete the accompanying experimental benchmarks for comparison to the DFT simulations. In the first year of thebudget period we completed TPD experiments for CO, water, $CO_2$ and coadsorbed $H_2O/CO_2$ all on MnO(100). In the final years of this budget period we completed the TPD experiments and DFT calculations for comparison for both CO and $NH_3$ adsorption on MnO, and methyl and ethyl reactions on $Cr_2O_3(10\bar{1}2)$ experimental temperature-programmed desorption (TPD) studies of CO and $NH_3$ adsorption on MnO(100) with complimentary density functional theory (DFT) simulations were completed. TPD reveals a primary CO desorption signal at 130 K from MnO(100) in the low coverage limit giving an adsorption energy of -35.6 ±2.1 kJ/mol on terrace sites. PBE+U gives a more reasonable structural result than PBE which predicts a non-physical (2x2) surface reconstruction even for weakly adsorbed molecules, and the adsorption energy obtained by PBE+U and DFT-D3 Becke-Johnson dispersion corrections gives excellent agreement with the experimentally obtained $\Delta E_{ads}$ for adsorption at Mn2+ terrace sites. The analysis of NH3-TPD traces revealed that adsorption energy on MnO(100) is coverage-dependent. At the low-coverage limit, the adsorption energy on terraces is -58.7± 1.0 kJ/mol. A doser results in the formation of a transient NH3 multilayers that appears in TPD at around 110K. For a terrace site, PBE+U predicts a more

realistic surface adsorbate geometry than PBE does, with PBE+U with Tkatchenko-Scheffler method with iterative Hirshfeld partitioning (TSHP) provides the best prediction.

DFT simulations of the dehydrogenation elementary step of the ethyl and methyl fragments on α-$Cr_2O_3(10\bar{1}2)$ were also completed to complement previous TPD studies of these subjects. On the nearly-stoichiometric surface of α-$Cr_2O_3(10\bar{1}2)$, $CD_3$- undergoes dehydrogenation to produce $CD_2$=$CD_2$ and $CD_4$. Previous TPD traces suggest that the α-hydrogen (α-H) elimination of methyl groups on α-$Cr_2O_3(10\bar{1}2)$ is the rate-limiting step following dissociative adsorption of $CD_3I$, and has an activation barrier of 135 ± 2 kJ/mol. Simulations showed that DFT gives reasonable prediction of the adsorption sites for methyl fragments in agreement with high resolution synchrotron with XPS spectra, while DFT+U did not. Both DFT and DFT+U failed to predict the correct adsorption sites for methylene fragments, $CH_2$=. When the simulation is set in accordance with the experimentally observed adsorption sites for the carbon species, DFT gives very accurate prediction on the reaction barrier when an adjacent I adatom is present, while PBE+U failed spectacularly. When the simulation is set in accordance with the DFT-predicted adsorption sites, PBE is still able to accurately predict the reaction barrier (<1% to 8.7% error) while PBE+U is less accurate.

DFT was also used to complement the previous experimental studies of the β-H elimination from ethyl groups on the α-$Cr_2O_3(10\bar{1}2)$ surface following dissociative adsorption of $CH_3CH_2Cl$. The DFT simulation shows that in the absent surface Cl adatoms, DFT predicts an activation barrier of 92.6 kJ/mol, underpredicting the experimental activation barrier by 28.7%, while DFT+U predicts a barrier of 27.0 kJ/mol, under-predicting the experimental barrier by 79.2%. Inclusion of chlorine in the calculation indicates worsens the DFT-predicted reaction barrier, but also demonstrates that the primary failing of DFT+U is associated with the energetics of adsorbed ethyl chloride. DFT+U incorrectly predicts the molecular adsorption adsorption of ethyl chloride, such that that C-Cl bond clevage is the rate-limiting step. DFT accurately predicts a facile dissociation of ethyl chloride to an ethyl group and Cl adatom, with β-H elimination from ethyl fragments as the rate-limiting elementary step.

**3. What opportunities for training and professional development has the project provided?**

The primary training interactions during the past project period has been the PI's mentorship of Ph.D. students. Professional development activities for grad students included joint group meetings with computational and high-surface area catalysis groups in our department, and participation at conferences and synchrotron visits for both the PI and students. Conference participation only extended through 2019 as a result of the Covid-19 pandemic hitting in early 2020.

**Conference participation and presentations acknowledging full or partial DOE support:**

(† Invited)

1. † Surface Science Model of Manganese Oxide-Based Catalysts for Low-Temperature Thermochemical Water Splitting, D.F. Cox, Invited Seminar, Department of Chemical Engineering, University of Florida, Gainesville, FL, March 2020. *(cancelled due to COVID-19 pandemic)*
2. † Surface Science Model of Manganese Oxide-Based Catalysts for Low-Temperature Thermochemical Water Splitting, D.F. Cox, Invited Seminar, Department of Chemical and Biomedical Engineering, University of South Florida, Tampa, FL, November 2019.
3. Reactions of methyl and ethyl fragments on α-$Cr_2O_3$ $(10\bar{1}2)$, H. Chen, J.D. Brooks, C.M. Byrd and D.F. Cox, 2019 Annual Meeting of the AIChE, Orlando, FL, November 2019.
4. "Benchmarks for CO and $CO_2$ Adsorption on MnO(100): A Comparison of DFT to Experimental Data", H. Chen and D.F. Cox, 2018 Annual Meeting of the AIChE, Pittsburgh, PA, November 2018.

5. "Benchmarks for Adsorption on Transition Metal Oxide Surfaces: A Comparison of DFT to Experimental Data for $NH_3$ on MnO(100)", H. Chen and D.F. Cox, 2018 Annual Meeting of the AIChE, Pittsburgh, PA, November 2018.
6. Benchmarks for Adsorption on Transition Metal Oxide Surfaces: A Comparison of DFT to Experimental Data for $NH_3$ on MnO(100), H. Chen and D.F. Cox, 18th Annual Fall Symposium of the Southeastern Catalysis Society, Atlanta, GA, Sept. 2018.
7. "MnO(100): Initial Experimental Benchmarks for Adsorption and Co-Adsorption on the Ordered Surface and Oxidation to $Mn^{3+}$ Surface Compounds, H. Chen, X. Feng and D.F. Cox, 2018 BES Catalysis Sciences PI Meeting, Gaithersburg, MD, July 2018.
8. "Benchmarks for CO and $CO_2$ Adsorption on MnO(100): a Comparison of DFT to Experimental Data", H. Chen and D.F. Cox, 17th Annual Fall Symposium of the Southeastern Catalysis Society, Asheville, NC, Sept. 2017.
9. "Impact of Extreme Pressure on Bonded Radii of Atoms", N.L. Ross, G.V. Gibbs and D.F. Cox, 2017 Goldschmidt Conference, Paris, August 2017 *(partial support)*.
10. "MnO(100): Initial Experimental Benchmarks for Adsorption and Co-Adsorption on the Ordered Surface and Oxidation to $Mn^{3+}$ Surface Compounds, H. Chen, X. Feng and D.F. Cox, 2017 BES Catalysis Sciences PI Meeting, Gaithersburg, MD, July 2017.
11. "Benchmarks for Adsorption on Transition Metal Oxide Surfaces: A Comparison of DFT to Experimental Data", H. Chen and D.F. Cox, 2016 Annual Meeting of the AIChE, San Francisco, CA, November 2016.
12. "Benchmarking DFT Calculations for Transition Metal Oxide Surfaces: CO Adsorption on MnO(100)", H. Chen and D.F. Cox, 16th Annual Fall Symposium of the Southeastern Catalysis Society, Asheville, NC, Sept. 2016.
13. † "Reactions of Simple Alkyl and Carbene Intermediates on Transition Metal Oxide Surfaces" D.F. Cox, Invited Seminar, Department of Chemical and Life Science Engineering, Virginia Commonwealth University, Richmond, VA, April 2016.
14. † "Reactions of Simple Alkyl and Carbene Intermediates on Transition Metal Oxide Surfaces" D.F. Cox, Invited Seminar, Department of Chemical & Biomedical Engineering, Florida A&M/Florida State University, Tallahassee, FL, September 2015.
15. "Benchmarking DFT Calculations for Transition Metal Oxide Surfaces: $H_2O$ and $CO_2$ Adsorption on MnO(100)" H. Chen and D.F. Cox, 15th Annual Fall Symposium of the Southeastern Catalysis Society, Clemson, SC, September 2015.
16. "Bond length, electron density distribution, bond strength and bonded radii for oxides and sulfides" G.V. Gibbs, N.L. Ross, D.F. Cox and K.M Rosso, Geological Society of America, Vancouver, BC, November 2014 *(partial support)*.
17. † "Reactions of Simple Alkyl and Carbene Intermediates on Transition Metal Oxide Surfaces" D.F. Cox, Invited Seminar, Department of Chemical Engineering and Biomolecular Engineering, University of Tennessee, Knoxville, TN, October 2014.
18. "Na Adsorption on MnO(001)" X. Feng and D.F. Cox, 13th Annual Fall Symposium of the Southeastern Catalysis Society, Asheville, NC, September 2014.
19. † "Interaction of Na, $D_2O$, and $CO_2$ with Manganese Oxide Surfaces" X. Feng and D.F. Cox, Catalysis Research PI Meeting: Frontiers at the Interface of Homogeneous and Heterogeneous Catalysts, II, July 2014.
20. † "Reactions of Simple Alkyl and Carbene Intermediates on Transition Metal Oxide Surfaces" D.F. Cox, Invited Seminar, Department of Chemical Engineering, Kansas State University, Manhattan, KS, November 2013.

21. "$D_2O$ and $CO_2$ Adsorption On Na-Precovered MnO(001) and $NaMnO_2$-Like Surfaces" X. Feng and D.F. Cox, 2013 Annual Meeting of the AIChE, San Francisco, CA, November 2013.
22. "$D_2O$ and $CO_2$ Adsorption on Stoichiometric and Na-precovered MnO(001) Surfaces" X. Feng and D.F. Cox, 12th Annual Fall Symposium of the Southeastern Catalysis Society; Asheville, NC, September 2013.
23. "Pauling Bond Strength, Bond Length and Electron Density Distribution", G.V. Gibbs, N.L. Ross and D.F. Cox, Geological Society of America, Denver, CO, October 2013 *(partial support)*.
24. † "Hydrocarbon Oxidation, Dehydrogenation and Coupling over Model Metal Oxide Surfaces", D.F. Cox, DOE/BES: Hydrogen and Fuel Cells and Vehicle Technologies Programs Contractors' Meeting, Arlington, VA, May 2013.
25. "Reaction of Methylene on α-$Fe_2O_3(10\bar{1}2)$", Y. Dong and D.F. Cox, 2012 Annual Meeting of the AIChE, Pittsburgh, PA, November 2012.
26. "Reaction of Methylene on α-$Fe_2O_3(10\bar{1}2)$" Y. Dong and D.F. Cox, 11th Annual Fall Symposium of the Southeastern Catalysis Society; Asheville, NC, September 2012.
27. "Water Adsorption on Manganese Oxides: Water TPD on Stoichiometric and Oxidized MnO(001)", X. Feng and D.F. Cox, 11th Annual Fall Symposium of the Southeastern Catalysis Society; Asheville, NC, September 2012.
28. "Reaction Chemistry of Methyl and Methylene Species on α-$Cr_2O_3$ (0001)", Y. Dong and D.F. Cox, 58th International Symposium of the American Vacuum Society; Nashville, TN, November 2011.
29. † "Hydrocarbon Dehydrogenation and Oxidation over Model Metal Oxide Surfaces", D.F. Cox, Meeting of the Catalysis and Chemical Transformations Program, DOE/BES Contractors' Meeting 2011 DOE Catalysis Science Contractors' Meeting, Annapolis, MD, October 2011.
30. "XPS and LEED Characterization of the α-$Fe_2O_3$ $(10\bar{1}2)$ Surface", X. Feng, Y. Dong and D.F. Cox, 10th Annual Fall Symposium of the Southeastern Catalysis Society; Asheville, NC, September 2011.
31. "Reaction Chemistry of $C_1$ Hydrocarbon Intermediates on α-$Cr_2O_3$ (0001)", Y. Dong, T.-L. Chen, D.R. Mullins and D.F. Cox, 10th Annual Fall Symposium of the Southeastern Catalysis Society; Asheville, NC, September 2011.
32. "Molecular crystals as models for long-range directed Lewis acid-base van der Waals interactions: implications for nanoparticle formation", G.V. Gibbs, T.D. Crawford, A.F. Wallace, and D.F. Cox, 242nd National Meeting of the American Chemical Society; Denver, CO, September 2011 *(partial support)*.
33. "Reaction of Methylene on α-$Cr_2O_3$ $(10\bar{1}2)$: A Prototype for Surface Carbene Coupling Reactions on Non-Reducible Oxides", C.M. Byrd and D.F. Cox, Southeastern Catalysis Society Fall Symposium, Asheville, NC, September 2010.
34. "Reaction of Methylene on α- $Cr_2O_3$ $(10\bar{1}2)$: A Prototype for Surface Carbene Coupling Reactions on Non-Reducible Oxides", C.M. Byrd and D.F. Cox, 2009 Annual Meeting of the AIChE, Nashville, TN, November 2009.
35. "Structure sensitive reactions of ethyl groups on model chromia surfaces: Ethyl chloride on α-$Cr_2O_3$ $(10\bar{1}2)$ and (0001)", J.D. Brooks and D.F. Cox, 2009 Annual Meeting of the AIChE, Nashville, TN, November 2009.
36. "Surface Characterization and Oxygen Adsorption on α-$Cr_2O_3$ (0001), Y. Dong and D.F. Cox, 2009 Annual Meeting of the AIChE, Nashville, TN, November 2009.
37. † "Hydrocarbon Dehydrogenation and Oxidation over Model Metal Oxide Surfaces", D.F. Cox, Meeting of the Catalysis and Chemical Transformations Program, DOE/BES Contractors' Meeting 2009 DOE Catalysis Science Contractors' Meeting, Annapolis, MD, June 2009.
38. † "Selectivity in Ethane Dehydrogenation over Chromia", D.F. Cox, Symposium: *A Century of Surface Science and Catalysis*, 2008 Annual Meeting of the AIChE, Philadelphia, PA, November 2008.

39. "The reaction of ethyl, ethylidene and ethylidyne surface intermediates over the stoichiometric α- $Cr_2O_3$ $(10\bar{1}2)$ surface", J.D. Brooks and D.F. Cox, 82nd ACS Colloid and Surface Science Symposium, Raleigh, NC, June 2008.
40. "Surface Characterization and Oxygen Adsorption on α-$Cr_2O_3$ (0001), Y. Dong and D.F. Cox, 82nd ACS Colloid and Surface Science Symposium, Raleigh, NC, June 2008.
41. "Reaction pathways of ethyl and ethylidene intermediates on α-$Cr_2O_3$ $(10\bar{1}2)$", J.D. Brooks, Q. Ma and D.F. Cox, 2007 Annual Meeting of the AIChE, Salt Lake City, UT, November 2007.
42. "The reaction of ethyl and ethylidene surface intermediates over the stoichiometric α-$Cr_2O_3$ $(10\bar{1}2)$ surface", J.D. Brooks and D.F. Cox, Southeastern Catalysis Society Fall Symposium, Asheville, NC, September 2007.
43. "Surface Characterization and Oxygen Adsorption on α-$Cr_2O_3$(0001)", Y. Dong and D.F. Cox, Southeastern Catalysis Society Fall Symposium, Asheville, NC, September 2007.
44. † "Model Study of Reaction Intermediates in Chromia-Catalyzed Small Alkane Dehydrogenation", Department of Chemical Engineering, D.F. Cox, University of Florida; Gainesville, FL; October 2007.
45. † "Hydrocarbon Dehydrogenation and Oxidation over Model Metal Oxide Surfaces", D.F. Cox, Frontiers in Interfacial and Nano Catalysis: 2007 Meeting of the Catalysis and Chemical Transformations Program, DOE/BES Contractors' Meeting, Wintergreen, VA, May 2007.
46. † "Bonded interactions in Fe and Cu Sulfides", G.V. Gibbs, D.F. Cox, K.M. Rosso, N.L. Ross and R.T. Downs, American Geophysical Union, San Francisco, December 2006 *(partial support)*.
47. † "Model Study of Surface Reaction Intermediates in Chromia-Catalyzed Small Alkane Dehydrogenation", Department of Chemical and Biomolecular Engineering, D.F. Cox, University of Nebraska; Lincoln, NE; November 2006.
48. "Ultra High Vacuum Surface Science Studies of Model Heterogeneous Catalysts", D.F. Cox, Deans' Forum on Energy Security and Sustainability, Virginia Tech, Blacksburg, VA, October 2006.
49. "Dehalogenation of dichloroethylene isomers on α-$Cr_2O_3$ $(10\bar{1}2)$", M.A. Minton and D.F. Cox, 2005 Annual Meeting of the AIChE, Cincinnati, OH, November 2005.
50. "A simple chemical view of relaxations at (110) surfaces of rutile structure-type oxides", T.M. Muscenti, G.V. Gibbs and D.F. Cox, 2005 Annual Meeting of the AIChE, Cincinnati, OH, November 2005 *(partial support)*.
51. "ELF isosurface maps of the $Al_2SiO_5$ polymorphs", J.B. Burt, N.L. Ross, G.V. Gibbs and D.F. Cox, 2005 Annual Meeting of the Geological Society of America, Salt Lake City, UT, October 2005 *(partial support)*.
52. "Reactions of Di-Halogenated Ethylenes on the α-$Cr_2O_3$ $(10\bar{1}2)$ Surface", M.A. Minton and D.F. Cox, Southeastern Catalysis Society Fall Symposium, Asheville, NC, September 2005.
53. "A simple chemical view of relaxations at stoichiometric (110) surfaces of rutile structure-type oxides", T.M. Muscenti, G.V. Gibbs and D.F. Cox, Southeastern Catalysis Society Fall Symposium, Asheville, NC, September 2005 *(partial support)*.
54. "Reactions of Vinyl Chloride on α-$Cr_2O_3$ $(10\bar{1}2)$", M.A. Minton, Q. Ma, D.F. Cox and David R. Mullins, 19th North American Catalysis Society Meeting, Phildelphia, PA, May 2005.
55. "The electron localization function, a probe for exploring bonded and nonbonded features in Earth materials, G.V. Gibbs, D.F.Cox, N.L. Ross, J.B. Burt and K.M Rosso, Pacific Northwest National Laboratory, January 2005 *(partial support)*.
56. † "The electron localization function, a probe for studying bonded interactions in earth materials", G.V. Gibbs, D.F. Cox, N.L. Ross and J.B. Burt, Annual Meeting of the Geological Society of America, Denver, CO, November 2004 *(partial support)*. (invited talk – gvg)

57. † "A comparison of experimental and theoretical bond critical point properties for earth materials", G.V. Gibbs, D.F. Cox and KM. Rosso, Pittsburgh Diffraction Conference, Pittsburg, PA, October 2004 *(partial support)*. (invited talk – gvg)
58. "Vinyl-Mediated Reactions of Vinyl Chloride on $\alpha$-$Cr_2O_3$ $(10\bar{1}2)$", M.A. Minton, Q. Ma, D.F. Cox and D.R. Mullins, **Southeastern Catalysis Society Fall Symposium, Asheville, NC, September 2004.**
59. † "Characterization of hydrocarbon fragments on model metal oxide surfaces at U12A: $C_2$ Alkenyl Species on Stoichiometric $\alpha$-$Cr_2O_3$ $(10\bar{1}2)$", M.A. Minton, Q. Ma and D.F. Cox, National Synchrotron Light Source, Brookhaven National Laboratory, Upton, NY, July 2004.
60. † "A Modeling of the Structure and Favorable H-Docking Sites and Defects for the High-Pressure Silica Polymorph Stishovite, G.V. Gibbs, D.F. Cox and N.L. Ross, 32nd International Geological Congress, Florence, Italy, August 2004 *(partial support)*. (Keynote Address – gvg)
61. † "A comparison of theoretical and experimental properties of the electron density distributions for earth materials", G.V Gibbs, D.F. Cox and K.M. Rosso, Pacific Northwest National Laboratory, June 2004 *(partial support)*.
62. "Hydrocarbon Dehydrogenation and Oxidation over Model Metal Oxide Surfaces", D.F. Cox, Frontiers In Catalysis Science: Meeting of the Catalysis and Chemical Transformations Program, DOE/BES Contractors' Meeting, Rockville, MD, May 2004.
63. "Decomposition and Coupling of Vinyl Species on Stoichiometric $\alpha$-$Cr_2O_3$ $(10\bar{1}2)$", M.A. Minton, Q. Ma and D.F. Cox, 2003 Annual Meeting of the AIChE, San Francisco, CA, November 2003.
64. "Potential Hydrogen Bonding Sites in Andalusite, Sillimanite, and Kyanite", J.B. Burt, D.F. Cox, N.L. Ross, G.V. Gibbs and K.M. Rosso, 2003 Annual Meeting of the Geological Society of America, Seattle, WA, November 2003 *(partial support)*.
65. "Coupling and Decomposition of Surface Vinyl Species on Stoichiometric $\alpha$-$Cr_2O_3$ $(10\bar{1}2)$", Q. Ma, M.A. Minton and D.F. Cox, 77th ACS Colloid and Surface Science Symposium, Atlanta, GA, June 2003.
66. "Reaction of Methyl Fragments on Stoichiometric $\alpha$-$Cr_2O_3$ $(10\bar{1}2)$", C.M. Byrd, Q. Ma, M.A. Minton and D.F. Cox, 77th ACS Colloid and Surface Science Symposium, Atlanta, GA, June 2003.
67. "Decomposition and Coupling of Surface Vinyl Species on Stoichiometric $\alpha$-$Cr_2O_3$ $(10\bar{1}2)$", M.A. Minton, Q. Ma and D.F. Cox, Southeastern Catalysis Society Spring Symposium, Asheville, NC, April 2003.
68. "Reaction of Methyl Iodide on Stoichiometric $\alpha$-$Cr_2O_3$ $(10\bar{1}2)$", C.M. Byrd, Q. Ma, M.A. Minton and D.F. Cox, Southeastern Catalysis Society Spring Symposium, Asheville, NC, April 2003.
69. † "Reactions of Methanol on Stoichiometric and O-terminated $Cr_2O_3(10\bar{1}2)$", C.M. Byrd, M.W. Mensch and D.F. Cox, 2002 Annual Meeting of the AIChE, Indianapolis, IN November 2002. (Alpha Chi Sigma Award Symposium honoring Mark A. Barteau, recipient of the 2002 Alpha Chi Sigma Award from AIChE)
70. "Nonbonding Electron-Pairs and Favorable Docking Sites for Protons in Coesite, Quartz and Stishovite", G.V. Gibbs, D.F. Cox, M.B. Boisen, R.T. Downs and N.L. Ross, 18th General Meeting of the International Mineralogical Association, Edinburgh, Scotland, September 2002 *(partial support)*. (Invited Plenary Lecture – gvg).
71. "Oxidation of Methanol over the $Cr_2O_3$ $(10\bar{1}2)$ Surface", C.M. Byrd, M.W. Mensch and D.F. Cox, Tri-State Catalysis Society Spring Symposium, Lexington, KY, May 2002.
72. "$CO_2$ and $BF_3$ Adsorption on $Cr_2O_3$ $(10\bar{1}2)$: Probing Surface Basicity and Oxygen Anions", M.W. Abee and D.F. Cox, Tri-State Catalysis Society Spring Symposium, Lexington, KY, May 2002.
73. "$CO_2$ and $BF_3$ Adsorption on $Cr_2O_3$ $(10\bar{1}2)$: Probing Surface Basicity and Oxygen Anions", M.W. Abee and D.F. Cox, 2001 IUVSTA 15th International Vacuum Congress (IVC-15), American Vacuum Society 48th International Symposium (AVS-48), & 11th International Conference on Solid Surfaces (ICSS-11), San Francisco, CA, Oct. 2001.

74. "$CH_3I$ Adsorption and Reaction on $Cr_2O_3$ ($10\bar{1}2$): Oxidation of Surface Methyl Groups", C.M. Byrd and D.F. Cox, 2000 Annual Meeting of the AIChE, Los Angeles, CA, Nov. 2000.
75. † "Influence of Local Structure on Chemisorption Properties and Oxidation Reactions Over Metal Oxide Surfaces", D.F. Cox, 11th DOE/BES Heterogeneous Catalysis and Surface Chemistry Research Conference; Rockville, MD, August 2000.
76. "$CO_2$ and $BF_3$ Adsorption on $Cr_2O_3$ ($10\bar{1}2$): Probing Surface Basicity and Oxygen Anions", M.W. Abee and D.F. Cox, 1999 Annual Meeting of the AIChE, Dallas, TX, Nov. 1999.
77. "Basicity of Specific Features on Well-Defined $Cr_2O_3$ ($10\bar{1}2$) Surfaces", M.W. Abee and D.F. Cox, 1999 Spring Symposium of the Tri-State Catalyst Society, Louisville, KY, April 1999.
78. "Oxidation of Hydrocarbon Fragments on $SnO_2$ (110)", C.M. Byrd and D.F. Cox, 1999 Spring Symposium of the Tri-State Catalyst Society, Louisville, KY, April 1999.
79. "A Computational Look at Tin Oxide Surface Chemistry", D.F. Cox and D.M. Teter, 1998 Spring Symposium of the Tri-State Catalyst Society, Charleston, WV, April 1998.
80. "Acidic Properties of Specific Features on Well-Defined $SnO_2$ (110) Surfaces", M.W. Abee and D.F. Cox, 71st ACS Colloid and Surface Science Symposium, Newark, DE, June 1997.
81. "Dehalogenation of $CFCl_2CH_2Cl$ and $CFCl{=}CH_2$ over $Cr_2O_3$ ($1\bar{1}02$)", S.C. York and D.F. Cox, 15th North American Catalysis Society Meeting, Chicago, IL, May 1997.
82. † Plenary Lecture: "Adsorption and Reaction at Defects on Oxide Surfaces", D.F. Cox, 19th Annual Spring Symposium of the Michigan Catalysis Society, Dearborne, MI, May 1997.
83. "Halogen-Oxygen Exchange over the $Cr_2O_3$ ($1\bar{1}02$) Surface", T.J. Conway, S.C. York and D.F. Cox, Tri-State Catalysis Club Spring Symposium; Charleston, West Virginia, April 1997.
84. "$CO_2$ as a Probe of $Cr_2O_3$ ($1\bar{1}02$) Surface Properties", S.C. York and D.F. Cox. Tri-State Catalysis Club Spring Symposium; Charleston, West Virginia, April 1997.

**4. How have the results been disseminated to communities of interest?**

Dissemination of results locally has been through student and faculty participation in joint group meetings, and outreach to VT undergraduates and pre-college visitors to campus. Externally, our primary methods of dissemination are through seminars/talks and publications.

**5. What do you plan to do during the next reporting period to accomplish the goals?**

N/A – project has ended

# PRODUCT DETAILS

**Journal publications acknowledging full or partial DOE support**

1. H. Chen and D.F. Cox, CO adsorption on MnO(100): experimental benchmarks compared to DFT, *Surface Science*, **707** (2021) 121808.
2. X. Feng and D.F. Cox, Synthesis of a planar, multicomponent catalytic surface of $Na_2CO_3$/MnO, *Surface Science*, **707** (2021) 121807.
3. X. Feng and D.F. Cox, Oxidation of MnO(100) and $NaMnO_2$ formation: Characterization of $Mn^{2+}$ and $Mn^{3+}$ Surfaces via XPS and Water TPD, *Surface Science*, **675** (2018) 47-53.
4. G.V. Gibbs, N.L. Ross and D.F. Cox, Sulfide Bonded Atomic Radii, *Physics and Chemistry of Minerals,* **44** (2017) 561-566. (partial support)
5. X. Feng and D.F. Cox, Na Deposition on MnO(100), *Surface Science,* **645** (2016) 23-29.
6. Y. Dong, J.D. Brooks, T.L. Chen, D.R. Mullins and D.F. Cox, Reactions of methyl groups on a non-reducible metal oxide: the reaction of iodomethane on stoichiometric α-$Cr_2O_3$(0001), *Surface Science,* **641** (2015) 148-153.
7. G.V. Gibbs, N.L. Ross and D.F Cox, Bond length estimates for oxide crystals with a molecular power law expression, *Physics and Chemistry of Minerals,* **42** (2015) 587-593. (partial support)
8. Y. Dong, J.D. Brooks, T.L. Chen, D.R. Mullins and D.F. Cox, Methylene migration and coupling on a non-reducible metal oxide: the reaction of dichloromethane on stoichiometric α-$Cr_2O_3$(0001), *Surface Science*, **632** (2015) 28-38.
9. G.V. Gibbs, N.L. Ross, D.F. Cox and K.M. Rosso, Insights into the crystal chemistry of earth materials rendered by electron density distributions: Pauling's rules revisited, *American Mineralogist,* **99** (2014) 1071-1084. (partial support)
10. G.V. Gibbs, N.L. Ross, D.F. Cox, K.M. Rosso, B.B.Iversen and M.A. Spackman, Pauling Bond Strength, Bond Length and Electron Density Distributions, *Physics and Chemistry of Minerals,* **41** (2014) 17-25. (partial support)
11. G.V. Gibbs, N.L. Ross, D.F. Cox, K.M. Rosso, B.B. Iversen and M.A. Spackman, Bonded radii and the contraction of the electron density of the oxygen atom by bonded interactions, *The Journal of Physical Chemistry A*, **117** (2013) 1632-1640. (partial support)
12. G.V. Gibbs, D. Wang, C. Hin, N.L. Ross, D.F. Cox, T.D. Crawford, M.A. Spackman, R.J. Angel, Properties of atoms under pressure: Bonded interactions of the atoms in three perovskites, *The Journal of Chemical Physics*, **137** (2012) 164313. (partial support)
13. G.V. Gibbs, T.D. Crawford, A.F. Wallace, D.F. Cox, R.M. Parrish, E.G. Hohenstein and C.D. Sherrill, Role of Long-Range Intermolecular Forces in the Formation of Inorganic Nanoparticle Clusters, *The Journal of Physical Chemistry A*, **115** (2011) 12933-12940. (partial support) (Invited contribution for a Festschrift commemorating the 80$^{th}$ birthday of R.F.W. Bader)
14. J.D. Brooks, T.L. Chen, D.R. Mullins and D.F. Cox, Reactions of ethylidene on a model chromia surface:1,1-dichloroethane on stoichiometric α-$Cr_2O_3$ ($10\bar{1}2$), *Surface Science*, **605** (2011) 1170-1176.
15. G.V. Gibbs, A.F. Wallace, R.T. Downs, N.L. Ross, D.F. Cox and K.M. Rosso, Thioarsenides: van der Waals bonded Interactions and bond paths, *Physics and Chemistry of Minerals*, **38** (2011) 267-291. (partial support)
16. G.V. Gibbs, A.F. Wallace, R. Zallen, R.T. Downs, N.L. Ross, D.F. Cox and K.M. Rosso, Bond Paths and van der Waals Interactions in Orpiment, $As_2S_3$, *The Journal of Physical Chemistry A*, **114** (2010) 6550-6557. (partial support)

17. G.V. Gibbs, A.F. Wallace, D.F. Cox, R.T Downs, N.L. Ross and K.M Rosso, Si-O Bonded Interactions, Silica Polymorphs and Siloxane Molecules, *American Mineralogist,* **94** (2009) 1085-1102. (partial support)
18. J.D. Brooks, Q. Ma and D.F. Cox, Reactions of ethyl groups on a model chromia surface: ethyl chloride on stoichiometric $\alpha$-$Cr_2O_3$ $(10\bar{1}2)$, *Surface Science*, **603** (2009) 523-528.
19. M.A. McKee, Q. Ma, D.R. Mullins, M. Neurock and D.F. Cox, Reactions of vinyl groups on a model chromia surface: vinyl chloride on stoichiometric $\alpha$-$Cr_2O_3$ $(10\bar{1}2)$, *Surface Science*, **603** (2009) 265-272.
20. G.V. Gibbs, A.F. Wallace, D.F. Cox, P.M. Dove, R.T Downs, N.L. Ross and K.M Rosso, The role of directed van der Waals bonded interactions in the determination of the structures of molecular arsenate solids, *The Journal of Physical Chemistry A*, **113** (2009) 736-749. (partial support)
21. G.V. Gibbs, R.T. Downs, D.F. Cox, K.M. Rosso, N.L. Ross, A. Kirfel, T. Lippmann, W. Morgenroth and T.D. Crawford, Experimental bond critical point and local energy density properties determined for Mn-O, Fe-O and Co-O bonded interactions for tephroite, $Mn_2SiO_4$, fayalite, $Fe_2SiO_4$ and $Co_2SiO_4$ olivine and selected organic metal complexes: Comparison with properties calculated for non-transition and transition metal M-O bonded interactions for silicates and oxides, *The Journal of Physical Chemistry A*, **112** (2008) 8811-8823. (partial support)
22. G.V. Gibbs, R.T. Downs, D.F. Cox, N.L. Ross, M.B. Boisen, Jr. and K.M. Rosso, Shared and closed-shell O-O interactions in silicates, *The Journal of Physical Chemistry A*, **112** (2008) 3693-3699. (partial support)
23. G.V. Gibbs, R.T. Downs, D.F. Cox, N.L. Ross, C.T. Prewitt, K.M. Rosso, T. Lippmann and A. Kirfel, Connections Between Bonded Interactions and the Crystal Chemistry of Minerals: A Review, *Zeitschrift für Kristallographie*, **223** (2008) 1-40. (partial support)
24. S. Das, D.F. Cox, G.L. Wilkes, D.B. Klinedinst, I. Yilgor, E. Yilgor, and F.L. Beyer, Effect of Symmetry and H-bond Strength of Hard Segments on the Structure-Property Relationships of Segmented, Nonchain Extended Polyurethanes and Polyureas, *Journal of Macromolecular Science, Part B: Physics*, **46** (2007) 853-875.
25. G.V. Gibbs, D.F. Cox, K.M. Rosso, N.L. Ross, R.T. Downs, and M.A. Spackman, Theoretical electron density distributions for Fe and Cu sulfide Earth materials: a connection between bond length, bond critical point properties, local energy densities and bonded interactions, *The Journal of Physical Chemistry B*, **111** (2007) 1923-1931. (partial support)
26. G.V. Gibbs, D. Jayatilaka, M.A. Spackman, D.F. Cox and K.M. Rosso, Si-O bonded interactions in silicate crystals and molecules: A comparison, *The Journal of Physical Chemistry A*, **110** (2006) 12678-12683. (partial support)
27. G.V. Gibbs, M. A. Spackman, D. Jayatilaka, K.M. Rosso and D.F. Cox, Bond length and local energy density property connections for non-transition metal oxide bonded interactions, *The Journal of Physical Chemistry A*, **110** (2006) 12259-12266. (partial support)
28. J.B. Burt, G.V. Gibbs, D.F. Cox and N.L. Ross, ELF isosurface maps for the $Al_2SiO_5$ polymorphs, *Physics and Chemistry of Minerals*, **33** (2006) 138-144. (partial support)
29. G.V. Gibbs, D.F Cox, T.D. Crawford, K.M., Rosso and N.L. Ross, Classification of MO Bonded Interactions Based on Local Potential and Kinetic Energy Densities, *The Journal of Chemical Physics*, **124** (2006) article no. 084704. (partial support)
30. G.V. Gibbs, R.T. Downs, C.T. Prewitt, K.M. Rosso, N.L. Ross and D.F. Cox, Electron Density Distributions Calculated for the Nickel Sulfides Millerite, Vaesite and Heazlewoodite and Ni Metal: A Case for the Importance of Ni-Ni Bond Paths for Electron Transport, *The Journal of Physical Chemistry B*, **109** (2005) 21788-21795. (partial support)
31. G.V. Gibbs, D.F. Cox, N.L. Ross, D.L. Crawford, R.T. Downs and J.B. Burt, Comparison of the Electron Localization Function and Deformation Electron Density Maps for Selected Earth Materials, *The Journal of Physical Chemistry A*, **109** (2005) 10022-10027. (partial support)

32. T.M. Muscenti, G.V. Gibbs and D.F. Cox, A simple chemical view of relaxations at stoichiometric (110) surfaces of rutile structure-type oxides: a first-principles study of stishovite, $SiO_2$, *Surface Science*, **594** (2005) 70-82.
33. Kirfel, T. Lippmann, P. Blaha, K. Schwarz, D.F. Cox, K.M. Rosso and G.V. Gibbs, Electron density distribution and bond critical point properties for forsterite, $Mg_2SiO_4$, determined with synchrotron single crystal X-ray diffraction data, *Physics and Chemistry of Minerals*, **32** (2005) 301-313. (partial support)
34. G. V. Gibbs, D.F. Cox, N.L. Ross, T.D. Crawford, J.B. Burt, K.M. Rosso, A mapping of the electron localization function for earth materials, *Physics and Chemistry of Minerals*, **32** (2005) 208-221. (partial support)
35. G.V. Gibbs, D.F. Cox, K.M. Rosso, A. Kirfel, T. Lippmann, P. Blaha and K. Schwarz, Experimental and theoretical bond critical point properties for model electron density distributions for earth materials, *Physics and Chemistry of Minerals*, **32** (2005) 114-125. (partial support)
36. G.V. Gibbs, D.F. Cox and K.M. Rosso, A Connection Between Bond Strength and Electron Density at the SiO Bond Critical Points in Silicates, *The Journal of Physical Chemistry A*, **108** (2004) 7643-7645. (partial support)
37. G.V. Gibbs, D.F. Cox and N.L. Ross, A Modeling of the Structure and Favorable H-Docking Sites and Defects for the High-Pressure Silica Polymorph Stishovite, *Physics and Chemistry of Minerals*, **31** (2004) 232-239. (partial support)
38. M.W. Mensch, C.M. Byrd and D.F. Cox, Reaction of Methanol on Stoichiometric and O-terminated $\alpha$-$Cr_2O_3$ ($10\bar{1}2$): Interconversion of Oxygenated $C_1$ Surface Intermediates, *Catalysis Today*, **85** (2003) 279-289. (Invited contribution for a special issue on oxides.)
39. G.V. Gibbs, K.M. Rosso, D.F. Cox and M.B. Boisen, Jr., A Physical Basis for Pauling's Definition of Bond Strength, *Physics and Chemistry of Minerals*, **30** (2003) 317-320. (partial support)
40. G.V. Gibbs, D.F. Cox, M.B. Boisen, Jr., R.T. Downs and N.L. Ross, The Electron Localization Function: A Tool for Locating Favorable Proton Docking Sites in the Silica Polymorphs, *Physics and Chemistry of Minerals*, **30** (2003) 305-316. (partial support)
41. S.C. York and D.F. Cox, Dehalogenation of 1,1,2-trichloro-1-fluoroethane over $\alpha$-$Cr_2O_3$ ($10\bar{1}2$), *The Journal of Physical Chemistry B*, **107** (2003) 5182-5189.
42. M.W. Abee and D.F. Cox, $BF_3$ Adsorption on Stoichiometric and Oxygen-Deficient $SnO_2$ (110) Surfaces, *The Journal of Physical Chemistry B*, **107** (2003) 1814-1820.
43. S.C. York and D.F. Cox, Dehalogenation of 1-chloro-1-flouroethene to Acetylene on $\alpha$-$Cr_2O_3$ ($10\bar{1}2$), *Journal of Catalysis*, **214** (2003) 273-283.
44. M.W. Abee and D.F. Cox, $NH_3$ Adsorption on Stoichiometric and Oxygen-Deficient $SnO_2$ (110) Surfaces, *Surface Science*, **520** (2002) 65-77.
45. T.P. St.Clair, S.T. Oyama and D.F. Cox, Adsorption and Reaction of Thiophene on $\alpha$-$Mo_2C$ (0001), *Surface Science*, **511** (2002) 294-302.
46. T.W. Terriberry, D.F. Cox and D.A. Bowman, A User-Centered Tool for the Interactive 3D Visualization of Electronic Structure in Molecules and Solids, *Computers and Chemistry*, **26** (2002) 313-319.
47. G.V. Gibbs, D.F. Cox, T.D. Crawford, M.B. Boisen, Jr., and M.S. Lim, A Mapping of the Electron Localization Function for the Silica Polymorphs: Evidence for Domains of Electron Pairs and Sites of Electrophillic Attack, *Physics and Chemistry of Minerals*, **29** (2002) 307-318. (partial support)
48. M.W. Abee and D.F. Cox, $BF_3$ Adsorption on $\alpha$-$Cr_2O_3$ ($10\bar{1}2$): Probing the Lewis Basicity of Surface Oxygen Anions, *The Journal of Physical Chemistry B*, **105** (2001) 8375-8380.
49. M.W. Abee, S.C. York and D.F. Cox, $CO_2$ Adsorption on $\alpha$-$Cr_2O_3$ ($10\bar{1}2$) Surfaces, *The Journal of Physical Chemistry B*, **105** (2001) 7755-7761.

50. T.P. St.Clair, S.T. Oyama and D.F. Cox, CO and $O_2$ Adsorption on $\alpha$-$Mo_2C$ (0001), *Surface Science*, **468** (2000) 62-76.
51. M.W. Abee and D.F. Cox, Stoichiometric and Oxygen-Terminated $\alpha$-$Cr_2O_3$ $(10\bar{1}2)$ Surfaces, *Surface Science Spectra*, **7** (2000) 134-142.
52. S.C. York, M.W. Abee and D.F. Cox, $\alpha$-$Cr_2O_3$ $(10\bar{1}2)$: Surface Characterization and Oxygen Adsorption, *Surface Science*, **437** (1999) 386-396.
53. A.-C. Christiaen, M.W. Abee and D.F. Cox, Stoichiometric and Non-Stoichiometric $Cu_2O$ (111) Single Crystal Surfaces, *Surface Science Spectra*, **4** (1996-97) 279-287. (Invited contribution for a special issue on oxides.)
54. A.-C. Christiaen, M.W. Abee and D.F. Cox, Stoichiometric and Non-Stoichiometric $SnO_2$ (110) Surfaces, *Surface Science Spectra*, **4** (1996-97) 220-231. (Invited contribution for a special issue on oxides.)

**Thesis and Dissertations Acknowledging DOE Support**

Dr. Han Chen
Degree Conferred: May 2021
**Ph.D. Dissertation:** "Experimental Adsorption and Reaction Studies on Transition Metal Oxides Compared to DFT Simulations"

Dr. Xu Feng
Degree Conferred: September 2015
**Ph.D. Dissertation:** "Interactions of Na, $O_2$, $CO_2$ and Water with MnO(100): Modeling a Complex Mixed Oxide Sysem for Thermochemical Water Splitting"

Dr. Yujung Dong
Degree Conferred: September 2012
**Ph.D. Dissertation:** "Geometric and Electronic Structure Sensitivity of Methyl and Methylene Reactions on $\alpha$-$Cr_2O_3$ and $\alpha$-$Fe_2O_3$ Surfaces"

Dr. John D. Brooks
Degree Conferred: September 2010
**Ph.D. Dissertation:** "Model Chromia Surface Chemistry: $C_2$ Alkyl Fragment Reactions and Probe Molecule Interactions"

Dr. Mary A. Minton (McKee)
Degree Conferred: December 2006
**Ph.D. Dissertation:** "Reactions of Halogenated Ethylenes on the $\alpha$-$Cr_2O_3$ $(10\bar{1}2)$ Surface"

Mr. Qiang Ma
Degree Conferred: August 2005
**M.S. Thesis:** "Haloethane Reactions Over the Chromia $Cr_2O_3$ $(10\bar{1}2)$ Surface"

Mr. Thomas Muscenti
Degree Conferred: December 2004
**M.S. Thesis:** "Density Functional Theory Study of Rutile $SiO_2$: An Electron Pair Description of Bulk and Surface Properties"

Dr. Chad M. Byrd

Degree Conferred: August 2003
**Ph.D. Dissertation:** "Reaction Chemistry of $C_1$ Hydrocarbon Fragments and Oxygenates on $Cr_2O_3$ $(10\bar{1}2)$"

Mr. Michael W. Mensch
Degree Conferred: May 2003
**M.S. Thesis:** "The Oxidation of Methanol on $Cr_2O_3$ $(10\bar{1}2)$ Single Crystal Surfaces"

Dr. Mark W. Abee
Degree Conferred: September 2001
**Ph.D. Dissertation:** "Interaction of Acid/Base Probe Molecules with Specific Features on Well-Defined Metal Oxide Single-Crystal Surfaces"

Dr. Steven C. York
Degree Conferred: August 1999
**Ph.D. Dissertation:** "Halocarbon Reactions on the $Cr_2O_3$ $(10\bar{1}2)$ Surface"

Dr. Todd P. St.Clair
Degree Conferred: August 1998 (Coadvisor: S. Ted Oyama)
**Ph.D. Dissertation:** "Characterization and Reactivity of $Mo_2C$" (partial support)

Mr. Timothy J. Conway
Degree Conferred: December 1997
**M.S. Thesis:** "Scanning Tunneling Microscopy and Adsorption Studies on Single Crystal Metal Oxide Surfaces"

**INTELLECTUAL PROPERTIES DETAIL**
There are no intellectual properties to report.

**TECHNOLOGIES AND TECHNIQUES DETAIL**
There are no technologies or techniques to report.

**OTHER PRODUCTS DETAIL**
There are no other products to report.

# PARTICIPANTS AND OTHER COLLABORATING ORGANIZATIONS

## PARTICIPANTS DETAIL

| | | |
|---|---|---|
| **1. Participant:** Dr. David F Cox | | |
| **Project Role**: Principal Investigator/Project Director | **Person Months Worked**: 11 | **Funding Support (if other than this award)**: Virginia Tech 10 months; DOE 1month for the last budget period, but varied over the course of the project |
| **Contribution to the Project**: Directing experiments and computations of graduate students on the project. | | |
| **International Collaboration: No** | | |
| **International Travel: No** | | |

## PARTNERS DETAIL

| |
|---|
| **1. Partner:** Virginia Tech Advanced Research Computing (VT ARC), Blacksburg, VA, USA |
| **Partner Contribution:** In-kind Support, Facilities Support |
| **Description of the Contribution:** Free access to BlueRidge computing cluster for DFT calculations at 1 million core hours per year. |

## OTHER COLLABORATORS DETAIL

| |
|---|
| **1. Description of the Contribution:**<br>G.V. Gibbs, VT Geosciences: Collaboration on electronic structure of minerals. |

| |
|---|
| **2. Description of the Contribution:**<br>N.L. Ross, VT Geosciences: Collaboration on electronic structure of minerals. |

# IMPACT

| |
|---|
| **1. What is the impact on the development of the principal discipline(s) of the project?** |
| Nothing to Report |
| **2. What is the impact on other disciplines?** |
| Nothing to Report |
| **3. What is the impact on the development of human resources?** |
| Nothing to Report |
| **4. What is the impact on physical, institutional, and information resources that form infrastructure?** |
| Nothing to Report |
| **5. What is the impact on technology transfer?** |
| Nothing to Report |
| **6. What is the impact on society beyond science and technology?** |
| Nothing to Report |
| **7. Foreign Spending** |
| None to Report |

# CHANGES - PROBLEMS

| |
|---|
| **1. Changes in approach and reasons for change** |
| Nothing to Report |
| **2. Actual or anticipated problems or delays and actions or plans to resolve them** |
| N/A. Project has ended. |
| **3. Changes that have a significant impact on expenditures** |
| Covid pandemic prevented planned hire of a postdoc, and pandemic delayed the graduation of the final PhD student working on the project. Two one-year no-cost extensions were approved to complete the project. |
| **4. Significant changes in use or care of human subjects, vertebrate animals, and/or biohazards** |
| Nothing to Report |
| **5. Change of primary performance site location from that originally proposed** |
| Nothing to Report |
| **6. Carryover Amount** |
| Project Ended. Virginia Tech OSP to determine if there are any unexpended funds. |

## REFERENCES

[1] V.A. Gercher, D.F. Cox, J.M. Themlin, Oxygen-Vacancy-Controlled Chemistry on a Metal Oxide Surface - Methanol Dissociation and Oxidation on $SnO_2$(110), Surface Science, 306 (1994) 279-293.
[2] V.A. Gercher, Influence of Oxygen Vacancies on Oxygenate Reactions over $SnO_2$(110) Single Crystal Surfaces, in: Chemical Engineering, Virginia Tech, 1994.
[3] M.A. Barteau, Site Requirements of Reactions on Oxide Surfaces, Journal of Vacuum Science & Technology a-Vacuum Surfaces and Films, 11 (1993) 2162-2168.
[4] M.W. Abee, Interaction of Acid/Base Probe Molecules with Specific Features on Well-Defined Metal Oxide Single-Crystal Surfaces, in: Chemical Engineering, Virginia Tech, 1999.
[5] M.W. Abee, D.F. Cox, $NH_3$ chemisorption on stoichiometric and oxygen-deficient $SnO_2$(110) surfaces, Surface Science, 520 (2002) 65-77.
[6] K.H. Schulz, D.F. Cox, PHOTOEMISSION AND LOW-ENERGY-ELECTRON-DIFFRACTION STUDY OF CLEAN AND OXYGEN-DOSED CU2O (111) AND (100) SURFACES, Physical Review B, 43 (1991) 1610-1621.
[7] H.L. Finston, H.L. Finston, A.C. Rychtman, A New View of Current Acid-base Theories, Wiley, 1982.
[8] H. Knöuzinger, Specific Poisoning and Characterization of Catalytically Active Oxide Surfaces, in: D.D. Eley, H. Pines, P.B. Weisz (Eds.) Advances in Catalysis, Academic Press, 1976, pp. 184-271.
[9] G. Busca, V. Lorenzelli, INFRARED SPECTROSCOPIC IDENTIFICATION OF SPECIES ARISING FROM REACTIVE ADSORPTION OF CARBON OXIDES ON METAL-OXIDE SURFACES, Materials Chemistry, 7 (1982) 89-126.
[10] A. Zecchina, S. Coluccia, E. Guglielminotti, G. Ghiotti, INFRARED STUDY OF SURFACE PROPERTIES OF ALPHA-CHROMIA .3. ADSORPTION OF CARBON DIOXIDE, Journal of Physical Chemistry, 75 (1971) 2790-+.
[11] H.J. Freund, M.W. Roberts, Surface chemistry of carbon dioxide, Surface Science Reports, 25 (1996) 225-273.
[12] V.E.C.P.A. Henrich, The surface science of metal oxides, Cambridge University Press, Cambridge; New York, 1994.
[13] O. Seiferth, K. Wolter, B. Dillmann, G. Klivenyi, H.J. Freund, D. Scarano, A. Zecchina, IR investigations of CO2 adsorption on chromia surfaces: Cr2O3 (0001)/Cr(110) versus polycrystalline alpha-Cr2O3, Surface Science, 421 (1999) 176-190.
[14] R.L. Burwell, J.F. Read, K.C. Taylor, G.L. Haller, ADSORPTIVE AND CATALYTIC PROPERTIES OF CHROMIA, Zeitschrift Fur Physikalische Chemie-Frankfurt, 64 (1969) 18-&.
[15] D. Scarano, A. Zecchina, S. Bordiga, G. Ricchiardi, G. Spoto, INTERACTION OF CO WITH ALPHA-CR2O3 SURFACE - A FTIR AND HRTEM STUDY, Chem. Phys., 177 (1993) 547-560.
[16] D. Scarano, G. Spoto, S. Bordiga, G. Ricchiardi, A. Zecchina, REVISITING THE ALPHA-CR2O3/CO INTERACTION - AN FTIR AND HRTEM STUDY, Journal of Electron Spectroscopy and Related Phenomena, 64-5 (1993) 307-313.
[17] Estimated using the Redhead equation. The estimate assumes a non-activated adsorption process and a normal first-order pre-exponential for desoption of $10^{13}$ $sec^{-1}$.
[18] P.A. Redhead, Thermal desorption of gases, Vacuum, 12 (1962) 203-211.
[19] K. Tanabe, M. Misono, Y. Ono, H. Hattori, New solid acids and bases : their catalytic properties, Elsevier Science Pub. Co., New York, 1989.
[20] A. Auroux, A. Gervasini, MICROCALORIMETRIC STUDY OF THE ACIDITY AND BASICITY OF METAL-OXIDE SURFACES, Journal of Physical Chemistry, 94 (1990) 6371-6379.
[21] D.F. Cox, T.B. Fryberger, S. Semancik, Oxygen Vacancies and Defect Electronic States on the $SnO_2$(110)-1X1 Surface, Physical Review B, 38 (1988) 2072-2083.
[22] J.F. Moulder, W.F. Stickle, P.E. Sobol, K.D. Bomben, J. Chastain, Handbook of X-Ray Photoelectron Spectroscopy, Perkin-Elmer, Eden Prairie, MN, 1992.
[23] B.E. Bent, Mimicking aspects of heterogeneous catalysis: Generating, isolating, and reacting proposed surface intermediates on single crystals in vacuum, Chemical Reviews, 96 (1996) 1361-1390.
[24] L.E. Manzer, V.N.M. Rao, CATALYTIC SYNTHESIS OF CHLOROFLUOROCARBON ALTERNATIVES, Advances in Catalysis, 39 (1993) 329-350.
[25] M. Vecchio, G. Groppelli, J.C. Tatlow, STUDIES ON A VAPOR-PHASE PROCESS FOR MANUFACTURE OF CHLOROFLUOROETHANES, J. Fluor. Chem., 4 (1974) 117-139.
[26] J.D. Park, in: J.H. Simmons (Ed.) Fluorine Chemistry, Academic Press, New York, 1950, pp. 523.
[27] J.M. Hamilton, ADVANCES IN FLUORINE CHEMISTRY, in: N. Kharasch, W. Wolf (Eds.) Index to Reviews, Symposia Volumes and Monographs in Organic Chemistry, Pergamon, 1966, pp. 117.
[28] A.K. Barbour, M.W. Belf, M.W. Buxton, ADVANCES IN FLUORINE CHEMISTRY, in: N. Kharasch, W. Wolf (Eds.) Index to Reviews, Symposia Volumes and Monographs in Organic Chemistry, Pergamon, 1966, pp. 181.
[29] S.C. York, Halocarbon Reactions on the Chromium (III) Oxide (10-12) Surface, in: Chemical Engineering, Virginia Polytechnic Institute and State University, Blacksburg, VA, 1999, pp. 118.

[30] J.P. Collman, L.S. Hegedus, J.R. Norton, R.G. Finke, Principles and Applications of Organotransition Metal Chemistry, University Science Books, 1987.
[31] M.I. Bruce, A.G. Swincer, VINYLIDENE AND PROPADIENYLIDENE (ALLENYLIDENE) METAL-COMPLEXES, Advances in Organometallic Chemistry, 22 (1983) 59-128.
[32] P.J. Stang, Unsaturated carbenes, Chemical Reviews, 78 (1978) 383-405.
[33] R.M. Ormerod, R.M. Lambert, H. Hoffmann, F. Zaera, L.P. Wang, D.W. Bennett, W.T. Tysoe, Room-Temperature Chemistry of Acetylene on Pd(111) - Formation of Vinylidene, Journal of Physical Chemistry, 98 (1994) 2134-2138.
[34] L.L. Kesmodel, L.H. Dubois, G.A. Somorjai, LEED ANALYSIS OF ACETYLENE AND ETHYLENE CHEMISORPTION ON THE PT(111) SURFACE - EVIDENCE FOR ETHYLIDYNE FORMATION, Journal of Chemical Physics, 70 (1979) 2180-2188.
[35] G. Vacek, J.R. Thomas, B.J. Deleeuw, Y. Yamaguchi, H.F. Schaefer, ISOMERIZATION-REACTIONS ON THE LOWEST POTENTIAL-ENERGY HYPERSURFACE OF TRIPLET VINYLIDENE AND TRIPLET ACETYLENE, Journal of Chemical Physics, 98 (1993) 4766-4776.
[36] G.H. Hatzikos, R.I. Masel, Structure Sensitivity of Ethylene Adsorption on Pt(100) - Evidence for Vinylidene Formation on (1X1) Pt(100), Surface Science, 185 (1987) 479-494.
[37] J.A. Gates, L.L. Kesmodel, Thermal Evolution of Acetylene and Ethylene on Pd(111), Surface Science, 124 (1983) 68-86.
[38] M.M. Hills, J.E. Parmeter, W.H. Weinberg, Isolation and Characterization of Vinylidene from the Dehydrogenation of Ethylidyne on the Ru(001) P(2X2)O Surface, J Am Chem Soc, 109 (1987) 597-599.
[39] S.C. York, D.F. Cox,
[40] D. Bechadergue, M. Blanchard, P. Canesson, ISOMERIZATION AND DISMUTATION OF CHLOROFLUOROETHANES ON A CR2O3/C CATALYST, Applied Catalysis, 20 (1986) 179-187.
[41] B. D, B. M, C. P, Studies in Surface Science and Catalysis, Elsevier, New York, 1988.
[42] J. Barrault, S. Brunet, B. Requieme, M. Blanchard, PREPARATION OF SUBSTITUTES FOR CFCS - CATALYTIC PROPERTIES OF CHROMIA FOR HALOGEN EXCHANGE INVOLVING HYDROGEN-FLUORIDE AND TRIFLUOROCHLOROETHANE, J. Chem. Soc.-Chem. Commun., (1993) 374-375.
[43] M. Blanchard, L. Wendlinger, P. Canesson, HETEROGENEOUS CATALYTIC REACTIONS OF CHLOROFLUOROCARBONS, Applied Catalysis, 59 (1990) 123-128.
[44] L. Rowley, J. Thomson, G. Webb, J.M. Winfield, A. McCulloch, RADIOTRACERS IN FLUORINE CHEMISTRY .15. HALOGEN EXCHANGE AND ISOMERIZATION-REACTIONS INVOLVING CHLOROFLUOROETHANES ON FLUORINATED CHROMIA SURFACES LABELED WITH ANHYDROUS HYDROGEN F-18 FLUORIDE, HYDROGEN CL-36 CHLORIDE OR 1,1-DI CL-36 CHLOROTETRAFLUOROETHANE, Applied Catalysis, 79 (1991) 89-103.
[45] A. Kohne, E. Kemnitz, HETEROGENEOUS CATALYZED SYNTHESIS OF 1,1,1,2-TETRAFLUOROETHANE FROM 1,1,1,2-TETRACHLOROETHANE - THERMODYNAMICS AND REACTION PATHWAYS, J. Fluor. Chem., 75 (1995) 103-110.
[46] T.W.G. Solomons, Organic Chemistry, Wiley, New York, 1976.
[47] Adsorbed dimethyl ether (DME) desorption occurs at this same temperature.
[48] C.M. Byrd, D.F. Cox, unpublished results.
[49] K.S. Kim, M.A. Barteau, REACTIONS OF METHANOL ON TIO2(001) SINGLE-CRYSTAL SURFACES, Surface Science, 223 (1989) 13-32.
[50] V.A. Gercher, D.F. Cox, Formic-Acid Decomposition on $SnO_2$(110), Surface Science, 312 (1994) 106-114.
[51] T.J. Conway, Scanning Tunneling Microscopy and Adsorption Studies on Single Crystal Metal Oxide Surfaces, in: Chemical Engineering, Virginia Tech, 1998.
[52] F.H. Jones, R. Dixon, J.S. Foord, R.G. Egdell, J.B. Pethica, The surface structure of SnO2(110) (4x1) revealed by scanning tunneling microscopy, Surface Science, 376 (1997) 367-373.
[53] The natural cassiterite crystal from the Usigodino Mine in Spane was obtained from the Virginia Tech Geology Museum.
[54] G. Kresse, J. Furthmüller, Efficient iterative schemes for *ab initio* total-energy calculations using a plane-wave basis set, Physical Review B, 54 (1996) 11169-11186.
[55] G. Kresse, J. Furthmüller, Efficiency of ab-initio total energy calculations for metals and semiconductors using a plane-wave basis set, Computational Materials Science, 6 (1996) 15-50.
[56] G. Kresse, J. Hafner, *Ab initio* molecular dynamics for liquid metals, Physical Review B, 47 (1993) 558-561.
[57] D. Vanderbilt, Soft Self-Consistent Pseudopotentials in a Generalized Eigenvalue Formalism, Physical Review B, 41 (1990) 7892-7895.
[58] J.P. Perdew, J.A. Chevary, S.H. Vosko, K.A. Jackson, M.R. Pederson, D.J. Singh, C. Fiolhais, ATOMS, MOLECULES, SOLIDS, AND SURFACES - APPLICATIONS OF THE GENERALIZED GRADIENT APPROXIMATION FOR EXCHANGE AND CORRELATION, Physical Review B, 46 (1992) 6671-6687.
[59] J.P. Perdew, A. Zunger, SELF-INTERACTION CORRECTION TO DENSITY-FUNCTIONAL APPROXIMATIONS FOR MANY-ELECTRON SYSTEMS, Physical Review B, 23 (1981) 5048-5079.

[60] K.A. Johnson, N.W. Ashcroft, Corrections to density-functional theory band gaps, Physical Review B, 58 (1998) 15548-15556.
[61] I. Manassidis, J. Goniakowski, L.N. Kantorovich, M.J. Gillan, The structure of the stoichiometric and reduced SnO2(110) surface, Surface Science, 339 (1995) 258-271.
[62] T.T. Rantala, T.S. Rantala, V. Lantto, Surface relaxation of the (110) face of rutile SnO2, Surface Science, 420 (1999) 103-109.
[63] P.J.D. Lindan, N.M. Harrison, M.J. Gillan, Mixed dissociative and molecular adsorption of water on the rutile (110) surface, Phys. Rev. Lett., 80 (1998) 762-765.
[64] S. Tjandra, F. Zaera, Methyl-Iodide Thermal-Reactions When Chemisorbed on Ni(100) Surfaces, Langmuir, 8 (1992) 2090-2097.
[65] H.S. Guo, F. Zaera, Thermal chemistry of diiodomethane on Ni(110) surfaces I. Clean and hydrogen-covered, Surface Science, 547 (2003) 284-298.
[66] S.C. York, D.F. Cox, Dehalogenation of 1-chloro-1-fluoroethene to acetylene on $\alpha$-$Cr_2O_3$ (10(1)over-bar-2), Journal of Catalysis, 214 (2003) 273-283.
[67] S.C. York, D.F. Cox, Dehalogenation of 1-chloro-1-fluoroethene to acetylene on $\alpha$-$Cr_2O_3$ (10$\underline{1}$2), Journal of Catalysis, 214 (2003) 273-283.
[68] S.C. York, D.F. Cox, Dehalogenation of 1,1,2-trichloro-1-fluoroethane over $\alpha$-$Cr_2O_3$ (10$\underline{1}$2), Journal of Physical Chemistry B, 107 (2003) 5182-5189.
[69] J.L. Lin, C.M. Chiang, C.J. Jenks, M.X. Yang, T.H. Wentzlaff, B.E. Bent, Alkyl Chain Propagation by Methylene Insertion on Cu(100), Journal of Catalysis, 147 (1994) 250-263.
[70] M.X. Yang, P.W. Kash, D.H. Sun, G.W. Flynn, B.E. Bent, M.T. Holbrook, S.R. Bare, D.A. Fischer, J.L. Gland, Chemistry of chloroethylenes on Cu(100): Bonding and reactions, Surface Science, 380 (1997) 151-164.
[71] J. Stohr, NEXAFS Spectroscopy, Springer, New York, 1996.
[72] M.X. Yang, J. Eng, P.W. Kash, G.W. Flynn, B.E. Bent, M.T. Holbrook, S.R. Bare, J.L. Gland, D.A. Fischer, Generation and reaction of vinyl groups on a Cu(100) surface, Journal of Physical Chemistry, 100 (1996) 12431-12439.
[73] H. Rabus, D. Arvanitis, M. Domke, K. Baberschke, High-Resolution X-Ray Absorption-Spectroscopy of Linear Hydrocarbons Adsorbed on Noble-Metal Surfaces, Journal of Chemical Physics, 96 (1992) 1560-1573.
[74] A. Rohrbach, J. Hafner, G. Kresse, Ab initio study of the (0001) surfaces of hematite and chromia: Influence of strong electronic correlations, Physical Review B, 70 (2004) -.
[75] G. Kresse, J. Hafner, Ab initio molecular dynamics for liquid metals, Physical Review B (Condensed Matter), 47 (1993) 558-561.
[76] G. Kresse, J. Furthmüller, Efficient iterative schemes for ab initio total-energy calculations using a plane-wave basis set, Physical Review B - Condensed Matter and Materials Physics, 54 (1996) 11169-11186.
[77] P.E. Blochl, Projector Augmented-Wave Method, Physical Review B, 50 (1994) 17953-17979.
[78] J.P. Perdew, W. Yue, Accurate and simple analytic representation of the electron-gas correlation energy, Physical Review B (Condensed Matter), 45 (1992) 13244-13249.
[79] C.M. Byrd, Reaction chemistry of C1 hydrocarbon fragments and oxygenates on $Cr_2O_3$ (10$\underline{1}$2), in: Chemical Enginnering, Virginia Polytechnic Institute & State University, Blacksburg, Virginia, 2002.
[80] M.W. Abee, D.F. Cox, $BF_3$ adsorption on $\alpha$-$Cr_2O_3$ (10$\underline{1}$2): Probing the Lewis basicity of surface oxygen anions, Journal of Physical Chemistry B, 105 (2001) 8375-8380.
[81] T. Uozumi, K. Okada, A. Kotani, Theory of photoemission spectra for $M_2O_3$ (M=Ti, V, Cr, Mn, Fe) compounds, Journal of Electron Spectroscopy and Related Phenomena, 78 (1996) 103-106.
[82] A. Rohrbach, J. Hafner, G. Kresse, Electronic correlation effects in transition-metal sulfides, Journal of Physics-Condensed Matter, 15 (2003) 979-996.
[83] J.G. Forbes, A.J. Gellman, The Beta-Hydride Elimination Mechanism in Adsorbed Alkyl-Groups, J Am Chem Soc, 115 (1993) 6277-6283.
[84] M.T. Buelow, A.J. Gellman, Correlations between substituent effects for surface reactions and catalytic reactions, Journal of Molecular Catalysis a-Chemical, 131 (1998) 55-70.
[85] M.W. Abee, D.F. Cox, $BF_3$ adsorption on stoichiometric and oxygen-deficient $SnO_2$(110) surfaces, Journal of Physical Chemistry B, 107 (2003) 1814-1820.
[86] M.W. Abee, S.C. York, D.F. Cox, $CO_2$ adsorption on $\alpha$-$Cr_2O_3$ (10$\underline{1}$2) surfaces, Journal of Physical Chemistry B, 105 (2001) 7755-7761.
[87] D.F. Cox, T.B. Fryberger, S. Semancik, Surface Reconstructions of Oxygen Deficient $SnO_2$(110), Surface Science, 224 (1989) 121-142.

[88] V.A. Gercher, D.F. Cox, Water-Adsorption on Stoichiometric and Defective $SnO_2$(110) Surfaces, Surface Science, 322 (1995) 177-184.
[89] A.D. Becke, K.E. Edgecombe, A Simple Measure of Electron Localization in Atomic and Molecular-Systems, Journal of Chemical Physics, 92 (1990) 5397-5403.
[90] A. Savin, A.D. Becke, J. Flad, R. Nesper, H. Preuss, H.G. Vonschnering, A New Look at Electron Localization, Angewandte Chemie-International Edition in English, 30 (1991) 409-412.
[91] A. Savin, R. Nesper, S. Wengert, T.F. Fassler, ELF: The electron localization function, Angewandte Chemie-International Edition in English, 36 (1997) 1809-1832.
[92] B. Silvi, A. Savin, Classification of Chemical-Bonds Based on Topological Analysis of Electron Localization Functions, Nature, 371 (1994) 683-686.
[93] R.F.W. Bader, A bond path: A universal indicator of bonded interactions, Journal of Physical Chemistry A, 102 (1998) 7314-7323.
[94] R.F.W. Bader, Atoms in Molecules, Oxford Science Publications Oxford, 1990.
[95] R.F.W. Bader, H. Essen, The Characterization of Atomic Interactions, Journal of Chemical Physics, 80 (1984) 1943-1960.
[96] R.F.W. Bader, R.J. Gillespie, P.J. Macdougall, A Physical Basis for the Vsepr Model of Molecular-Geometry, J Am Chem Soc, 110 (1988) 7329-7336.
[97] R.F.W. Bader, S. Johnson, T.H. Tang, P.L.A. Popelier, The electron pair, Journal of Physical Chemistry, 100 (1996) 15398-15415.
[98] R.F.W. Bader, P.J. Macdougall, Toward a Theory of Chemical-Reactivity Based on the Charge-Density, J Am Chem Soc, 107 (1985) 6788-6795.
[99] R.F.W. Bader, P.J. Macdougall, C.D.H. Lau, Bonded and Nonbonded Charge Concentrations and Their Relation to Molecular-Geometry and Reactivity, J Am Chem Soc, 106 (1984) 1594-1605.
[100] G.V. Gibbs, D.F. Cox, M.B. Boisen, R.T. Downs, N.L. Ross, The electron localization function: a tool for locating favorable proton docking sites in the silica polymorphs, Physics and Chemistry of Minerals, 30 (2003) 305-316.
[101] G.V. Gibbs, D.F. Cox, T.D. Crawford, M.B. Boisen, M. Lim, A mapping of the electron localization function for the silica polymorphs: evidence for domains of electron pairs and sites of potential electrophilic attack, Physics and Chemistry of Minerals, 29 (2002) 307-318.
[102] G.V. Gibbs, D.F. Cox, N.L. Ross, A modeling of the structure and favorable H-docking sites and defects for the high-pressure silica polymorph stishovite, Physics and Chemistry of Minerals, 31 (2004) 232-239.
[103] G.V. Gibbs, D.F. Cox, N.L. Ross, T.D. Crawford, J.B. Burt, K.M. Rosso, A mapping of the electron localization function for earth materials, Physics and Chemistry of Minerals, 32 (2005) 208-221.
[104] G.V. Gibbs, D.F. Cox, K.M. Rosso, A. Kirfel, T. Lippmann, P. Blaha, K. Schwarz, Experimental and theoretical bond critical point properties for model electron density distributions for earth materials, Physics and Chemistry of Minerals, 32 (2005) 114-125.
[105] A. Kirfel, T. Lippmann, P. Blaha, K. Schwarz, D.F. Cox, K.M. Rosso, G.V. Gibbs, Electron density distribution and bond critical point properties for forsterite, $Mg_2SiO_4$, determined with synchrotron single crystal X-ray diffraction data, Physics and Chemistry of Minerals, 32 (2005) 301-313.
[106] G.V. Gibbs, D.F. Cox, N.L. Ross, T.D. Crawford, R.T. Downs, J.B. Burt, Comparison of the Electron Localization Function and Deformation Electron Density Maps for Selected Earth Materials, J. Phys. Chem. A, (2005).
[107] T.M. Muscenti, G.V. Gibbs, D.F. Cox, A simple chemical view of relaxations at stoichiometric (110) surfaces of rutile-structure type oxides: A first-principles study of stishovite, $SiO_2$, Surface Science, 594 (2005) 70-82.
[108] M. Ramamoorthy, D. Vanderbilt, R.D. King-Smith, First-principles calculations of the energetics of stoichiometric TiO2 surfaces, Physical Review B (Condensed Matter), 49 (1994) 16721-16727.
[109] S.P. Bates, G. Kresse, M.J. Gillan, A systematic study of the surface energetics and structure of $TiO_2$(110) by first-principles calculations, Surface Science, 385 (1997) 386-394.
[110] P.J.D. Lindan, J. Muscat, N.M. Harrison, S. Bates, M. Gillan, Ab initio simulation of molecular processes on oxide surfaces, Faraday Discuss, (1997) 135-154.
[111] P.J.D. Lindan, N.M. Harrison, M.J. Gillan, J.A. White, First-principles spin-polarized calculations on the reduced and reconstructed $TiO_2$ (110) surface, Physical Review B (Condensed Matter), 55 (1997) 15919-15927.
[112] U. Diebold, The surface science of titanium dioxide, Surface Science Reports, 48 (2003) 53-229.
[113] T.J. Godin, J.P. LaFemina, Atomic structure of the cassiterite $SnO_2$(111) surface, Surface Science, 301 (1994) 364-370.
[114] T.J. Godin, J.P. LaFemina, Surface atomic and electronic structure of cassiterite $SnO_2$(110), Physical Review B: Condensed Matter and Materials Physics, 47 (1993) 6518-6523.
[115] J. Oviedo, M.J. Gillan, Energetics and structure of stoichiometric $SnO_2$ surfaces studied by first-principles calculations, Surface Science, 463 (2000) 93-101.

[116] F.R. Sensato, R. Custodio, M. Calatayud, A. Beltran, J. Andres, J.R. Sambrano, E. Longo, Periodic study on the structural and electronic properties of bulk, oxidized and reduced $SnO_2$(1 1 0) surfaces and the interaction with $O_2$, Surface Science, 511 (2002) 408-420.
[117] Y.D. Kim, A.P. Seitsonen, H. Over, The atomic geometry of oxygen-rich Ru(0001) surfaces: coexistence of (1 x 1)O and $RuO_2$(110) domains, Surface Science, 465 (2000) 1-8.
[118] C.B. Duke, Semiconductor surface reconstruction: The structural chemistry of two-dimensional surface compounds, Chemical Reviews, 96 (1996) 1237-1259.
[119] A.S. Gibson, J.P. LaFemina, Structure of mineral surfaces, Physics and Chemistry of Mineral Surfaces, (1996) 1-62.
[120] J.P. Lafemina, Theory of insulator surface structures, Handbook of Surface Science, 1 (1996) 137-184.
[121] J.P. LaFemina, C.B. Duke, Dependence of oxide surface structure on surface topology and local chemical bonding, Journal of Vacuum Science & Technology, A: Vacuum, Surfaces, and Films, 9 (1991) 1847-1855.
[122] A.J. Skinner, J.P. LaFemina, Surface atomic and electronic structure of zinc oxide polymorphs, Physical Review B: Condensed Matter and Materials Physics, 45 (1992) 3557-3564.
[123] G.N. Lewis, Valence and the Structure of Atoms and Molecules, Dover Press, New York, 1966.
[124] R.J. Gillespie, Journal of Chemical Education, 47 (1970) 18.
[125] E.C.T. Chao, J.J. Fahey, J. Littler, Science, 133 (1961) 882.
[126] E.C.T. Chao, J.J. Fahey, J. Littler, D.J. Milton, Journal of Geophysical Research, 67 (1962) 419.
[127] J.D. Brooks, Q. Ma, D.F. Cox, Reactions of ethyl groups on a model chromia surface: Ethyl chloride on stoichiometric $\alpha$-$Cr_2O_3$ (10(1)over-bar2), Surface Science, 603 (2009) 523-528.
[128] M.A. McKee, Q. Ma, D.R. Mullins, M. Neurock, D.F. Cox, Reactions of vinyl groups on a model chromia surface: Vinyl chloride on stoichiometric $\alpha$-$Cr_2O_3$ (10(1)over-bar2), Surface Science, 603 (2009) 265-272.
[129] C.H. Hwang, C.W. Lee, H. Kang, C.M. Kim, Ethylene dehydrogenation to ethylidyne on Pt(111) studied by Cs+ reactive ion scattering. Evidence for an ethylidene intermediate, Surface Science, 490 (2001) 144-152.
[130] M.A. Henderson, S.A. Chambers, HREELS, TPD and XPS study of the interaction of water with the $\alpha$-$Cr_2O_3$(001) surface, Surface Science, 449 (2000) 135-150.
[131] F. Rohr, M. Baumer, H.J. Freund, J.A. Mejias, V. Staemmler, S. Muller, L. Hammer, K. Heinz, Strong relaxations at the $Cr_2O_3$(0001) surface as determined via low-energy electron diffraction and molecular dynamics simulations, Surface Science, 372 (1997) L291-L297.
[132] V. Maurice, S. Cadot, P. Marcus, XPS, LEED and STM study of thin oxide films formed on Cr(110), Surface Science, 458 (2000) 195-215.
[133] J.S. Foord, R.M. Lambert, Oxygen-Chemisorption and Corrosion on Cr(100) and Cr(110) Single-Crystal Surfaces, Surface Science, 161 (1985) 513-520.
[134] S.C. York, M.W. Abee, D.F. Cox, $\alpha$-$Cr_2O_3$ (10$\underline{1}$2): surface characterization and oxygen adsorption, Surface Science, 437 (1999) 386-396.
[135] N.S. McIntyre, D.G. Zetaruk, Quantitative-Analysis of Thin Oxide-Films Using X-Ray Photoelectron-Spectroscopy and Rastered Ion-Bombardment, Journal of Vacuum Science & Technology, 14 (1977) 181-185.
[136] J.F. Moulder, W.F. Stickle, P.E. Sobol, K.D. Bomben, Handbook of X-ray Photoelectron Spectroscopy, Perkin-Elmer Corporation, Physical Electronics Division, Eden Prairie, Minnesota, 1992.
[137] J.S. Foord, R.M. Lambert, Interaction of Oxygen with Chromium(Iii) Oxide - Chemisorption Studies and the Effects of Surface Additives, Surface Science, 169 (1986) 327-336.
[138] M.A. McKee, Q. Ma, D.F. Cox, Reactions of vinyl groups on a model chromia surface: vinyl chloride on stoichiometric $\alpha$-$Cr_2O_3$ (10$\underline{1}$2), Surface Science, (2008) **Accepted**.
[139] J.D. Brooks, Q. Ma, D.F. Cox, Reactions of ethyl groups on a model chromia surface: ethyl chloride on stoichiometric $\alpha$-$Cr_2O_3$ (10$\underline{1}$2), Surface Science, (2008) **Submitted**.
[140] M.A. Minton, Reaction of Halogenated Ethylenes on the $\alpha$-$Cr_2O_3$ (10$\underline{1}$2) Surface, in: Chemical Engineering, Virginia Polytechnic Institute & State University, Blacksburg, VA, 2006, pp. 113.
[141] M. Pykavy, V. Staemmler, O. Seiferth, H.J. Freund, Adsorption of CO on Cr2O3(0001), Surface Science, 479 (2001) 11-25.
[142] C. Xu, B. Dillmann, H. Kuhlenbeck, H.J. Freund, Unusual State of Adsorbed Co - Co(Square-Root-3xsquare-Root-3)R30-Degrees/Cr2o3(111), Phys. Rev. Lett., 67 (1991) 3551-3554.
[143] J. Dvorak, J. Hrbek, Adsorbate ordering effects in the trimerization reaction of acetylene on Cu(100), Journal of Physical Chemistry B, 102 (1998) 9443-9450.
[144] H. Hoffmann, F. Zaera, R.M. Ormerod, R.M. Lambert, J.M. Yao, D.K. Saldin, L.P. Wang, D.W. Bennett, W.T. Tysoe, A near-Edge X-Ray Absorption Fine-Structure and Photoelectron Spectroscopic Study of the Structure of Acetylene on Pd(111) at Low-Temperature, Surface Science, 268 (1992) 1-10.

[145] K. Judai, A.S. Worz, S. Abbet, J.M. Antonietti, U. Heiz, A. Del Vitto, L. Giordano, G. Pacchioni, Acetylene trimerization on Ag, Pd and Rh atoms deposited on MgO thin flms, Phys. Chem. Chem. Phys., 7 (2005) 955-962.
[146] A.F. Lee, K. Wilson, R.M. Lambert, A. Goldoni, A. Baraldi, G. Paolucci, On the coverage-dependent adsorption geometry of benzene adsorbed on Pd{111}: A study by fast XPS and NEXAFS, Journal of Physical Chemistry B, 104 (2000) 11729-11733.
[147] R.M. Ormerod, R.M. Lambert, H. Hoffmann, F. Zaera, J.M. Yao, D.K. Saldin, L.P. Wang, D.W. Bennett, W.T. Tysoe, NEXAFS Identification of a Catalytic Reaction Intermediate - $C_4H_4$ on Pd(111), Surface Science, 295 (1993) 277-286.
[148] K.G. Pierce, V.S. Lusvardi, M.A. Barteau, Catalytic formation of carbon-carbon bonds in ultrahigh vacuum: Cyclotrimerization of alkynes on reduced TiO2 surfaces, 11th International Congress on Catalysis - 40th Anniversary, Pts a and B, 101 (1996) 297-306.
[149] A. Ramirezcuesta, G. Zgrablich, W.T. Tysoe, Simulation of Benzene Formation from Acetylene on Palladium and Oxygen-Covered Palladium Surfaces, Surface Science, 340 (1995) 109-118.
[150] J. Szanyi, M.T. Paffett, Dimerization and Trimerization of Acetylene over a Model Sn/Pt Catalyst, J Am Chem Soc, 117 (1995) 1034-1042.
[151] J. Zhang, P. Braunstein, T.S.A. Hor, Highly selective chromium(III) ethylene trimerization catalysts with [NON] and [NSN] heteroscorpionate ligands, Organometallics, 27 (2008) 4277-4279.
[152] T. Agapie, J.A. Labinger, J.E. Bercaw, Mechanistic studies of olefin and alkyne trimerization with chromium catalysts: Deuterium labeling and studies of regiochemistry using a model chromacyclopentane complex, J Am Chem Soc, 129 (2007) 14281-14295.
[153] R.J. Lad, V.E. Henrich, Structure of $\alpha$-$Fe_2O_3$ Single-Crystal Surfaces Following Ar+ Ion-Bombardment and Annealing in $O_2$, Surface Science, 193 (1988) 81-93.
[154] R.J. Lad, V.E. Henrich, Structure of $\alpha$-$Fe_2O_3$ single crystal surfaces following Ar+ ion bombardment and annealing in $O_2$, Surface Science, 193 (1988) 81-93.
[155] C.R. Brundle, T.J. Chuang, K. Wandelt, Core and Valence Level Photoemission Studies of Iron-Oxide Surfaces and Oxidation of Iron, Surface Science, 68 (1977) 459-468.
[156] R.L. Kurtz, V.E. Henrich, Geometric Structure of the Alpha-Fe2o3(001) Surface - a Leed and Xps Study, Surface Science, 129 (1983) 345-354.
[157] R.L. Blake, Hessevic.Re, T. Zoltai, L.W. Finger, Refinement of Hematite Structure, Am. Miner., 51 (1966) 123-&.
[158] X.Y. Ma, L. Liu, J.J. Jin, P.C. Stair, D.E. Ellis, Experimental and theoretical studies of adsorption of CH3 center dot on alpha-Fe2O3(0001) surfaces, Surface Science, 600 (2006) 2874-2885.
[159] G. Henkelman, G. Johannesson, H. Jonsson, Methods for finding saddle points and minimum energy paths, Progress in Theoretical Chemistry and Physics, 5 (2000) 269-302.
[160] G. Henkelman, H. Jonsson, Improved tangent estimate in the nudged elastic band method for finding minimum energy paths and saddle points, Journal of Chemical Physics, 113 (2000) 9978-9985.
[161] G. Henkelman, B.P. Uberuaga, H. Jonsson, A climbing image nudged elastic band method for finding saddle points and minimum energy paths, Journal of Chemical Physics, 113 (2000) 9901-9904.
[162] E.A. Jarvis, A.M. Chaka, Oxidation mechanism and ferryl domain formation on the alpha-Fe2O3 (0001) surface, Surface Science, 601 (2007) 1909-1914.
[163] T.P. Trainor, A.M. Chaka, P.J. Eng, M. Newville, G.A. Waychunas, J.G. Catalano, G.E. Brown, Structure and reactivity of the hydrated hematite (0001) surface, Surface Science, 573 (2004) 204-224.
[164] B. Halevi, J.M. Vohs, Reactions of CH3SH and (CH3)(2)S-2 on the (0001) and (0001) surfaces of ZnO, Journal of Physical Chemistry B, 109 (2005) 23976-23982.
[165] J.D. Brooks, Q. Ma, D.F. Cox, Reactions of ethyl groups on a model chromia surface: Ethyl chloride on stoichiometric alpha-Cr(2)O(3) (10(1)over-bar2), Surface Science, 603 (2009) 523-528.
[166] J.D. Brooks, T.L. Chen, D.R. Mullins, D.F. Cox, Reactions of ethylidene on a model chromia surface: 1,1-dichloroethane on stoichiometric alpha-Cr(2)O(3) (10(1)over-bar2), Surface Science, 605 (2011) 1170-1176.
[167] F.A. Cotton, G. Wilkinson, M. Bochmann, C.A. Murillo, Advanced Inorganic Chemistry: A Comprehensive Text, 6 ed., Wiley, New York, 1999.
[168] M.A. Henderson, Low temperature oxidation of Fe(2+) surface sites on the (2 x 1) reconstructed surface of alpha-Fe(2)O(3)(01(1)over-bar2), Surface Science, 604 (2010) 1197-1201.
[169] M.A. Henderson, Photochemistry of methyl bromide on the alpha-Cr(2)O(3)(0001) surface, Surface Science, 604 (2010) 1800-1807.
[170] M.A. Henderson, Insights into the (1 x 1)-to-(2 x 1) phase transition of the $\alpha$-$Fe_2O_3$(0 1 2) surface using EELS, LEED and water TPD, Surface Science, 515 (2002) 253-262.
[171] M.A. Henderson, S.A. Joyce, J.R. Rustad, Interaction of water with the (1x1) and (2x1) surfaces of alpha-Fe2O3(012), Surface Science, 417 (1998) 66-81.

[172] R.J. Lad, V.E. Henrich, STRUCTURE OF ALPHA-FE2O3 SINGLE-CRYSTAL SURFACES FOLLOWING AR+ ION-BOMBARDMENT AND ANNEALING IN O-2 - REPLY, Surface Science, 200 (1988) L473-L474.
[173] U. Becker, M.F. Hochella, E. Apra, The electronic structure of hematite{001} surfaces: Applications to the interpretation of STM images and heterogeneous surface reactions, Am. Miner., 81 (1996) 1301-1314.
[174] N.G. Condon, F.M. Leibsle, A.R. Lennie, P.W. Murray, T.M. Parker, D.J. Vaughan, G. Thornton, Scanning tunnelling microscopy studies of alpha-Fe2O3(0001), Surface Science, 397 (1998) 278-287.
[175] N.G. Condon, P.W. Murray, F.M. Leibsle, G. Thornton, A.R. Lennie, D.J. Vaughan, FE3O4(111) TERMINATION OF ALPHA-FE2O3(0001), Surface Science, 310 (1994) L609-L613.
[176] C.M. Eggleston, The surface structure of alpha-Fe2O3 (001) by scanning tunneling microscopy: Implications for interfacial electron transfer reactions, Am. Miner., 84 (1999) 1061-1070.
[177] C.M. Eggleston, A.G. Stack, K.M. Rosso, A.M. Bice, Adatom Fe(III) on the hematite surface: Observation of a key reactive surface species, Geochemical Transactions, 5 (2004) 33-40.
[178] R.A. Fellows, A.R. Lennie, H. Raza, C.L. Pang, G. Thornton, D.J. Vaughan, Fe3O4 (111) formation on a reduced alpha-Fe2O3 (11(2)over-bar3) substrate: a low-energy electron diffraction and scanning tunnelling microscopy study, Surface Science, 445 (2000) 11-17.
[179] K.T. Rim, J.P. Fitts, T. Muller, K. Adib, N. Camillone, R.M. Osgood, S.A. Joyce, G.W. Flynn, CCl4 chemistry on the reduced selvedge of a alpha-Fe2O3(0001) surface: a scanning tunneling microscopy study, Surface Science, 541 (2003) 59-75.
[180] K.T. Rim, T. Muller, J.P. Fitts, K. Adib, N. Camillone, R.M. Osgood, E.R. Batista, R.A. Friesner, S.A. Joyce, G.W. Flynn, Scanning tunneling microscopy and theoretical study of competitive reactions in the dissociative chemisorption of CCl4 on iron oxide surfaces, Journal of Physical Chemistry B, 108 (2004) 16753-16760.
[181] W. Weiss, W. Ranke, Surface chemistry and catalysis on well-defined epitaxial iron-oxide layers, Progress in Surface Science, 70 (2002) 1-151.
[182] M.A. Henderson, Surface stabilization of organics on hematite by conversion from terminal to bridging adsorption structures, Geochimica Et Cosmochimica Acta, 67 (2003) 1055-1063.
[183] Z.M. Liu, X.L. Zhou, J.M. White, Electron-Induced Dissociation of Monolayer C2h5cl on Ag(111) - Electron-Energy Dependence, Chem Phys Lett, 198 (1992) 615-620.
[184] L. Lin, B.R. Quezada, P.C. Stair, Adsorption, Desorption, and Reaction of Methyl Radicals on Surface Terminations of alpha-Fe(2)O(3), J. Phys. Chem. C, 114 (2010) 17105-17111.
[185] G. Rollmann, A. Rohrbach, P. Entel, J. Hafner, First-principles calculation of the structure and magnetic phases of hematite, Physical Review B, 69 (2004).
[186] D. Hucknall, Selective Oxidation of Hydrocarbons, Academic Press, New York, 1974.
[187] D.A. Dowden, D. Wells, Actes du 2e Congres International de Catalyse, in, 1961, pp. 1489.
[188] M. Loukah, G. Coudurier, J.C. Vedrine, Studies in Surface Science and Catalysis, 72 (1992) 191.
[189] P. Oliver-Pastor, e. al., Studies in Surface Science and Catalysis, 82 (1994) 103.
[190] A.P.E. York, J.B. Claridge, M.L.H. Green, S.C. Tsang, Studies in Surface Science and Catalysis, (1994) 315.
[191] F. Cavani, M. Koutyrev, F. Trifiro, A. Bartolini, D. Ghisletti, R. Iezzi, A. Santucci, G. DelPiero, Chemical and physical characterization of alumina-supported chromia-based catalysts and their activity in dehydrogenation of isobutane, Journal of Catalysis, 158 (1996) 236-250.
[192] M. Hoang, J.F. Mathews, K.C. Pratt, Oxidative dehydrogenation of isobutane to isobutylene over supported transition metal oxide catalysts, Reaction Kinetics and Catalysis Letters, 61 (1997) 21-26.
[193] L.Y. Xu, e. al., Natural Gas Conversion, 119 (1998) 605.
[194] O.F. Gorriz, L.E. Cadus, Supported chromium oxide catalysts using metal carboxylate complexes: dehydrogenation of propane, Applied Catalysis a-General, 180 (1999) 247-260.
[195] L.R. Mentasty, O.F. Gorriz, L.E. Cadus, Chromium oxide supported on different $Al_2O_3$ supports: Catalytic propane dehydrogenation, Industrial & Engineering Chemistry Research, 38 (1999) 396-404.
[196] B.M. Weckhuysen, R.A. Schoonheydt, Alkane dehydrogenation over supported chromium oxide catalysts, Catalysis Today, 51 (1999) 223-232.
[197] O.F. Gorriz, V.C. Corberan, J.L.G. Fierro, Propane Dehydrogenation and Coke Formation on Chromia-Alumina Catalysts - Effect of Reductive Pretreatments, Industrial & Engineering Chemistry Research, 31 (1992) 2670-2674.
[198] M. Cherian, M.S. Rao, W.T. Yang, H.M. Jehng, A.M. Hirt, G. Deo, Oxidative dehydrogenation of propane over $Cr_2O_3/Al_2O_3$ and $Cr_2O_3$ catalysts: effects of loading, precursor and surface area, Applied Catalysis a-General, 233 (2002) 21-33.
[199] S.B. Wang, K. Murata, T. Hayakawa, S. Hamakawa, K. Suzuki, Oxidative dehydroisomerization of n-butane over anion-promoted $Cr_2O_3/ZrO_2$ catalysts, Energy & Fuels, 15 (2001) 384-388.

[200] B. Grzybowska, J. Sloczynski, R. Grabowski, L. Keromnes, K. Wcislo, T. Bobinska, Oxidation of C2-C4 alkanes on chromium oxide/alumina and on $Cr_2O_3$: catalytic and TPD studies, Applied Catalysis a-General, 209 (2001) 279-289.
[201] Y. Ohtsuka, K. Asamil, Y. Wang, Novel utilization of carbon dioxide for direct conversion of methane to ethane and ethylene, Journal of the Chinese Institute of Chemical Engineers, 30 (1999) 439-447.
[202] A. Hakuli, M.E. Harlin, L.B. Backman, A.O.I. Krause, Dehydrogenation of i-butane on $CrO_x/SiO_2$ catalysts, Journal of Catalysis, 184 (1999) 349-356.
[203] I. Takahara, W.C. Chang, N. Mimura, M. Saito, Promoting effects of $CO_2$ on dehydrogenation of propane over a $SiO_2$-supported $Cr_2O_3$ catalyst, Catalysis Today, 45 (1998) 55-59.
[204] X. Wang, Y.C. Xie, Total oxidation of $CH_4$ on Sn-Cr composite oxide catalysts, Applied Catalysis B-Environmental, 35 (2001) 85-94.
[205] H. Zou, X. Ge, M.S. Li, R.C. Shangguan, J.Y. Shen, Dehydrogenation of propane over $CrO_x/SiO_2$ catalysts under $CO_2$ atmosphere, Chinese Journal of Inorganic Chemistry, 16 (2000) 775-782.
[206] C.M. Pradier, F. Rodrigues, P. Marcus, M.V. Landau, M.L. Kaliya, A. Gutman, M. Herskowitz, Supported chromia catalysts for oxidation of organic compounds - The state of chromia phase and catalytic performance, Applied Catalysis B-Environmental, 27 (2000) 73-85.
[207] S. Wang, K. Murata, T. Hayakawa, S. Hamakawa, K. Suzuki, Effect of promoters on catalytic performance of $Cr/SiO_2$ catalysts in oxidative dehydrogenation of ethane with carbon dioxide, Catalysis Letters, 73 (2001) 107-111.
[208] S.B. Wang, K. Murata, T. Hayakawa, S. Hamakawa, K. Suzuki, Effect of promoters on catalytic performance of $Cr/SiO_2$ catalysts in oxidative dehydrogenation of ethane with carbon dioxide, Catalysis Letters, 73 (2001) 107-111.
[209] S.B. Wang, K. Murata, T. Hayakawa, S. Hamakawa, K. Suzuki, Oxidative dehydrogenation of ethane by carbon dioxide over sulfate-modified $Cr_2O_3/SiO_2$ catalysts, Catalysis Letters, 63 (1999) 59-64.
[210] S.B. Wang, K. Murata, T. Hayakawa, S. Hamakawa, K. Suzuki, Dehydrogenation of ethane with carbon dioxide over supported chromium oxide catalysts, Applied Catalysis a-General, 196 (2000) 1-8.
[211] S.B. Wang, K. Murata, T. Hayakawa, S. Hamakawa, K. Suzuki, Dehydrogenation of ethane into ethylene by carbon dioxide over chromium supported on sulfated silica, Chemistry Letters, (1999) 569-570.
[212] B. Grzybowska, J. Sloczynski, R. Grabowski, K. Wcislo, A. Kozlowska, J. Stoch, J. Zielinski, Chromium oxide alumina catalysts in oxidative dehydrogenation of isobutane, Journal of Catalysis, 178 (1998) 687-700.
[213] I. Takahara, M. Saito, Promoting effects of carbon dioxide on dehydrogenation of propane over a $SiO_2$-supported $Cr_2O_3$ catalyst, Chemistry Letters, (1996) 973-974.
[214] S. Derossi, G. Ferraris, S. Fremiotti, E. Garrone, G. Ghiotti, M.C. Campa, V. Indovina, Propane Dehydrogenation on Chromia Silica and Chromia Alumina Catalysts, Journal of Catalysis, 148 (1994) 36-46.
[215] D.W. Flick, M.C. Huff, Oxidative dehydrogenation of ethane over supported chromium oxide and Pt modified chromium oxide, Applied Catalysis a-General, 187 (1999) 13-24.
[216] V.E. Henrich, P.A. Cox, The Surface Science of Metal Oxides, 1994.
[217] Y. Dong, J.D. Brooks, T.-L. Chen, D.R. Mullins, D.F. Cox, Methylene migration and coupling on a non-reducible metal oxide: The reaction of dichloromethane on stoichiometric $\alpha$-$Cr_2O_3$(0001), Surface Science, 632 (2015) 28-38.
[218] Y. Dong, Geometric and Electronic Structure Sensitivity of Methyl and Methylene Reactions on $\alpha$-$Cr_2O_3$ and $\alpha$-$Fe_2O_3$ surfaces, in: Chemical Engineering, Virginia Polytechnic Institute and State University, Blacksburg, VA, 2012, pp. 138.
[219] Y. Dong, J.D. Brooks, T.-L. Chen, D.R. Mullins, D.F. Cox, Reactions of methyl groups on a non-reducible metal oxide: The reaction of iodomethane on stoichiometric $\alpha$-$Cr_2O_3$(0001), Surface Science, 641 (2015) 148-153.
[220] J.D. Brooks, Model Chromia Surface Chemistry: $C_2$ Alkyl Fragment Reactions and Probe Molecule Interactions, in: Chemical Engineering, Virginia Polytechnic Institute and State University, Blacksburg, VA, 2010, pp. 91.
[221] J.D. Brooks, T.-L. Chen, D.R. Mullins, D.F. Cox, Reactions of ethylidene on a model chromia surface: 1,1-dichloroethane on stoichiometric $\alpha$-Cr2O3 (10(1)over-bar2), Surface Science, 605 (2011) 1170-1176.
[222] C.M. Byrd, Reaction chemistry of $C_1$ hydrocarbon fragments and oxygenates on $\alpha$-$Cr_2O_3$ (10-12), in: Chemical Engineering, Virginia Polytechnic Institute and State University, Blacksburg, VA, 2003, pp. 104.
[223] B. Halevi, J.M. Vohs, Site requirements for the reactions of CH3SH and (CH3)(2)S-2 on ZnO(10(1)over-bar0), Surface Science, 602 (2008) 198-204.
[224] P. Berlowitz, B.L. Yang, J.B. Butt, H.H. Kung, Reactions of diazomethane on a clean, H-covered and O-covered Pt(111) surface, Surface Science, 159 (1985) 540-554.
[225] C.M. Chiang, T.H. Wentzlaff, B.E. Bent, Iodomethane decomposition on copper(110): surface reactions of $C_1$ fragments, The Journal of Physical Chemistry, 96 (1992) 1836-1848.
[226] F. Solymosi, I. Kovács, Carbon-carbon coupling of methylene groups: thermal and photo-induced dissociation of $CH_2I_2$ on Pd(100) surface, Surface Science, 296 (1993) 171-185.

[227] B. Xu, Y. Bhawe, M.E. Davis, Low-temperature, manganese oxide-based, thermochemical water splitting cycle, Proceedings of the National Academy of Sciences of the United States of America, 109 (2012) 9260-9264.
[228] B. Xu, Y. Bhawe, M.E. Davis, Spinel Metal Oxide-Alkali Carbonate-Based, Low-Temperature Thermochemical Cycles for Water Splitting and CO2 Reduction, Chemistry of Materials, 25 (2013) 1564-1571.
[229] X. Feng, D.F. Cox, Na Deposition on MnO(100), Surface Science, 645 (2016) 23-29.
[230] V. Bayer, R. Podloucky, C. Franchini, F. Allegretti, B. Xu, G. Parteder, M.G. Ramsey, S. Surnev, F.P. Netzer, Formation of $Mn_3O_4$(001) on MnO(001): Surface and interface structural stability, Physical Review B, 76 (2007) 165428.
[231] M.A. Langell, C.W. Hutchings, G.A. Carson, M.H. Nassir, High resolution electron energy loss spectroscopy of MnO(100) and oxidized MnO(100), J Vac Sci Technol A, 14 (1996) 1656-1661.
[232] X. Feng, Interactions of Na, O2, CO2 and water with MnO(100): Modeling a complex mixed oxide system for thermochemical water splitting, in: Chemical Engineering, Virginia Polytechnic Institute and State University, Blacksburg, VA, 2015, pp. 118.
[233] G. Kresse, D. Joubert, From ultrasoft pseudopotentials to the projector augmented-wave method, Physical Review B, 59 (1999) 1758-1775.
[234] S.L. Dudarev, G.A. Botton, S.Y. Savrasov, C.J. Humphreys, A.P. Sutton, Electron-energy-loss spectra and the structural stability of nickel oxide: An LSDA+U study, Physical Review B, 57 (1998) 1505-1509.
[235] J.P. Perdew, K. Burke, M. Ernzerhof, Generalized Gradient Approximation Made Simple, Phys. Rev. Lett., 77 (1996) 3865-3868.
[236] S. Grimme, J. Antony, S. Ehrlich, H. Krieg, A consistent and accurate ab initio parametrization of density functional dispersion correction (DFT-D) for the 94 elements H-Pu, Journal of Chemical Physics, 132 (2010).
[237] T. Shishido, H. Tsuji, Y. Gao, H. Hattori, H. Kita, Extensive oxygen exchange between carbon dioxide and magnesium oxide surface, Reaction Kinetics and Catalysis Letters, 51 (1993) 75-79.
[238] H. Tsuji, T. Shishido, A. Okamura, Y. Gao, H. Hattori, H. Kita, Oxygen exchange between magnesium oxide surface and carbon dioxide, Journal of the Chemical Society, Faraday Transactions, 90 (1994) 803-807.
[239] H. Tsuji, A. Okamura-Yoshida, T. Shishido, H. Hattori, Dynamic Behavior of Carbonate Species on Metal Oxide Surface: Oxygen Scrambling between Adsorbed Carbon Dioxide and Oxide Surface, Langmuir, 19 (2003) 8793-8800.
[240] Y. Yanagisawa, K. Takaoka, S. Yamabe, Exchange of strong carbon dioxide O=C bonds on an MgO surface, Journal of the Chemical Society, Faraday Transactions, 90 (1994) 2561-2566.